



UNIVERSIDAD TECNOLÓGICA NACIONAL
Facultad Regional Concepción del Uruguay
INGENIERIA ELECTROMECHANICA

PROYECTO FINAL DE CARRERA
(P F C)

**Evaluación de la nucleación y precipitación de
carburos secundarios en hierros fundidos con alto
contenido de cromo al 16%**

Proyecto N°: PFC-2207A

Autor: Vergniaud, Pablo Martín

Tutores: Dra. Guitar, María Agustina – Universidad del Saarland. Alemania

Dra. Dalibon, Eugenia – Universidad Tecnológica Nacional. Facul-
tad Regional Concepción del Uruguay

Dirección de Proyectos: Ing. Puente, Gustavo

AÑO 2022

Ing. Pereira 676 –C. del Uruguay (3260) – Entre Ríos – Argentina

Tel. / Fax: 03442 – 425541 / 423803 - Correo Electrónico: frcu@frcu.utn.edu.ar



NATIONAL TECHNOLOGICAL UNIVERSITY
Regional Faculty Concepción del Uruguay

Electromechanical Engineering

Final Degree Project

Evaluation of the nucleation and precipitation of secondary
carbides in 16% high chromium cast irons

Final Project submitted in compliance with the requirements of the Electromechanical Engineering degree course of the Regional Faculty Concepción del Uruguay, carried out by the student:

Vergniaud, Pablo Martín

Tutor:

Dra. María Agustina Guitar

Dra. Eugenia Dalibon

Concepción del Uruguay, Entre Ríos
Argentina

Year 2022

Content

ACKNOWLEDGMENTS.....	I
ABSTRACT	II
RESUMEN	IV
CHAP. 1: INTRODUCTION	1
1.1. INSTITUTIONAL FRAMEWORK	1
1.2. OBJECTIVES.....	1
1.3. SCOPE	2
CHAP. 2: THEORETICAL FRAMEWORK.....	3
2.1. CRYSTALLOGRAPHIC STRUCTURE	3
2.2. HYPOEUTECTIC WHITE CAST IRONS.....	7
2.3. HIGH CHROMIUM CAST IRONS (HCCI)	10
2.4. MICOESTRUCTURAL CONSTTUENTS.....	12
2.4.1. MATRIX.....	12
2.4.1.1. MARTENSITIC TRANSFORMATION.....	14
2.5. HEAT TREATMENTS (SOLID TRANSFORMATIONS).....	17
2.6. DESTABILIZATION HEAT TREATMENT	17
CHAP.3: STATE OF THE ART	20
3.1. DESTABILIZATION HEAT TREATMENT OF HCCI	20
3.2. WEAR AND TRIBOLOGY	23
CHAP. 4: CHARACTERIZATION METHODS	29
4.1. SCANNING ELECTRON MICROSCOPE (SEM).....	29
4.2. CONFOCAL LASER SCANNING MICROSCOPE (CLSM).....	33
CHAP. 5: EXPERIMENTAL PROCEDURE	36
5.1. SAMPLES.....	36

5.2.	HEAT TREATMENT	37
5.3.	METALLOGRAPHIC PREPARATION	38
5.4.	ETCHING.....	40
5.5.	IMAGE ANALYSIS (I-A)	41
5.6.	HARDNESS MEASUREMENT	43
5.7.	TRIBOLOGICAL TESTS.....	43
CHAP. 6: RESULTS AND DISCUSSIONS.....		46
6.1.	PHASE AND MICROSTRUCTURAL EVOLUTION.....	46
6.2.	SECONDARY CARBIDES CHARACTERIZATION.....	51
6.3.	MICROHARDNESS.....	58
6.4.	WEAR	61
6.4.1.	Microstructural analysis of the 800 °C heat treated sample after wear test	67
6.4.2.	Microstructural analysis of the 900°C heat treated sample after wear test	71
6.4.3.	Microstructural analysis of the 980°C heat treated sample after wear test	74
CHAP. 7: SUMMARY AND CONCLUSIONS.....		78
7.1.	SYNTHESIS OF RESULTS	78
7.2.	DEGREE OF ACHIEVEMENT OF OBJECTIVES	81
7.3.	EVALUATION OF RESULTS.....	82
CHAP. 8: REFERENCES.....		83
APPENDIX.....		91
LIST OF FIGURES.....		91
LIST OF TABLES		96

ACKNOWLEDGMENTS

With the following words, I aspire to acknowledge all those that were somehow involved in the making of this thesis.

For starters, I would like to thank Dr Sonia Brühl. None of this would have been possible without her trust and support throughout this whole experience. Additionally, I would like to thank Prof. Frank Mücklich for giving me the opportunity to carry out my experimental work at his institute, and Dr.-Ing. Flavio Soldera for his help throughout the previous stages of my stay in Saarbrücken.

Many thanks go to the European School of Materials at the University of Saarland for financially supporting my trip and stay in Saarbrücken, giving me the possibility to carry out my research.

I would also like to thank all the wonderful people that I met at Saarland University, in specific my tutor Dr. M. Agustina Guitar, and Ph.D. U. Pranav Nayak. I am extremely thankful for all their time, dedication, and effort. They have taught me so much and have played a key role in this thesis. In addition, I would like to thank Sebastian Suarez, U. Pranav Nayak, Timothy MacLucas, Christian Schäfer, Michael Kasper, Silas Schütz, Tobias Fox, and Rouven Zimmer for their friendship and for helping me to make my stay in Germany easier.

Many thanks to all members of the Surface Engineering Group (GIS), especially my co-tutor Dr. Dalibon, Eugenia, and all other people that have influenced me throughout the last six years.

Last but not least, I would like to thank my parents for the effort they made so that I could study, to my brothers, my girlfriend, and my daughter. Their love and support have been vital every step of the way, and for that, I am truly thankful. I would not be the person that I am today without all of them in my life. This achievement is as much theirs, as it is mine.

ABSTRACT

Microstructures with different fractions of carbides, austenite, ferrite, pearlite, and other phases can be obtained by applying different destabilization heat treatments (HT), which modify the tribological response in abrasion-resistant high-chromium cast irons. In the present work, three destabilization heat treatments were carried out at temperatures of 800, 900 and 980°C, with a dwell time of 0 minutes and a subsequent quenching in water in all three cases. The microstructure was characterized by confocal optical microscopy (CLSM) and scanning electron microscopy (SEM), before and after etching with Vilella's reagent. The quantification and characterization of the secondary carbides was carried out by SEM image analysis after etching with modified Murakami reagent. This process was carried out by image segmentation using FIJI software. Sliding wear response and tribological characteristics were evaluated by CLSM, SEM and EDS, together with dry reciprocating sliding wear tests. The latter were carried out using a 3mm Al₂O₃ ball, a constant load of 20N and 2000 cycles, in an atmosphere of 22-26°C and 40-50% relative humidity.

As a result, the microstructure of the 16 wt.% Cr white cast iron, with increasing destabilization temperature, had an increase in the number and size of secondary carbide particles of the M₇C₃ type, accompanied by an increase in the martensitic phase and a decrease in the austenitic phase in the matrix. As for the matrix hardness, it remained constant except for the 980°C condition, which increased its value by ~30%. The results show that the average particle size as well as the volume fraction of secondary carbides particles increased with increasing temperature. This had direct implications on the wear properties, where a decrease of up to 50, 71 and 77% in the wear rate of the destabilized samples was observed at 800, 900 and 980°C, respectively compared to the untreated material. The coefficient of friction also decreased significantly for the 900 and 980°C samples with respect to the untreated one (25 and 30% respectively), while for the 800°C sample it barely decreased by 6%. This can be explained by the increase in the martensite fraction in the matrix, together with an increase in number and average size of the SCs. Finally, the results obtained in this study shed light on the ability to alter the HT parameters to adjust the microstructure according to the prerequisites of the application.

Keywords: High chromium cast iron · Destabilization heat treatment · Austenite transformation · Secondary carbides · Wear rate · Microstructural tailoring.

RESUMEN

Es posible obtener microestructuras con diferentes fracciones de carburos, austenita, ferrita, perlita y otras fases mediante la aplicación de distintos tratamientos térmicos de destabilización, los cuales modifican la respuesta tribológica en las fundiciones de hierro con alto contenido de cromo resistentes a la abrasión. En el presente trabajo se realizaron tres tratamientos térmicos de destabilización a temperaturas de 800, 900 y 980°C, con un tiempo de permanencia de 0 minutos y un posterior temple en agua, en los tres casos. La microestructura fue caracterizada mediante microscopía óptica confocal (CLSM) y electrónica de barrido (SEM), previo y posterior a un ataque con el reactivo de Vilella. La cuantificación y caracterización de los carburos secundarios se llevó a cabo mediante el análisis de imágenes SEM luego del ataque con reactivo de Murakami modificado. Este proceso se realizó por medio de la segmentación de las imágenes utilizando el software FIJI. La respuesta al desgaste por deslizamiento y las características tribológicas fueron evaluadas combinando CLSM, SEM y EDS, junto con ensayos de desgaste de deslizamiento recíproco en seco. Estos últimos se realizaron utilizando como contraparte una bolilla de Al₂O₃ de 3mm, una carga constante de 20N y 2000 ciclos, en una atmósfera de 22-26°C y 40-50% de humedad relativa.

Como resultado, la microestructura de la fundición blanca de 16% Cr, con el aumento de la temperatura de destabilización tuvo un crecimiento en el número y tamaño de las partículas de carburos secundarios del tipo M₇C₃, acompañado de un incremento de la fase martensítica y una disminución de la austenítica en la matriz. En cuanto a la dureza de la matriz, ésta se mantuvo constante a excepción de la condición 980°C, la cual aumentó su valor en ~30%. Los resultados muestran que el tamaño promedio de partículas, así como la fracción de volumen de SC fue creciendo a medida que lo hacía la temperatura. Esto tuvo implicaciones directas en las propiedades de desgaste, donde se observó una disminución de hasta el 50, 71 y 77% en la tasa de desgaste de las muestras desestabilizadas a 800, 900 y 980°C, respectivamente en comparación con el material no tratado. El coeficiente de fricción también disminuyó significativamente para las muestras de 900 y 980°C con respecto a la sin tratar (25 y 30% respectivamente), mientras que para la muestra de 800°C apenas disminuyó en un 6%. Esto puede explicarse por el incremento en la fracción de martensita en la matriz, junto con un aumento en número y tamaño promedio

de los SC. Por último, los resultados obtenidos en este estudio arrojan luz sobre la capacidad de alterar los parámetros de HT para ajustar la microestructura en función de los requisitos previos de la aplicación.

Palabras claves: Fundición con alto contenido en cromo - Tratamiento térmico de desestabilización - Transformación austenítica - Carburos secundarios - Índice de desgaste - Adaptación microestructural.

CHAP. 1: INTRODUCTION

1.1. INSTITUTIONAL FRAMEWORK

The present work was developed in two parts, the first was the experimental work carried out in Germany, at the Chair of Functional Materials Research Group at the University of Saarland, Saarbrücken, Germany. All the equipment used in the research work is located in this institute. The participation in the research group was part of a three-month fellowship funded by the European School of Materials at the University of Saarland (EUSMAT). It was an incredible opportunity to gain knowledge and experience in the area of scientific research. In addition, it gave me the possibility to develop another research in parallel and to manipulate the equipment to characterize the samples of this work. The second part consisted of the analysis of the results and the writing of this final project, carried out in Argentina at the Surface Engineering Group (GIS) of the Technological National University, Regional Faculty of Concepción.

1.2. OBJECTIVES

The main objective of this thesis is to understand the kinetics and nature of the secondary carbide precipitation occurring in an HCCI_16%Cr during the heating up to the destabilization temperature. Besides the variation in size and fraction of the secondary carbides, other microstructural modifications are expected to occur as a function of the reached temperature such as austenite to martensite transformation during cooling. All these factors will affect the mechanical and tribological response of the material. Therefore, this work has also the objective of addressing the tribological response of an HCCI_16%Cr to the different microstructures modified during the heating.

For reaching these objectives the following steps will be followed:

- Perform heat treatments varying the temperature reached during heating to obtain microstructures with a diverse combination of microstructural features. The heat treatment parameters are selected from kinetic simulations.
- Identification of the secondary carbides precipitated during heat treatments.
- Quantification of secondary carbides in terms of size, volume fraction, and distance between particles.
- Evaluation of the wear resistance by performing ball-on-plate tribological tests.
- Correlation of the microstructure to the wear response.
- Comparison of results from 16% Cr HCCI to 26% Cr HCCI.

1.3. SCOPE

- 16% HCCI samples will be characterized before and after the different destabilization heat treatments.
- The relation between temperature and morphology of the secondary carbides' precipitation will be established.
- The influence of the different heat treatments on the wear resistance will be determined.
- The knowledge will be transferred to the Chair of the Functional Materials Research Group at the University of Saarland, Saarbrücken, Germany.

CHAP. 2: THEORETICAL FRAMEWORK

2.1. CRYSTALLOGRAPHIC STRUCTURE

The physical structure of solids is a consequence of the arrangement of atoms, molecules, or ions in space, as well as the interaction of the particles. Depending on this arrangement they can be amorphous or crystalline in nature. The first is characterized by the absence of a regular arrangement of atoms in the form of a crystalline lattice and a low melting temperature. A clear example of this amorphous material is glass.

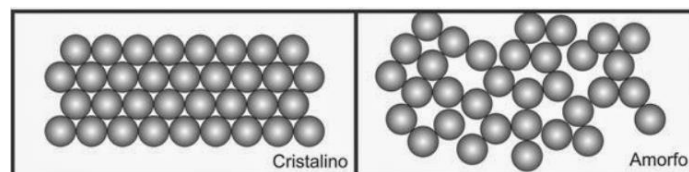


Fig. 1. Diagram of a crystalline and an amorphous structure [1].

On the contrary, in crystalline materials, e.g. metals, the atoms are arranged in space according to a geometrical order, forming a crystal lattice [2]. The atomic distribution (crystals) in solid crystalline bodies is formed as a result of the cooling of the liquid mass of metals and can be described by a spatial lattice in which the atomic positions are defined. In a crystalline material, it is always possible to distinguish a minimum set of atoms (unit cell or crystal), whose spatial distribution is similar and repeated. These elementary crystals have the properties of the corresponding material and when combined form a crystal lattice. This crystal lattice can be defined as a repetition in space of unit cells, which can adopt any of the 14 possible three-dimensional structures. The 14 Bravais lattices are shown in Fig. 2.

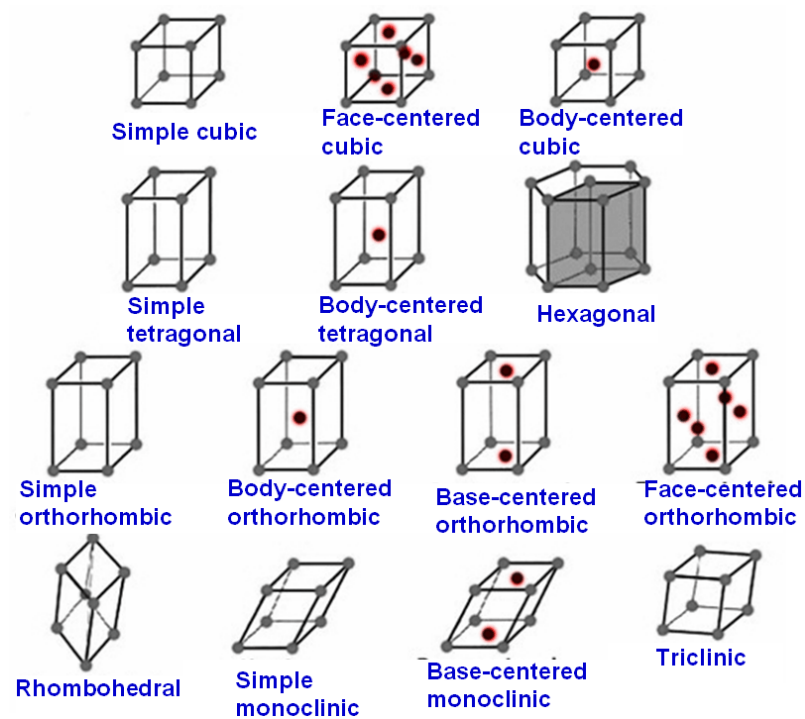


Fig. 2. The 14 Bravais' networks [1].

Metals, with a few exceptions, crystallize in only three structures: body-centred cubic structure (BCC), face-centred cubic structure (FCC), and compact hexagonal structure (HCP) [3]. The structure of real crystals differs from those mentioned above, as there are impurities that influence the crystallisation process. For this reason, the arrangement of real materials considered crystalline is not perfect, presenting imperfections such as point or dimensionless defects, linear (dislocations), one-dimensional and planar or two-dimensional [4]. Dislocations are one of the most influential defects in the mechanical behaviour of the crystal lattice. They deform the Bravais lattice in a row of points. The direction and magnitude of the distortions caused by dislocation can be represented by the Burgers Vector (b), which is shown in Fig. 3.

Dislocations can be of two types:

- The edge (or wedge) dislocation is formed by an extra plane of atoms in the crystal lattice. Its Burgers vector is perpendicular to the dislocation line.
- The screw (or helical) dislocation is formed when a shear stress is applied to a perfect crystal that has been separated by a shear plane (shear). Its Burgers vector is parallel to the dislocation line.

The most common scenario is for the two types of faults indicated above to occur concurrently, resulting in mixed dislocations. The Burgers vector is not perpendicular nor parallel to the dislocation line, but instead maintains a constant orientation in space. [4].

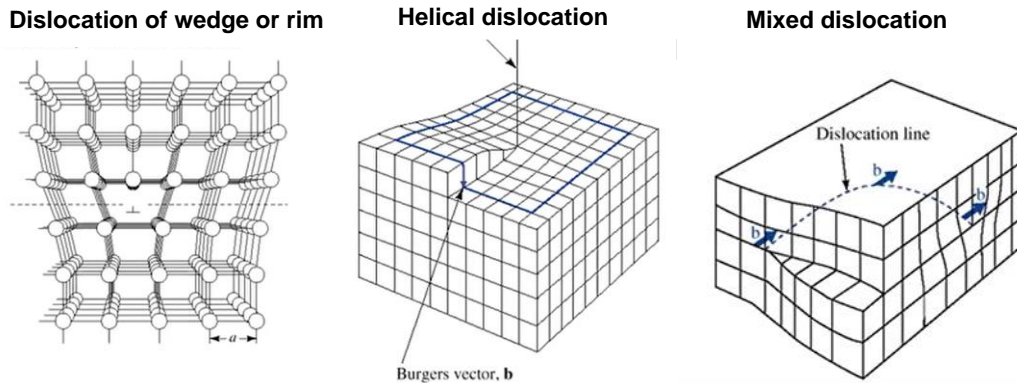


Fig. 3. Types of dislocations: wedge, helical and mixed dislocations, respectively [5].

The dislocations' motions allow for plastic (irreversible) deformation. It can be said that the dislocations discretely transport the plastic deformation. Shear stress would be considerably larger in the absence of dislocations. Therefore, dislocations in the crystal structure of metals are responsible for the ductility of the material, i.e. the presence of these imperfections is directly related to the ability of a metal to resist plastic deformation without breaking [6]. The plastic deformation capability of the different crystalline formations is related to the slip systems they present. The sliding system is defined as a collection of symmetrically identical sliding planes connected by a family of directions in which dislocation motion can easily occur and cause plastic deformation. These systems arise due to the application of external forces on the crystal structure, causing its parts to slide over each other. Sliding does not take place on a single plane, but rather on small sections of parallel planes known as slip bands or slip lines [7]. A three-dimensional schematic of the movement is shown in Fig. 4 and can be compared to the movement of a caterpillar track, where minor displacements generated by small repeating loads can lead to massive translations.

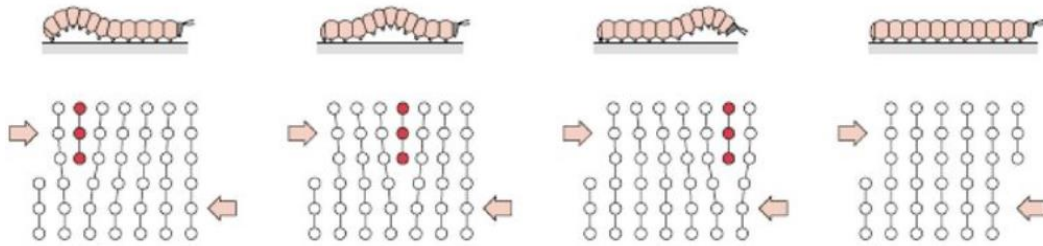
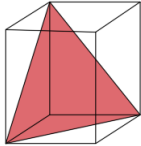
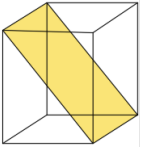
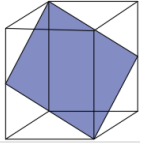
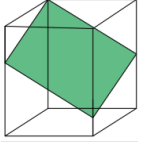


Fig. 4. Exemplification of a linear dislocation sliding system [8].

Each crystalline structure has a different number of slip systems and a different direction, which governs the response of each to stress application. Table 1 shows the packing factors, slip systems, and directions for each of the three crystalline structures FCC, BCC, and HCP.

Crystal structure	Packaging factor	Representation	Slip plane	Slip direction	N° of non-parallel planes	Slip plane	N° of slip systems	Total N° of slip systems
FCC	0.74		{111}	$\langle 1\bar{1}0 \rangle$	4	3	12 = (4x3)	12
			{111}	$\langle \bar{1}11 \rangle$	6	2	12 = (6x2)	
BCC	0.68		{112}	$\langle \bar{1}11 \rangle$	12	1	12 = (12x1)	24
			{123}	$\langle 11\bar{1} \rangle$	24	1	24 = (24x1)	

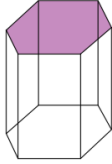
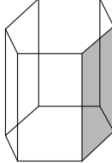

			$\{0001\} \langle 11\bar{2}0 \rangle$	1	3	$3 = (1 \times 3)$	
HCP	0.74		$\{10\bar{1}0\} \langle 11\bar{2}0 \rangle$	3	1	$3 = (3 \times 1)$	12
			$\{10\bar{1}1\} \langle 11\bar{2}0 \rangle$	6	1	$6 = (6 \times 1)$	

Table 1. Slip planes and slip directions for FCC, BCC, and HCC crystallographic structures [9].

As shown in the table, the FCC and HCP crystals have a denser family of planes than the BCC structure due to their higher packing factor. It should be noted that for the BCC structure, there are dislocation slips in planes of the $\{112\}$ and $\{123\}$ types, each with a single dense direction $\langle 111 \rangle$, depending on the material and temperature. The dense plane in HCP crystals is the basal plane (0001) , with the dense directions (three of them) of the $\langle 11\bar{2}0 \rangle$ type. Because of the small number of slip systems in HCP crystals, these metals are difficult to plastically deform. As a result, HCP crystals are susceptible to creep deformation. Furthermore, HCP metals are generally more brittle than BCC or FCC metals. This is because the ductility of a material is determined by the density of the slip planes and the number of slip systems. Despite having a lower slip number, metals with an FCC structure are more ductile than BCC because they have denser planes.

2.2. HYPOEUTECTIC WHITE CAST IRONS

Since the start of the Industrial Revolution, iron castings have been an essential part of the engineering scene. Therefore, it is easy to lose sight of their present importance

compared with more recent developments in materials technology. Nevertheless, there is no doubt that cast irons are indispensable engineering materials.

Based on the metastable phase diagram of the iron-carbon system at a lower carbon concentration (Fig. 5), a ferrous alloy with more than 2.06 wt.% of carbon is considered cast iron, and below is considered steel. Between 2.06 and 4.3 wt.% of carbon, the alloy is a hypoeutectic cast iron (hypo means “less than”). At a carbon content of 4.3 wt.%, a eutectic transformation takes place at 1147°C: the residual melt crystallizes at a constant temperature to form the eutectic (ledeburite-I). Both the primary austenite and the austenite crystals contained in ledeburite-I precipitate cementite as cooling progresses due to the decreasing solubility of the carbon. Consequently, the microstructure in this state consists of ledeburite-I and the primary austenite embedded therein as well as the precipitated cementite (F_3C). At 723 °C the eutectoid composition in the austenite crystals is finally reached (both in the primary crystals and in the eutectic). Above 4.3 wt.%, the alloy becomes hypereutectic (hyper means “greater than”) [2], [10], [11].

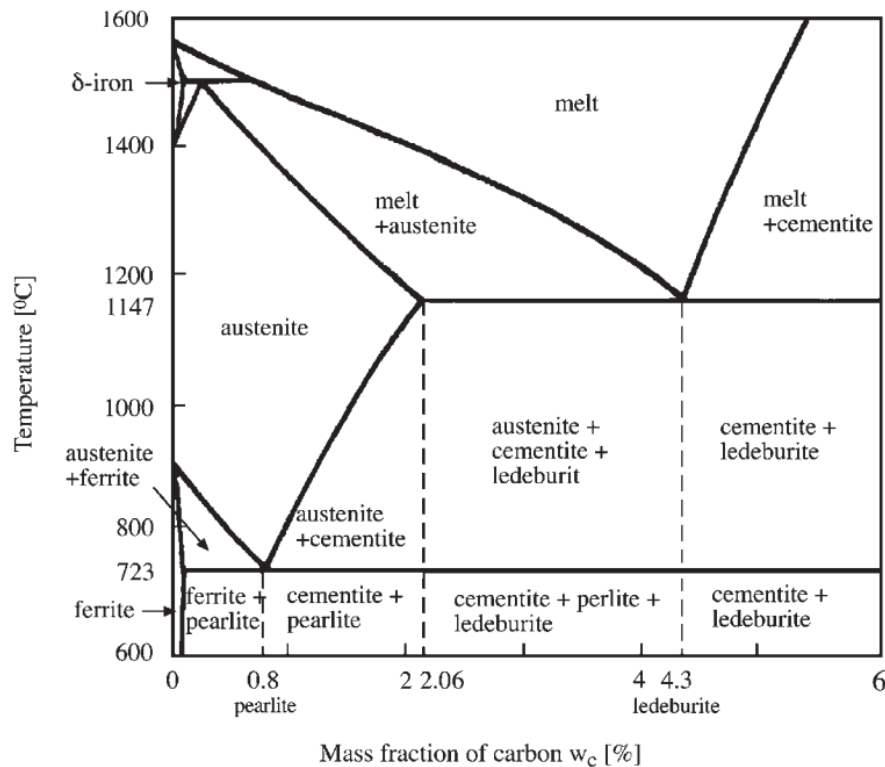


Fig. 5. Metastable phase-diagram of the iron-carbon system at a lower carbon concentration [10]

The high amount of carbon in cast iron exceeds the solubility of this element in ferrite and/or austenite and promotes the precipitation of a carbon-rich phase during solidification, which remains during cooling to room temperature; this phase can be either a carbide or graphite. Therefore, the final structure of cast irons is composed of a metallic matrix and carbide or graphite, depending on the chemical composition and the solidification rate [12]. The alloy composition does not only determine the difference in solidification temperature between these types, but still, the ease of nucleation also rests on the presence of other minor phases that could act as nucleants [13]. If the carbon-rich eutectic constituent is either cementite or an alloy carbide, the alloy is called “white cast iron”. On the other hand, if graphite precipitates, they are called “grey cast iron” [14]. As only white cast iron (WCI) was studied, particularly the one with high chromium alloy content, the following parts will only deal with them.

During the solidification of a hypoeutectic cast iron, dendrites of austenite (Fig. 6(a)) with a face-centred-cubic (FCC) crystalline structure grow in the liquid melt. At the eutectic point, the austenite will have a C content of around 2% and the remaining liquid will have a C content of around 4.4%. This remaining liquid then undergoes a eutectic

reaction, forming both austenite and carbide phases. These crystalline phases grow in a coupled manner, i.e., the austenite and carbide grow at approximately the same rates. At the end of solidification, the microstructure consists of primary austenite dendrites and a mixture of eutectic austenite and carbides [15]. Fig. 6(b) shows a microstructure of a 16 wt.% Cr high chromium cast iron (HCCI) in the as-cast condition, in which those dendrites (red arrows) and eutectic carbides (black arrows) are shown.

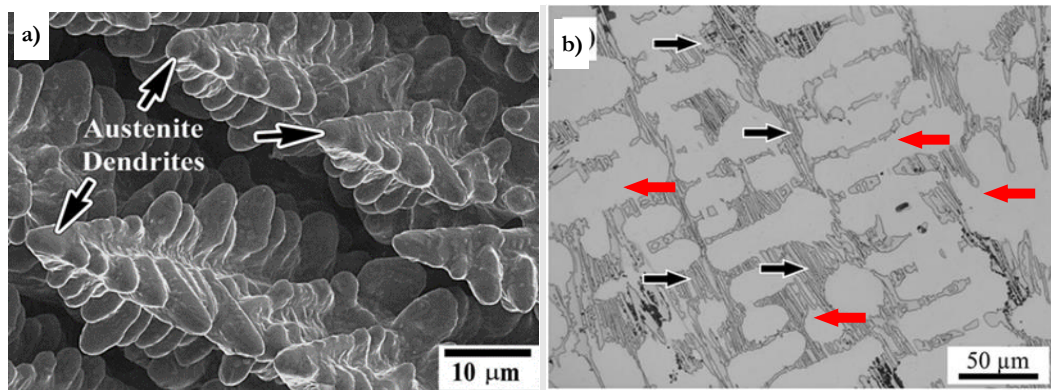
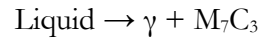


Fig. 6. a) 3D SEM image of Primary austenite dendrites during solidification of a high-Cr iron before the eutectic reaction takes place [15], and b) Optical microscopy image of the as-cast condition of 16 wt.% Cr HCCI [16].

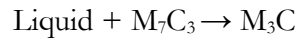
2.3. HIGH CHROMIUM CAST IRONS (HCCI)

When toughness, abrasion, and, in a few cases, corrosion resistance is critical, the high-Cr family of white cast irons is hard to surpass. HCCI have been around since the early 1900s and, historically, were the first true, alloyed abrasive resistance irons in commercial production [12], [14].

The high chromium content leads to the formation of a large volume fraction of eutectic chromium carbides within a metal matrix. This provides the hardness needed for crushing and grinding other materials in abrasive and erosive environments and gives good resistance to corrosion and oxidation at high temperatures. In addition, the high but precise percentage of chromium present in the casting helps to delay graphite formation and stabilize the carbides [17]. In the case of HCCI, as the material solidifies, austenite dendrites form until the temperature decreases to a level where the eutectic reaction, given by the line U_1-U_2 in Fig. 7, takes place. This reaction is described as:



where M_7C_3 is the eutectic carbide that forms (M represents the metallic species and is most commonly iron and chromium). Even though most of the HCCI solidify completely within the eutectic region (square in Fig. 7), a peritectic reaction may occur if liquid metal remains when the temperature reaches U_2 . Then, the following reaction takes place:



Then, an M_3C wall forms on the M_7C_3 carbides, inhibiting contact between the M_7C_3 carbides and the liquid [18].

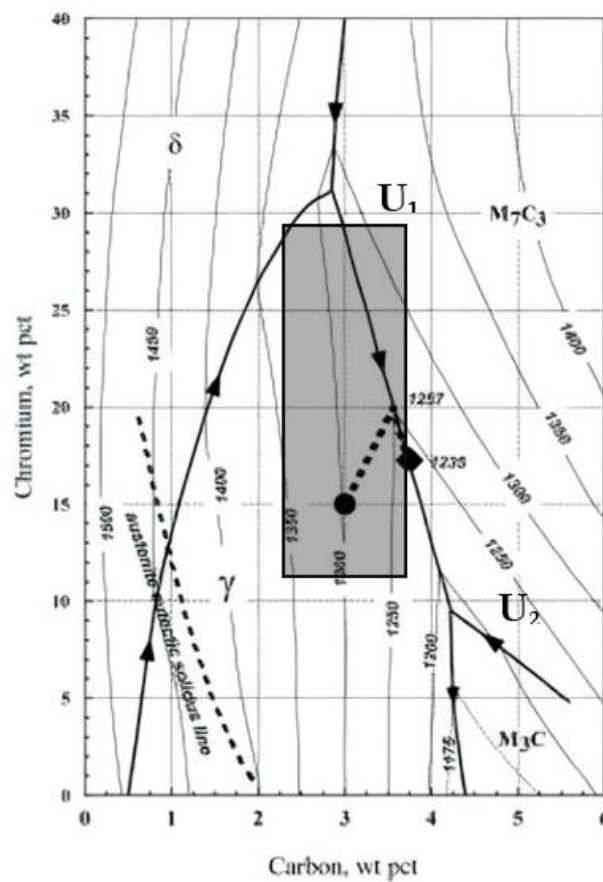


Fig. 7. 2D view of the Iron rich corner of metastable C-Cr-Fe liquidus surface: rectangular box indicates the compositional range of hypo-eutectic white cast iron alloys commonly used. Image-based on [14], [19].

2.4. MICROSTRUCTURAL CONSTITUENTS

As mentioned above, the microstructure of an HCCI is composed of a metallic matrix (austenite, ferrite, perlite, bainite, or martensite) and carbides (eutectic, and could have or not secondary ones depending on the heat treatment (HT)). Understanding the nature and morphology of both constituents is essential to determine its response against wear and further applications.

2.4.1. MATRIX

The first phase to solidify is austenite, which has a face-centered-cubic (FCC) crystal-line structure and grows in form of dendrites. As the primary austenite dendrites grow during the solidification process, the remaining liquid becomes enriched in C and Cr, and its representative point is pushed diagonally toward the eutectic valley (Fig. 8). As the liquid reaches the eutectic, it starts to form eutectic colonies of austenite and carbides ($\gamma + M_7C_3$). Fig. 8 exemplifies the solidification process for an HCCI with 15 wt.% Cr and 3wt.% C. As the alloy continues to solidify, the remaining eutectic liquid moves down the eutectic valley, decreasing in temperature [14], [19], [20]. Further decrease in temperature to ambient temperature leads to metastable austenite retaining. This retaining has been attributed to the presence of high contents of alloying elements and carbon that can inhibit pearlite formation and decrease the martensite start temperature M_s below room temperature.

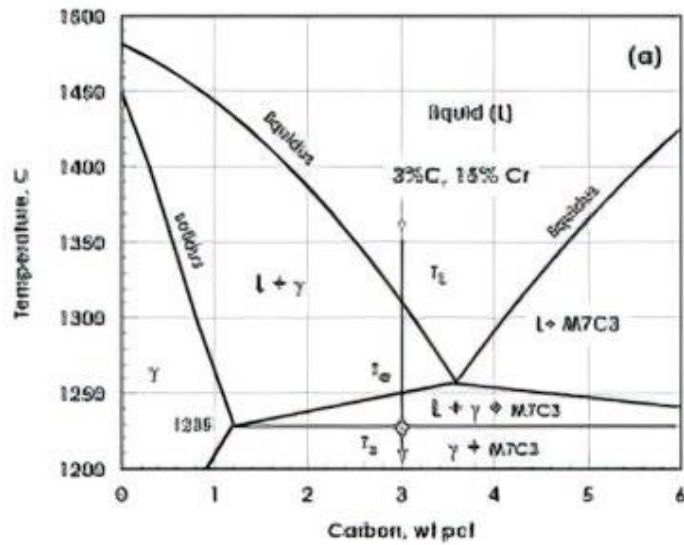


Fig. 8. Iron-rich corner of the Fe-Cr-C metastable liquidus diagram, for 15 wt.% Cr and 3wt.% C HCCI [14].

Primary austenite has been found to contain a higher amount of chromium than eutectic austenite. It is postulated that the formation of the eutectic carbides in contact with the primary austenitic phase has led to excessive consumption and thus matrix depletion of C and Cr. Consequently, the M_s temperature in this localized interfacial regime has increased. As a result, martensite has formed at the periphery of the primary carbide particles [21], [22]. A closer examination of Fig. 9 reveals that the eutectic carbide particles are surrounded by a thin white zone, which has been associated with the formation of martensite. Therefore, during the casting, the matrix does not turn into martensite.

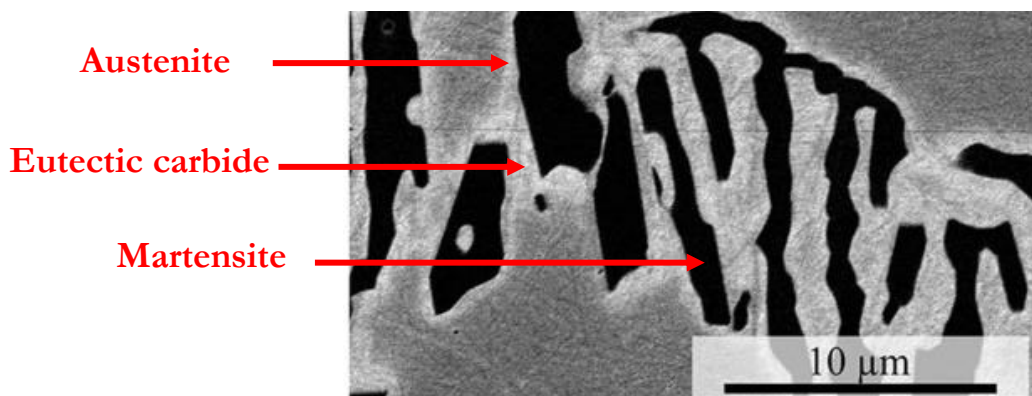


Fig. 9. SEM (BSE) images for As-cast 16wt.% Cr HCCI at different magnifications from left to right x500, x2000, and x6500, respectively. Image-based on [16].

2.4.1.1. MARTENSITIC TRANSFORMATION

The martensitic transformation is athermal, i.e., it occurs without diffusion. Because Martensite is an out-of-equilibrium phase, is unstable, and its essential properties, consisting of high hardness, although accompanied by high brittleness, make it an important alternative in those components requiring high resistance to frictional wear, high elastic limit, and fatigue resistance. When a hypoeutectic iron casting of 1.6 wt.% C, for example, is cooled slowly from the austenitic field, the final structure obtained is cementite-pearlite; on the other hand, if the cooling is rapid, diffusion does not take place. This does not prevent allotropic change, so the austenite is still transformed, but maintaining the C content; the structure obtained is called martensite, and its lattice, as shown in Fig. 10, is body-centered tetragonal (BCT). The system tries to adopt the BCC lattice, but the excessive C content, whose atoms still occupy the interstices between the Iron atoms, distorts the lattice, making it tetragonal. The result can be considered a ferrite very oversaturated in C. As the diffusion mechanism does not participate, the transformation takes place by shearing, consisting of a cooperative movement of the Fe atoms which, moving only a fraction of the interatomic distance, pass from the lattice point they occupied in the austenite to the corresponding lattice point in the martensite.

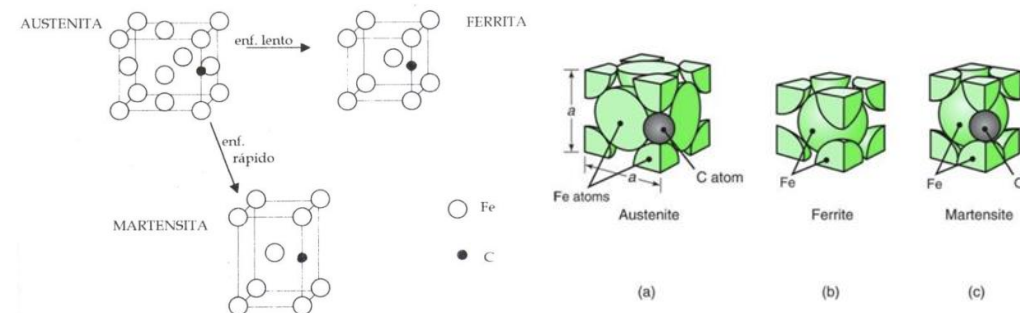


Fig. 10. Austenite and martensite unit cells showing carbon atom position [23], [24].

2.4.1. EUTECTIC AND SECONDARY CARBIDES

Depending on the amount of chromium of the HCCI, different types of eutectic carbides could precipitate. Chromium levels below 12 wt.% result in the presence of M_3C carbide type with a hardness of around 1,000 HV_{0.01} [20]. Below 6 wt.% Cr, eutectic carbide is an M_3C type in a continuous form which limits toughness [25]. When the amount

of Cr is about 8-10 wt.% Cr, the eutectic carbides are less continuous and can be duplex, consisting of an inner core of M_7C_3 and an outer shell of M_3C forming during solid state cooling in the mold. Above 12 wt.% Cr, the form of the eutectic carbide changes to the M_7C_3 type with is described as discontinuous and lamellar [11].

The M_7C_3 carbides have a hexagonal crystalline structure, while the M_3C carbide is orthogonal; and due, in part, to its different crystalline structure, the M_7C_3 carbide is much harder than the M_3C carbide; approximately 1400 $HV_{0.01}$ versus approximately 1000 $HV_{0.01}$, respectively [14]. Given the inherited brittleness associated with the carbide, continuous precipitates are not favored for abrasion resistance, and therefore, discontinuous, and relatively tougher M_7C_3 carbides are advantageous [11].

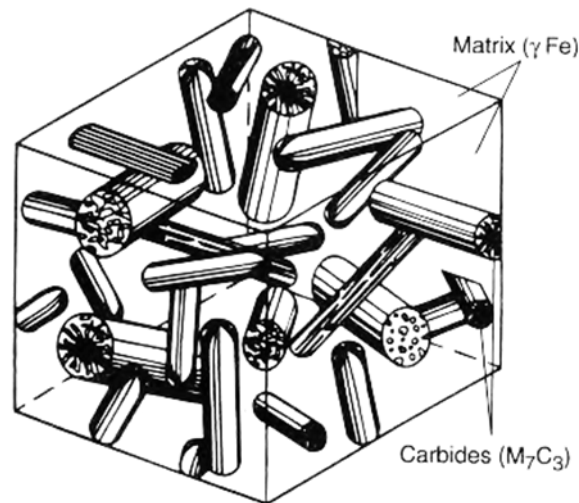


Fig. 11. Representation of a cube of High chromium White cast iron with M_7C_3 carbides [14].

The eutectic carbides consist of rod-like hexagonal pencil-shaped crystals, as Fig. 11 illustrates, which solidify as a colony structure. The rods join together to form blade-like structures which are often described as lamellar. The rod-like M_7C_3 carbides become finer with increasing chromium content and with an increasing rate of eutectic solidification [26].

Although these eutectic carbides improve the hardness and wear resistance of the system, this can be further improved by the precipitation of much finer and smaller carbides during latter HT, called secondary carbides (SC). SC precipitation begins very fine, very

densely, and randomly around eutectic carbides and some grain boundaries. It then progresses into austenite dendrites that are very close to each other along the preferred crystallographic planes.

It is the precipitation of secondary carbides which depletes the matrix of alloying elements, and hence destabilizes the austenite, so that on cooling a martensitic matrix is formed. The type of carbide that precipitates depend on the alloy composition and the destabilization temperature. Secondary carbides commonly precipitate on slip bands or subgrain boundaries within the austenitic regions. These slip bands and subgrain boundaries form due to the stresses generated by the difference in thermal expansion between the eutectic carbides and the matrix [18].

2.4.2. EFFECT OF ALLOYING ELEMENTS

In addition to chromium, there are other alloying elements that can be added to the casting to transform the microstructure. An increase in silicon content leads to a refinement of the dendritic structure and an increase in the eutectic carbide volume fraction. Silicon has a minimal effect on M_s temperature, but a major effect on reducing C solubility. This is why it is so effective in increasing the hardness (martensite content) of as-cast martensitic grades of high-alloy white irons [14]. However, for contents above 3%, a transformation of the austenitic matrix to pearlite occurred in preference to martensite [21], [27].

Boron additions to cast irons with 13%Cr [28], decreases the volume fraction of the matrix of austenite partially transformed into martensite, whereas the volume fraction of the eutectic carbides increases. The increasing of the boron content also decreases the space between dendrites' arms, but at the same time, the eutectic carbides become coarser. According to Bedolla et. al. [21], boron addition changes the morphology of carbides from interconnected, coarse, clustered rods to a parallel distribution of isolated fine rods. Also, the addition of boron, less than 195ppm, refine the carbide structure, which leads to an improvement of the wear resistance in HCCI up to 40% [29].

Molybdenum, with a content lower than 3%, is used to avoid pearlite formation. With more than 3wt.%, M_2C , and M_6C carbides are formed, leading to an increase in hardenability and wear resistance at high temperatures. Furthermore, it has been observed that M_6C carbides seem more contribute to enhance wear resistance than M_7C_3 carbides since some micro-cracks were observed in M_7C_3 and not in M_6C [22].

The typical amount of nickel is about 0.2 to 1.5%, and it is usually added in conjunction with molybdenum. Nickel contents higher than this range tend to excessively stabilize the austenite, leading to austenite retention [30].

The addition of titanium ($\leq 2\%$) leads to the precipitation of titanium carbides in the matrix, which increases the bulk hardness. Besides, the depth on which deformations occur is decreased by the increase of the titanium content, since the strengthened matrix offered an extra support for the eutectic carbides against cracking [27].

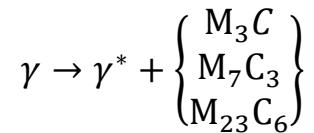
2.5. HEAT TREATMENTS (SOLID TRANSFORMATIONS)

During the production and use of high-chromium white iron, several solid-state transformations are exploited, as a consequence of various heat treatments. The main objective of most heat treatments is to destabilize the high-alloyed austenite so that on cooling the matrix is transformed into martensite. This process would give a harder matrix, and also allows the precipitation of SC, which would increase the hardness of the system. The most common heat treatment for HCCI is to destabilize the austenite at high temperatures and quenching. This treatment is usually followed by a subcritical destabilization step, which enhances further the precipitation of SC.

2.6. DESTABILIZATION HEAT TREATMENT

The as-cast metallic matrix of a HCCI is largely austenitic and will contain an excess of dissolved C, which stabilizes the austenite matrix. The principal role of heat treatment is to destabilize the austenite by reducing the C content via precipitation of secondary carbides. Carbide precipitation depletes the austenite of excess C and raises the martensite

transformation temperature (M_s) range to above room temperature. The heat treatment of commercial high-Cr white iron castings is commonly performed in the temperature range of 930 to 1060°C [14]. The reaction that takes place during the destabilization heat treatment has been described as:



Where γ^* is austenite of lower alloy content than the original austenitic matrix (γ) [31]. The type of secondary carbides formed (M_3C , M_7C_3 , or $M_{23}C_6$) depends on the matrix composition and the destabilization temperature. Although a predominantly martensitic matrix is formed after the destabilization treatment, up to about 35% austenite may be retained in the matrix. The amount of retained austenite is strongly dependent on the matrix carbon content following destabilization, which is influenced by the alloy composition, the time and temperature of destabilization, and the section size. The eutectic carbides are generally thought to be inert at the temperatures used and are unaffected by the destabilization heat treatment [18].

Maratray [20] investigated the carbide precipitation for many austenitic high-Cr iron alloys and a typical transformation diagram is shown in Fig. 12. The isothermal decomposition of the austenite occurs in two temperature ranges. Above the nose of the higher C-shaped curve, at about $975 \pm 25^\circ\text{C}$, precipitation of secondary carbides (SC) is observed. This area is divided into two portions: the one above the A_3 point corresponds to the transformation $\gamma \rightarrow \gamma + \text{SC}$; the other, below the A_3 point, corresponds to the transformation $\gamma \rightarrow \gamma + \alpha + \text{SC}$. The second C-shaped transformation range has a maximum rate at about 650 to 700°C, whose product of transformation is a very fine perlite structure.

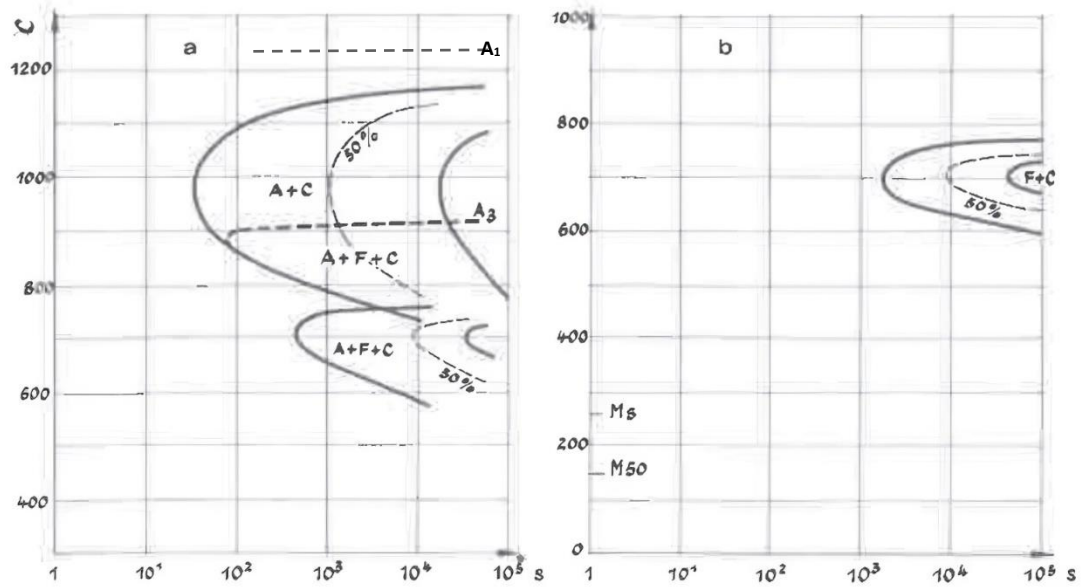


Fig. 12. Schematic isothermal transformation diagrams for HCCI: (a) undestabilized austenite, (b) austenite destabilized by precipitation of secondary carbides [20].

According to Maratay experiments [20], X-ray analysis only showed secondary carbides of the type M_7C_3 after precipitation at temperatures above the A_3 line in Fig. 12. On the other hand, the $M_{23}C_6$ carbide has been observed after holding between A_1 and A_3 . Because of the presence of eutectic M_7C_3 carbide, it is impossible to determine whether only the $M_{23}C_6$ carbide is formed in this temperature range and if it is stable on long holding.

CHAP.3: STATE OF THE ART

3.1. DESTABILIZATION HEAT TREATMENT OF HCCI

As mentioned in section 2.4, the role of the destabilization heat treatments in the enhancement of wear resistance and toughness of HCCI is very important. During the process, extensive precipitation of SC takes place together with the austenitic matrix transformation into martensite during cooling. Several research have been carried out to decipher the nature, morphology, and mechanisms of matrix modification and secondary carbide precipitation during destabilization heat treatments. Asensio et al. [32] provide a first approach of the carbide phases (primary and secondary) present, depending on the chemical-composition of the as-cast alloy. Powell and Laird [31], examined the morphology, structure, and growth sequence of secondary carbides, as a function of the Cr content and the destabilization treatment parameters. They observed that by increasing the Cr content, the stoichiometry of the secondary carbide followed the sequence M_3C , M_7C_3 , and $M_{23}C_6$. Their morphology varied from rod like, for M_3C and M_7C_3 , to fibred like, for $M_{23}C_6$. In all cases, in concordance with Tabrett [18], precipitation of secondary carbides took place within the austenitic grains without any evidence of preferential growth from the eutectic carbides.

Bedolla-Jacuinde et al. [33], widely studied the effect of destabilization treatment parameters on the nature and morphology of secondary carbide precipitation. In their work, destabilization of a 17wt.% Cr, 2wt.% Mo, 2wt.% V, 1.8wt.% Ni white cast iron was carried out at 900, 1000, and 1150 °C for 5 min up to 8 h. They reported that decreasing temperature decreases the precipitation of secondary carbides. They also observed that high temperatures stabilized an austenitic phase free of secondary carbide precipitates. At 900 and 1000 °C, the extent of carbide precipitation increased with time, reaching a maximum, then decreased due to dissolution or coarsening phenomena. In their work, the highest hardness values were obtained after destabilization at 900 °C for 1 to 2 hours; these conditions ensured an optimal combination of martensite and finely dispersed secondary carbide precipitates. Karantzalis et. Al. [34], reported that for a 18wt.% Cr,

0,3wt.% Mo, the maximum values of hardness are obtained at 1000°C, due to the optimum combination of carbide precipitation, carbide particle morphology, as well as extent of martensite formed. Above 1000°C, dissolution of carbides takes place, leading to stabilization of the austenitic phase, which represents a diminution of the hardness.

The precipitation of SC during a subcritical destabilization heat treatment for HCCI and the standard quenching procedure, i.e., holding temperatures above the critical line (from 0.5 to 4 h) before cooling in air, has previously been described [35]. Multi-step treatments have been proposed (martensite formation and post-quench subcritical annealing for carbide precipitation), with a significant secondary carbide precipitation, although the intermediate air cooling induced a sharp decrease in mechanical properties. The decrease in mechanical properties was associated with the formation of ferritic phases in the subcritical step. In general, subcritical treatments have been associated with hardness reduction [36]. Furthermore, the type, size, and distribution of secondary carbides formed during the destabilization depend on the composition and destabilization temperature. The secondary carbides are efficient for improving the abrasion resistance [37]. Guitar et al. [38]. proposed a destabilization technique consisting of a multi-step HT, where the sub-critical process is carried out directly following the destabilization of the austenite. Later, a second destabilization step was performed followed by a quenching in air. The implementation of this multi-step HT to HCCI 16%Cr showed an improvement of 69% in the wear resistance in comparison with the destabilized and quenched material. In another research, Guitar et al. [38], performed thermodynamic and kinetic calculations with MatCalc software about the multi-step HT performed in [16], but for a 26wt.% Cr in order to evaluate the applicability of a successful HT to a material with a different chemical composition and therefore to assess the influence of the Cr content on the modified microstructure. The result of the simulation is presented in Fig. 13.

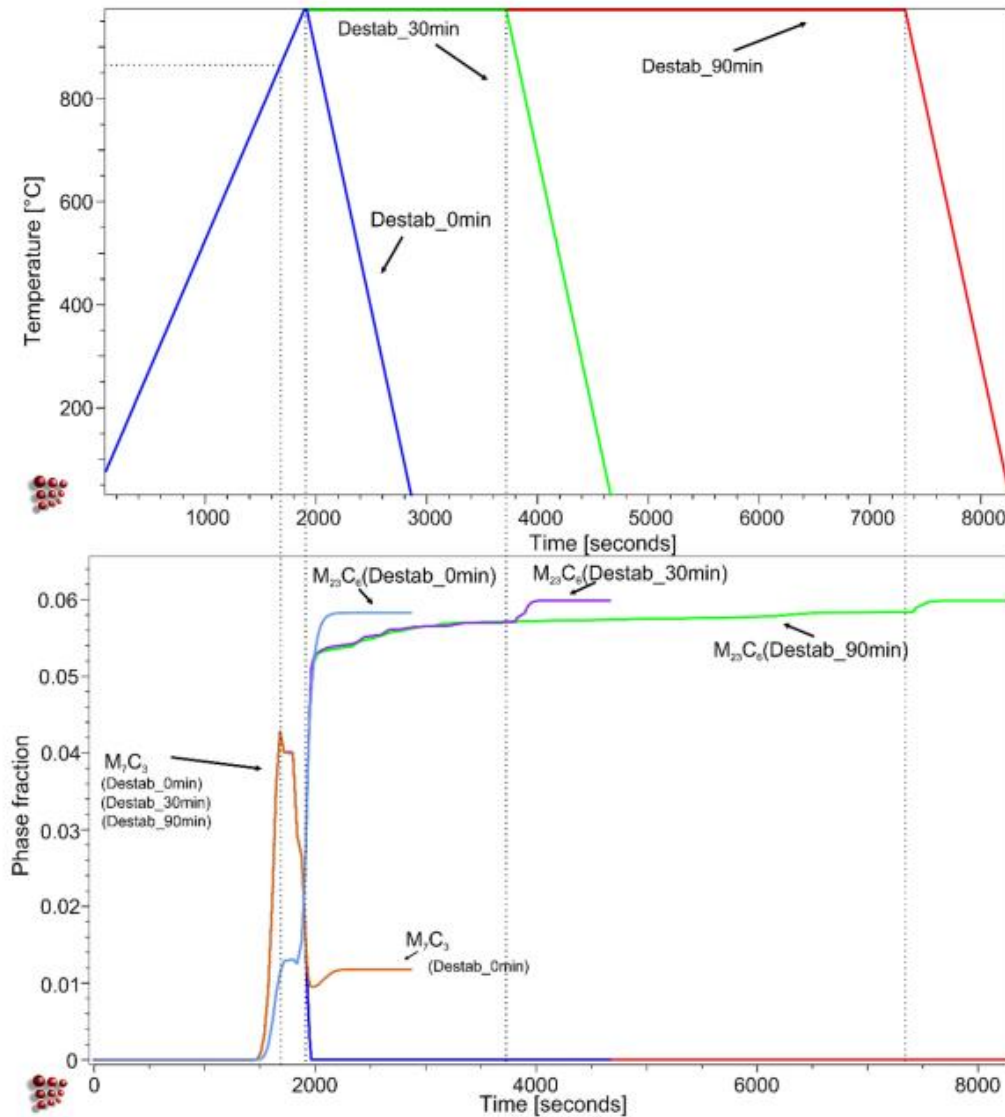


Fig. 13. Destabilization process at 980 C for different times (0, 30 and 90 min) calculated using MatCalc and the corresponding SC type and fraction. Thermal cycle for the destabilization process (on top) and the SC type and fraction during HT as a function of time (low) [38].

Thermodynamic and kinetic calculations of the destabilization process showed that M_7C_3 are the first to precipitate during heating of a 26%Cr HCCI. After destabilization temperature is reached, they completely transform to $M_{23}C_6$, which grow throughout the holding time. Further precipitation of $M_{23}C_6$ occurred during cooling, in the temperature range 980–750°C. The SC precipitated at this point are observed in the quenched samples in the area in contact with the EC. This research is one of the only ones that showed, through simulation, what happens during the heating process at the beginning of HT.

With basis on the previous HT simulations of a 16wt.% Cr and 26wt.% Cr HCCI, where it was found that the precipitation of secondary carbides of the M_7C_3 begins at

about 780-800°C, the present work will focus on heating the material up to 800, 900 and 980°C, in order to corroborate simulation results and understand the precipitation mechanisms.

3.2. WEAR AND TRIBOLOGY

Tribology can be defined as "the branch of science and technology concerned with surfaces interacting in relative motion and related issues", and includes the study of friction, wear, and lubrication [39]. Thus, as Fig. 14 shows, a tribological system can be defined by two materials (solid body and counterbody with their surface properties) interacting within an interfacial element, and the environment (humidity, temperature, pressure, present of lubrication). However, friction and wear are not intrinsic properties of materials, but characteristics of the tribological system [40].

Wear is a material degradation process which causes progressive material removal from the surface of a component as a result of relative motion between the contacting surfaces, with or without the presence of other substances such as lubricants, wear debris and abrasive particles. C. Kajdas et.al [41] described wear as "undesirable continuous loss of material from one or both of the surfaces of mating tribological elements due to relative motion of the surfaces". It is well known that every object interacts with its environment through its surface. Therefore, there is a great need to understand surface interactions, as many different physical or chemical interactions can occur on surfaces, such as wear, corrosion, adhesion, friction, abrasion, etc. Therefore, the study of this wear mechanism, surface properties and interactions between two surfaces leads to the development of new engineering materials or surface modifications. It is worth noting the importance of the surface in these interactions, as in most cases, its properties are different from those of the bulk and in a way, it is the barrier/fence between the bulk and the environment. An example of this could be corrosion or processing techniques that might change the chemical distribution of the surface, but not that of the bulk.

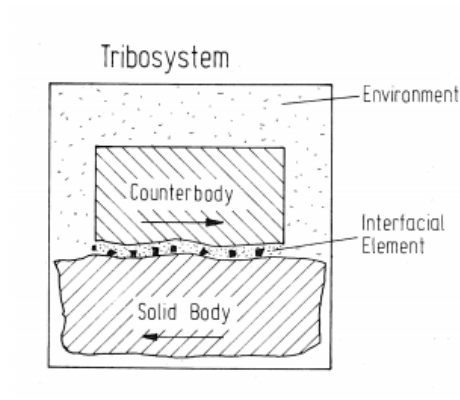


Fig. 14. Schematic representation of the elements of tribo-system [40].

There are several wear mechanisms, each one depending on the tribological system. According to [40], [42], there are four main wear mechanisms:

- 1) adhesive wear,
- 2) tribo-oxidative (tribochemical) wear,
- 3) abrasive wear,
- 4) wear by contact fatigue.

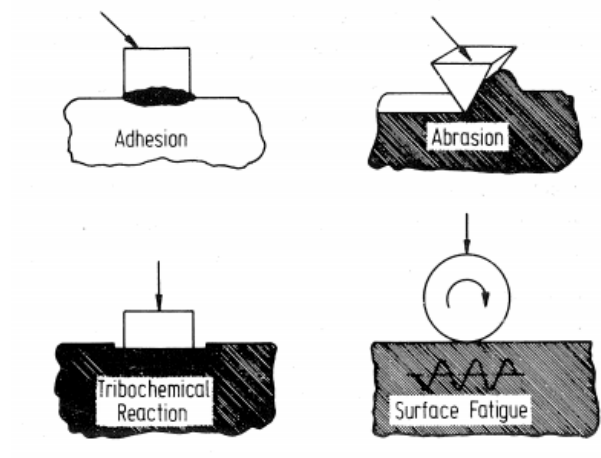


Fig. 15. Schematic description of the four main wear mechanisms [40].

During a tribological test, several different wear mechanisms could take place. For example, on the abrasive wear, two different processes can act: two- or three-body wear (Fig. 16). Two-body abrasive wear is exemplified by the action of sandpaper on a surface. Hard asperities or rigidly held grits pass over the surface like a cutting tool. In three-body abrasive wear the grits are free to roll as well as slide over the surface, since they are not held rigidly [43].

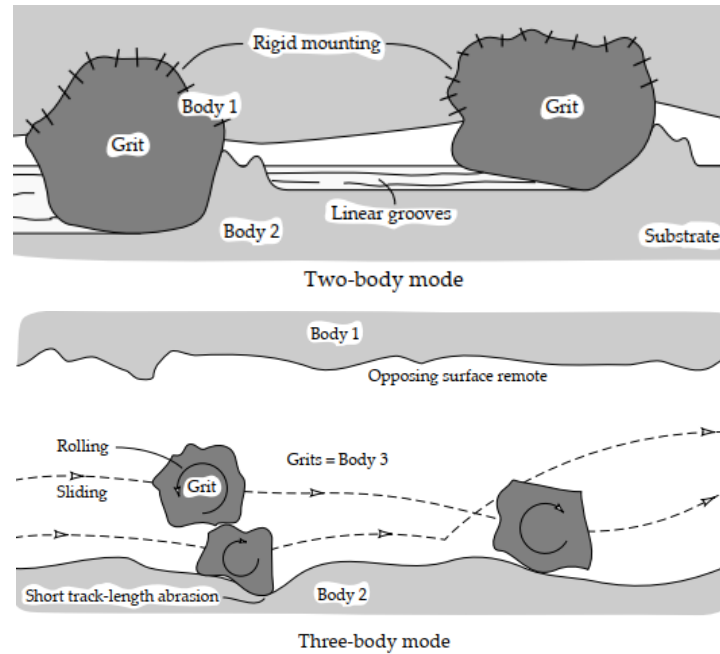


Fig. 16. Two and three-body modes of abrasive wear [43].

To analyze the response of a material to these wear mechanisms, there are several tribological test that are able to perform. They can be classified as closed or open systems. The first one is used when the study of both bodies in contact is needed, in contrary to open systems, where only the solid body is studied. The tribological test chosen for this project is the ball-on-plate test, which consists of a linear sliding movement between a plate body and a ball, with a certain load on the ball. Classical parameters of this tribological test are the sliding rate, the material of both ball and sample, the number of cycles, the load applied to the ball, and the environment (temperature, pressure, humidity).

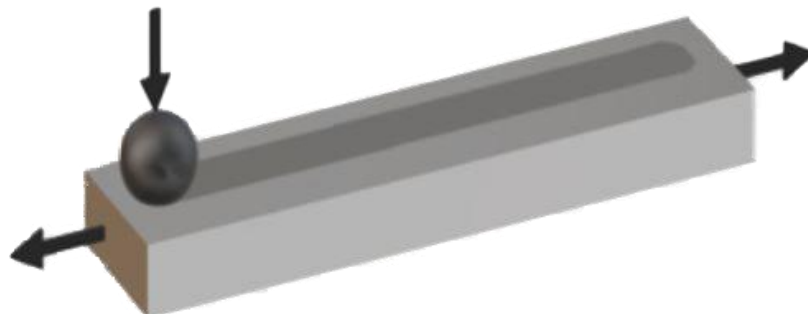


Fig. 17. Ball-on-plate tribological test [44].

On the sliding tests, the contact between surfaces of solids at moderate pressures is limited to contacts between asperities of opposing surfaces. Most forms of wear are the result of events occurring at asperity contacts. There could, however, be some exceptions to this rule, e.g., erosive wear which involves hard particles colliding with a surface. Holm and Archard [45] developed a model in which the total wear volume is proportional to the real contact area times the sliding distance. A coefficient ‘K’ which is the proportionality constant between real contact area, sliding distance, and the wear volume has been introduced, i.e.[46]:

$$V = K A_r l = K l \frac{W}{H}$$

Where:

- V is the wear volume [m³].
- K is the proportionality constant.
- A_r is the real area of the contact [m²].
- W is the load [N].
- H is the hardness of the softer surface [Pa].
- l is the sliding distance [m].

The ‘K’ coefficient, also known as the ‘Archard coefficient’ is widely used as an index of wear severity. The coefficient can also be imagined as the proportion of asperity contacts resulting in wear. The value of ‘K’ is never supposed to exceed unity and in practice ‘K’ has a value of 0.001 or less for all but the most severe forms of wear. The low value of ‘K’ indicates that wear is caused by only a very small proportion of asperity contacts. In almost all cases asperities slide over each other with little difficulty and only a minute proportion of asperity contacts result in the formation of wear particles. Several works focus on the influence of alloying and carbide volume fraction (CVF) on the final wear properties of the HCCI alloys [27], [28], [47]. These studies are devoted to find the optimum CVF for a given chemical composition to obtain the maximum hardness, which was initially associated with high wear resistance, as empirically demonstrated by Archard [45]. Due to a large body of research, it is now known that many factors contribute to the overall wear resistance, such as carbide type, morphology, volume fraction, and its interaction with the host matrix. Therefore, the overall wear resistance can be considered a

synergistic contribution between the carbide and the surrounding matrix [32], [48] The high hardness of M_7C_3 carbides is known to confer high wear resistance to the HCCI alloy. However, the matrix as such also plays a fundamental role in wear because it acts as mechanical support [14]. This was demonstrated in the study by Doğan et al. [37], in which increasing the CVF did not necessarily increase the wear resistance of the HCCI alloys examined. Therefore, it can be said that the wear behavior of a material is not an inherent property, but is defined entirely by the system and, in this sense, the hardness of the carbides contributes in part to the wear resistance [40].

Studies have shown that having a pearlitic and ferritic matrix should be avoided, as their presence will reduce wear and fracture resistance [11], [49]. Instead, austenite in general provides better mechanical support for carbides compared to pearlite/bainite due to its ability to absorb crack propagation and progressively harden during service [39], [40]. This was verified in the work by Doğan et al. [37], where it was observed that HCCI with an austenitic matrix and a CVF of 28% showed a decrease in volume wear rate of almost 50% compared to the alloy with a pearlitic/bainitic matrix that had a CVF of 45%. On the other hand, studies indicate that a harder martensitic matrix may not be the most optimal choice [37], [49]. In addition, numerous studies indicate a tendency for wear resistance to increase with increasing CVF when a softer abrasive than M_7C_3 carbide is used, although there is no consensus in the community when the hardness of the counterpart exceeds that of the carbide, as in the case of silicon carbide or alumina (SiO_2 and Al_2O_3 , respectively) [48]. Finally, several studies have shown that heat treatment modifications performed on HCCI alloy as the cast have improved wear resistance [16], [50]–[52]. Thus, wear behavior is not only influenced by the microstructure of the HCCI alloy, but also by other factors such as the experimental environment, loading conditions, relational motion of the contact surface, abrasive type, and hardness [14]. This only elucidates the complexity and variables associated with tribological testing.

Among the multitude of studies dealing with wear in cast irons, only a limited number of investigations dealt with creep wear [14], [21], [53] and even fewer studies emphasized the matrix modifications that take place during creep [27], [38], [54]. It is believed that, in addition to dislocation interactions, strain-induced martensite (SIM) formation also contributes to the work hardening behavior of austenite [55]. Although the transformation of austenite to martensite under abrasion is mentioned by Pokusová et al [56], it is not described as such. The ability of the austenite matrix to plastically deform during service and

its ability to form SIM gives scope for improving the creation of a self-replacing wear-resistant surface, increasing the longevity of wear parts [11], [49]. Nayak et al. [57] performed linear dry sliding tribological tests on a 26% Cr cast HCCI alloy with varying loads. Loads of 5, 15, and 20N were applied. The critical load (P_c) is defined as the load at which the onset of plastic deformation occurs in the material, which was determined by Nayak by applying the Hertzian contact theory. This was found to be ~ 15 N for the austenitic phase in 26%_HCCI. In that work, the dominant wear mechanism was adhesion with signs of mild abrasion at loads below P_c , but at loads equal to and above P_c , the dominant wear mechanism was observed to change to abrasion. The increased tendency to spalling, together with the propensity for strain hardening of the austenitic matrix, resulted in poor mechanical stability. Furthermore, in the present work, 20N linear dry sliding tribological tests on a 16% Cr cast HCCI are performed, in order to determine its resistance to wear resistance in the different conditions: 800, 900, and 980°C.

CHAP. 4: CHARACTERIZATION METHODS

In this section, a brief overview of the different characterization methods will be given. The focus will be on their basic working principle and the information that can be obtained by the application of these methods.

4.1. SCANNING ELECTRON MICROSCOPE (SEM)

The scanning electron microscope (SEM) is based on the principle of interaction between electrons and matter to produce high-resolution surface images. Unlike optical microscopes that reflect a beam of light to form the image, an electron microscope uses a beam of electrons that "reflect" differently as they interact with the surface, allowing a very realistic image to be displayed, albeit only in greyscale. Compared to an optical microscope, the SEM has a greater depth of field, i.e., it can focus on a larger part of the sample, even though the sample has different heights. Therefore, it allows the characterization of a specimen's surface observing its topography, irregularities, and compositional variations [58].

The structure is a vertical column with a small lower chamber where the sample, which must be under vacuum, is introduced (Fig. 18). At the top of the column, there is a tungsten, gallium, or argon filament, which is heated and acts as the source of the electron beam, which is accelerated by the application of a voltage between 50 V and 30 kV. Unlike optical microscopes that use lenses to focus the light beam, these microscopes use electromagnetic coils to condense and focus the electron beam. The scanning coils are responsible for constantly scanning over the region of interest in the sample, obtaining point-by-point data to generate the graph on the screen.

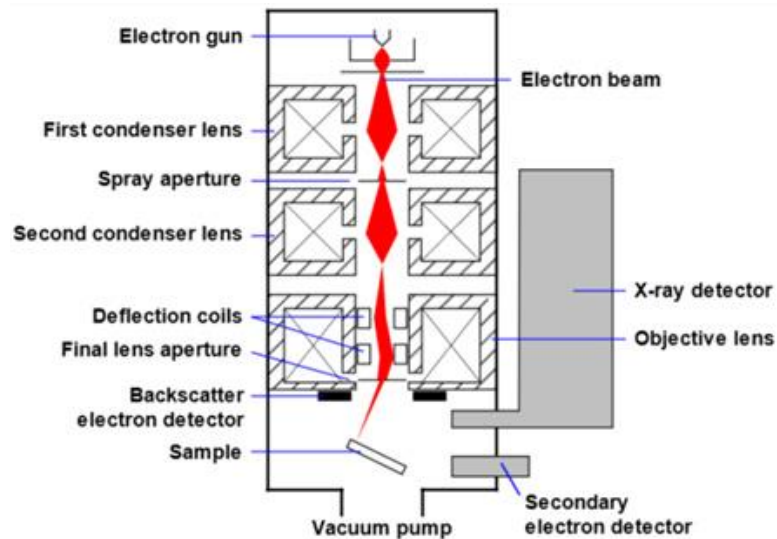


Fig. 18. Scheme of a SEM (extracted from NanoScience Instruments, 2016) [59].

The SEM utilizes electromagnetic lenses to focus a beam of electrons towards the specimen's surface. When an electron beam hits a sample, it generates several signals (Fig. 19) that are picked up by different sensors located in the SEM column. Each of these signals are used for a different kind of analysis. They can be electrons, such as *secondary electrons*, which are used to generate the image in most SEMs, *backscattered electrons*, which are also used to generate the image or Auger electrons. Depending on the energy the secondary electrons possess (intensity detected), the image shown has a higher or lower contrast and brightness level [58], [60]. In addition, the impact of the beam on the sample generates X-rays, which are captured with a device for *energy-dispersive spectroscopy* (EDS).

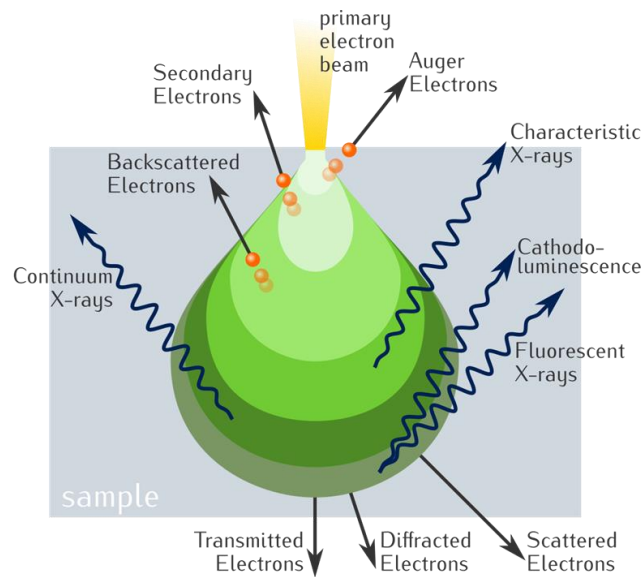


Fig. 19. Schematic drawing of a scanning electron beam incident on a solid sample, showing some of the signals generated that can be used to help characterize the microstructure [61].

Although SEM images could have a much higher resolution than optical ones, sometimes it is difficult to distinguish between two different phases present on a surface. To surpass this, the backscattered mode (BSE) can be used. As seen in Fig. 19, the backscattered electrons are electrons that come out of the sample and because they are moving so fast, they travel in straight lines. In order to form an image with BSE, a detector is placed in their path. This detector consists of a semiconductor material, typically silicon, placed directly above the sample. Electrons that hit the detectors excite the silicon electrons, creating an electron-hole pair. The free electrons and pairs generated from backscattered electrons can be separated before their recombination, generating a current. This current can be measured by an electronic circuit, which is eventually converted into a high-resolution image containing information about the elemental makeup of the sample. The quality of BSE images can be manipulated depending on the researcher's goals. When a higher acceleration voltage is used, for example, the penetration depth increases, making it harder to see thin film layers on the sample surface.

In this investigation, in order to be able to observe the fine microstructural details of the As Cast and heat-treated samples, SEM images were taken using two different equipment, both from the brand Thermo Scientific™, Waltham, MA, USA. One of them was the Helios™ G4 PFIB CXe DualBeam™ (Fig. 20) operating at an accelerating voltage of 5 kV and a 2.5 μ A Xenon Plasma FIB column. Also, Energy-dispersive X-ray spectroscopy (EDS) was carried out with this equipment, to evaluate the chemical composition of

the worn and unaffected surfaces. The other one was the FEI Helios NanoLab™ 600 DualBeam™ field emission scanning electron microscope (FE-SEM) (Fig. 21) operating at an accelerating voltage of 15 kV and a 1.4 nA Gallium + ion column. A magnification of 3500x was used for imaging and a high sensitivity backscattered electron detector was also used to obtain a better contrast between the phases, as Fig. 22 shows.

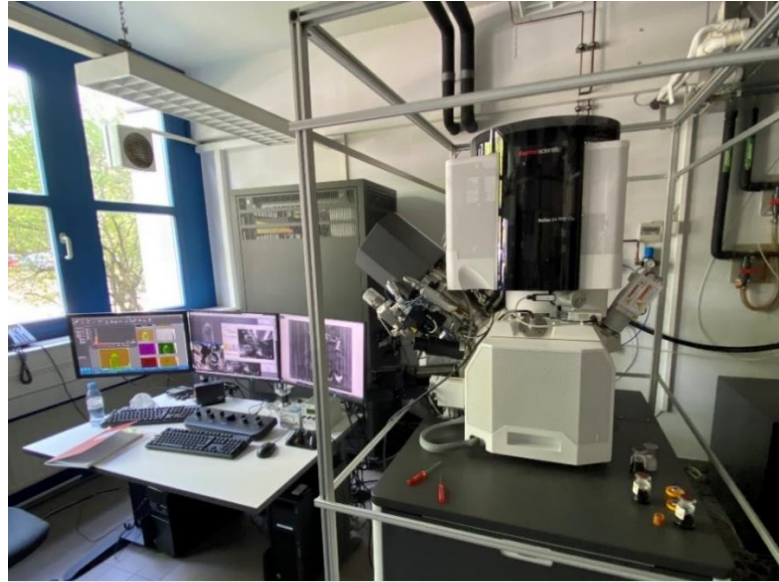


Fig. 20. Helios™ G4 PFIB CXe DualBeam™ SEM.



Fig. 21. FEI Helios NanoLab™ 600 DualBeam™ FE-SEM.

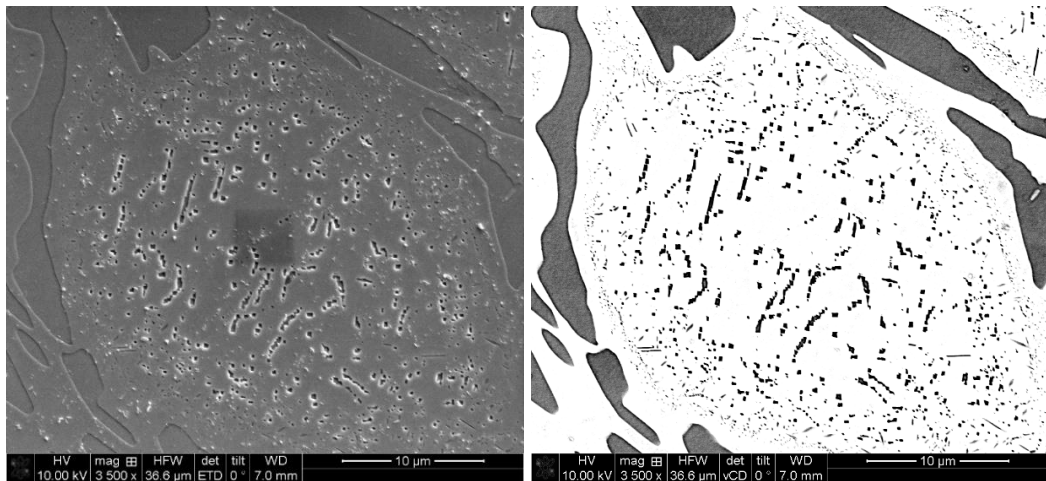


Fig. 22. Representative SEM micrograph of a heat-treated sample chemically etched with Murakami's reagent; (b) represents a 100% overlay of the corresponding micrograph in the back-scattered mode [62].

4.2. CONFOCAL LASER SCANNING MICROSCOPE (CLSM)

This microscope allows 3D topographic images to be obtained from the composition of several optical planes taken at different heights, as seen in the example in Fig. 23. High resolution is achieved by restricting the light reaching the detector, which should only come from the focal plane currently being measured, by using spatial filters to block light coming from outside the focused plane. A higher resolution is achieved the smaller the jump in the Z-axis between measured plane and measured plane, limited by the capacity of the movement and the minimum aperture of the objective.

In addition to the image, the microscope stores point-by-point information on relative distances, which makes it a useful instrument for making measurements in any direction with high levels of precision at both millimeter and nanometer scales, even allowing the roughness of the surface analyzed to be determined. To achieve the height measurement, an algorithm is used to determine the position on the Z-axis based on the received light intensity, with an accuracy of 1/100 of the focal plane separation value.

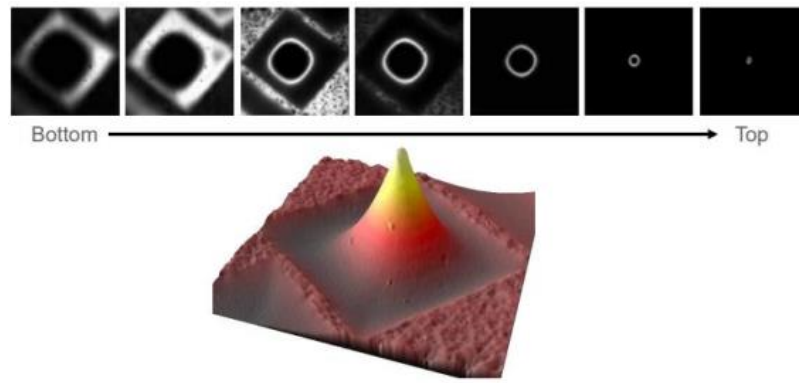


Fig. 23. Scan of a structure with a confocal laser scanning microscope. (Extracted from Leica Microsystems web, year 2008) [63].

The size of the measurement area is limited by the size of the light beam, which is reduced as more precision is required. To enlarge the observable field, the software can be programmed to measure several consecutive areas and then assemble them into a single image (stitching). This technique allows several millimeters of surface area to be scanned, even an entire sample, if it is smaller than the maximum displacement of the probe holder [64], [65].

In this work, a LEXT OLS 4100 Olympus CLSM confocal scanning microscope (Olympus Corporation, Tokyo, Japan) was used (Fig. 24) with magnifications from 5x to 100x. The CLSM uses a laser with 405 nm wavelength and, a lateral and vertical resolution of 120 and 10 nm, respectively. Surface roughness and wear track measurements of the Slip-on-track test were carried out with this microscope to obtain the scanned surface track profile data and further wear rate.

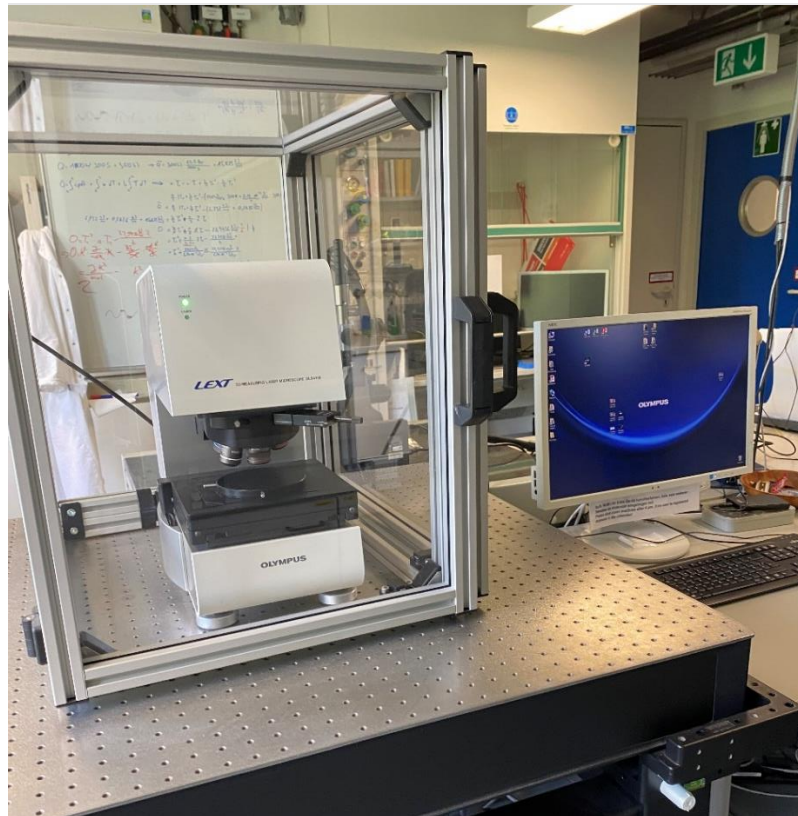


Fig. 24. LEXT OLS 4100 Olympus CLSM.

CHAP. 5: EXPERIMENTAL PROCEDURE

5.1. SAMPLES

The 16% Cr HCCI alloy used in this study was manufactured in an arc furnace and casted at 1450°C into rectangular (Y) shaped sand molds hardened with phenolic resin. An abrasive disc was used to cut the cast samples into pieces measuring 10mm × 10mm × 5mm approximately (Fig. 25). Arc spark optical emission spectroscopy (SPECTROMAXx, SPECTRO Analytical Instruments GmbH, Kleve, Germany) was used to determine the bulk chemical composition of the castings (Fig. 26).



Fig. 25. Rectangular sample before being mounted.



Fig. 26. SPECTROMAXx arc spark optical emission spectroscopy [55].

5.2. HEAT TREATMENT

Three different heat treatments were performed for this 16wt.% Cr HCCI on a box furnace brand Carbolite, which has a PID controller that commands the process (Fig. 27). The three HTs consisted of heating, with a 10°C/min rate, up to 800, 900, and 980°C, respectively. Once the desired temperature is reached, they were instantly cooled in water with a ratio of 40°C/min approximately.

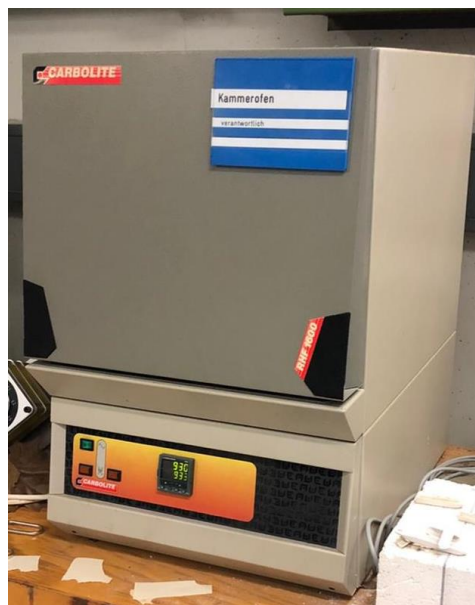


Fig. 27. Furnace used for realizing the Heat Treatments.

Therefore, four groups of two samples each were formed:

- As Cast: I and II
- 800°C: I and II
- 900°C: I and II
- 980°C: I and II

Group I was designated for microstructure analysis and group II for wear tests.

The schematic of the heat treatment cycle is represented in Fig. 28.

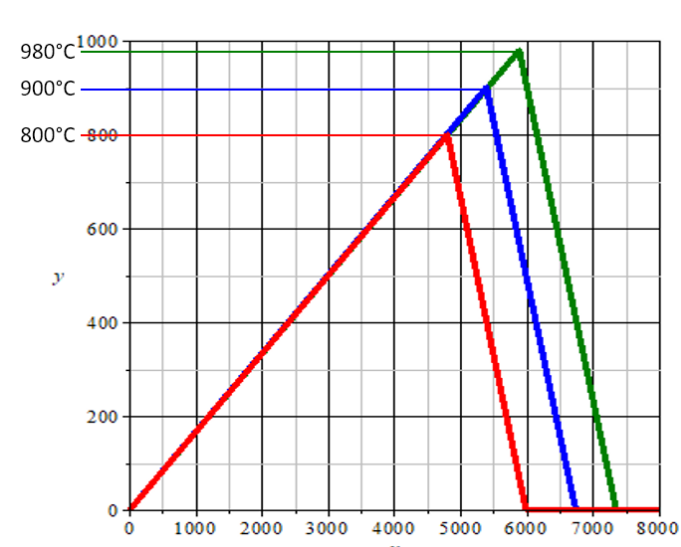


Fig. 28. Schematic of the performed heat treatment.

5.3. METALLOGRAPHIC PREPARATION

Once heat treated, all samples were embedded on resin with a metallographic mounting machine Mecapress I (Fig. 29). The embedded samples were subjected to grinding and polishing according to the specifics mentioned in Table 2. to obtain a scratch-free, mirror surface. A Struers TegraPol-21 grinder/polisher (Struers Inc., Cleveland, OH, USA) was used for this purpose (Fig. 30).

Grinding/Polishing Pads	Grain Size	Time (minutes)
SiC grit paper	P80 - P180 - P320	2-3
	P600	5
	P1200	8
MD Dac	6 μ diamond suspension	10
MD Mol	3 μ diamond suspension	6
MD Nap	1 μ diamond suspension	5
MD Chem	0.04 μ oxide polishing suspension (OPS)	2 (OPS) + 5 (water)

Table 2. Grinding/Polishing parameters.

It should be noted that after each grinding and polishing step, the samples were washed with water and cotton pads, rinsed with ethanol, and dried with pressurized air. In addition, before proceeding to the next step, the samples were lightly wetted with water to ensure that they were lubricated enough to withstand the initial jolt of grinding.



Fig. 29. Mecapress I metallographic mounting machine.



Fig. 30. Struers TegraPol-21 grinder/polisher.

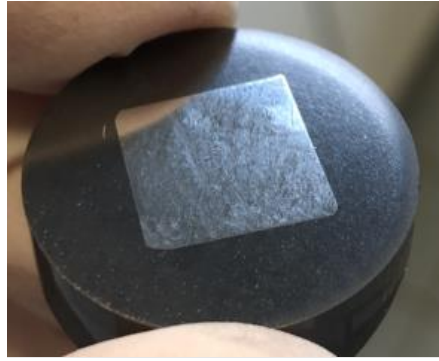


Fig. 31. Piece of 16% HCl after HT after mounting.

5.4. ETCHING

As mentioned above, samples from group I were destined for microstructural analysis. Therefore, once polished they were etched with two different reagents depending upon the intended purpose as detailed in Table 3. These parameters were determined according to the previous work of Guitar and Nayak [66], [67]. In all cases, the samples were immersed in the freshly prepared etchant for the appropriate time (Fig. 32), rinsed with water and ethanol, and air-dried. Finally, the etched samples were ultrasonicated in isopropanol for 5 minutes before air-drying.

Sol. N°	Etchant	Composition	Etching Parameters		Purpose/Objective
			Temperature	Time	
1	Villella's Reagent	100 mL Ethanol + 5 mL HCl + 1 g Picric Acid	Room Temperature (RT)	7s	General Microstructure Observation
2	Modified Murakami's reagent (MM)	4 g potassium ferricyanide + 8 g Sodium hydroxide + 100 mL water	RT	15s*	IA - Carbide Quantification

Table 3. Description of the two etchants employed on the polished samples and their corresponding parameters, depending on the final objective.

*In the 800°C sample it was necessary to etch for 20+10 seconds in order to reveal the secondary carbides.



Fig. 32. Cupboard used for etching the samples.

5.5. IMAGE ANALYSIS (I-A)

The analysis of the SEM images was performed using the software ImageJ2 with the FIJI processing package (version 1.52p) (LOCI, UW-Madison, WI, USA) [68]. Despite the vast field of image analysis, microstructural segmentation and quantitative image analysis were performed on this project, using some of the procedures mentioned in [62]. It is worth noting that the analyzed area for all images was kept constant, $51.2 \times 44.2 \mu\text{m}$, and 7 micrographs were taken for each sample. Furthermore, a magnification of 2500x was used to include more than 3000 particles in each image. Due to the presence of more than two phases in the sample, it was required to use the trainable WEKA (Waikato Environment for Knowledge Analysis) segmentation approach. This is an inbuilt FIJI plugin that combines a collection of machine learning algorithms with a set of selected image features to produce pixel-based segmentation [14], [32]. The initial process involves,

‘training’ the classifier with a set number of classes (different phases) and further continuing by adding more data to make the training robust and finally saving the classifier. The ‘saved’ classifier is then applied to another set of micrographs to obtain the respective segmented result. As Fig. 33(a). shows, austenite, martensite, eutectic, and secondary carbides are present in the studied samples. Therefore, in order to be able to quantify and characterize the secondary carbides, the image was segmented into two different groups, the secondary carbides, and the rest (austenite, martensite, and EC), as Fig. 33(b) shows in color white and black, respectively.

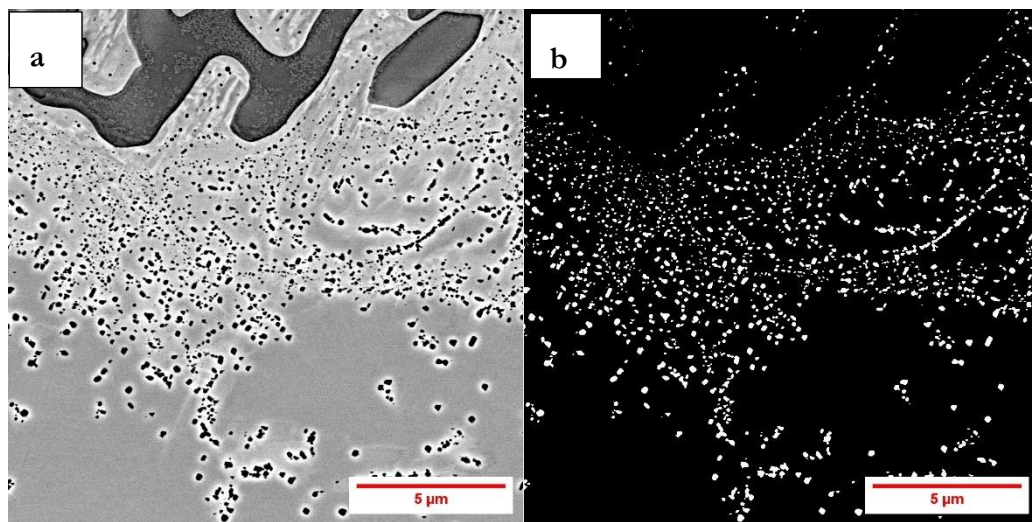


Fig. 33. SEM vCD image of 900°C sample before (a) and after (b) the segmentation using the Trainable WEKA segmentation method.

Considering the magnification and resolution of image acquisition, all pixelated particles having a diameter of less than 100 nm were excluded from the analysis. Further details concerning the determination of the SC specifics are given in [62].

Also, the nearest neighbor distance (nnd) parameter was used. It was determined with the Fiji software and using a plugin developed for that purpose [69]. The nnd was calculated using the data from BSE + IA images. The nnd is calculated by the Fiji [69] software as the distance between the centroids of a particle and the centroid of the nearest particle. Note that the result can be biased if the size and shapes of the particles are very irregular. All the particles cutting the edges of the image were not considered for the analysis.

5.6. HARDNESS MEASUREMENT

Microhardness was measured using a Struers Dura Scan 50 microhardness tester (Struers Inc., Cleveland, OH, USA) with a load of 0.09807 N ($HV_{0.01}$). During the testing, the dwell time was 15 s and an average of 10 measurements were considered. The load was chosen considering previous works of Nayak et al. [57], such that the surrounding entities are not participating in the evaluation of the matrix hardness and the indentation mark was clearly resolvable using the optical microscope.



Fig. 34. Struers Dura Scan 50 microhardness tester [70].

5.7. TRIBOLOGICAL TESTS

Dry sliding wear tests in a linear back-and-forth motion were carried out using a slip-on-track micro tribometer (CSM Instruments), while the entire assembly was placed in a Spirale 3 - Excal 2211-HA (Climats, Saint Médard d'Eyrans, France) environmental chamber to control temperature and humidity (Fig. 35). Alumina (Al_2O_3) 3 mm balls (99.00%-99.99% purity; Grade GD28) were used as the sliding body. It should be noted that, before starting the wear tests, the balls were rinsed in an ultrasonic bath for 10 minutes each with isopropanol and ethanol separately. The value of the critical load (PC) i.e., the load

at which the outset of plastic deformation takes place in the austenitic matrix, was determined by Nayak et al. [57]. Based on that, the load applied in this work was higher than the calculated P_c . Tab. 4 resumes the parameters used on the tribological tests.

Parameter	Value
Temperature [°C]	22-26
Relative Humidity [%]	40-50
Load [N]	20
Sliding velocity [m/s]	0.02
Stroke length [mm]	5.5
N° of cycles	2000
Data acquisition frequency [Hz]	50

Table 4. . Tribological testing parameters.

Wear was quantified in terms of wear rate, and the volume loss in each track was calculated using the LEXT software, considering the entire wear track, including the ends, and Equation 3 was used to calculate it. Similar variations of Eq. 3 were used in other studies to quantify wear, where mass loss and density were considered [71]–[73]. In Eq. (3), V represents the wear volume (mm^3), l is the total sliding distance ($5.5 \times 2 \times 2,000$ mm), P is the applied load (N), and K represents the wear rate ($\text{mm}^3/(\text{N}\cdot\text{mm})$).

$$K = \frac{V}{l \times P} \quad (3)$$

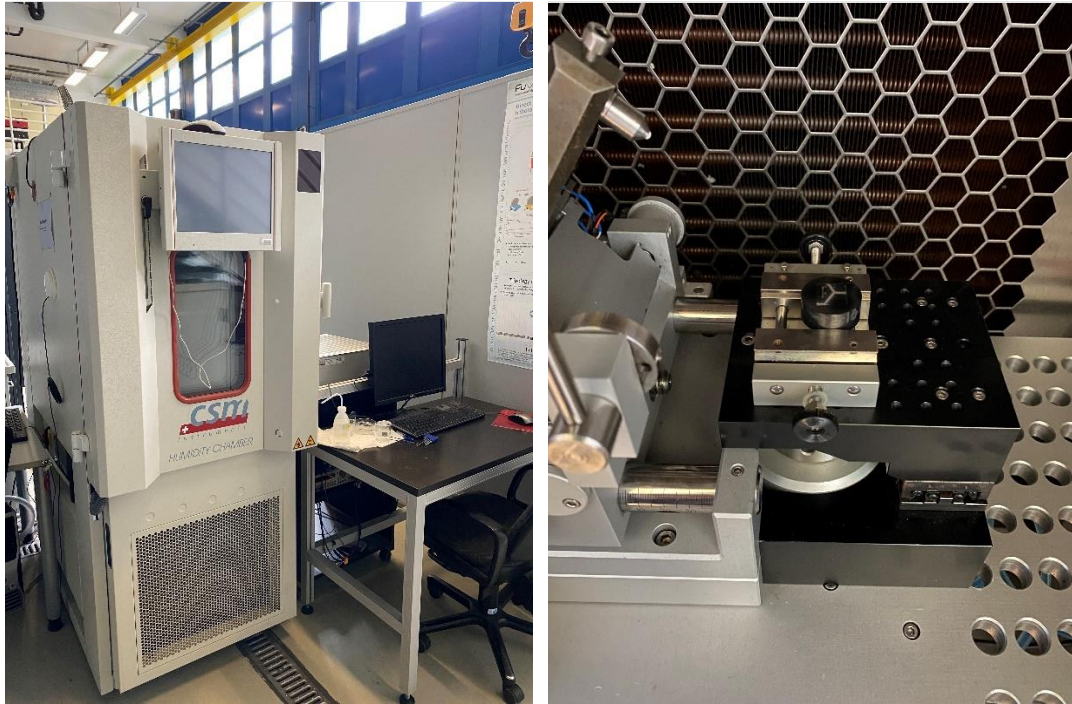


Fig. 35. Spirale 3 - Excal 2211-HA Environmental chamber and Microtribometer used, respectively

CHAP. 6: RESULTS AND DISCUSSIONS

In this chapter, the results obtained during all the tests and analyses will be presented and discussed. In the first instance, we will focus on the results concerning the general microstructure of each condition. Then, the distribution of secondary carbides will be evaluated, followed by the results of the wear behavior through the analysis of the tribological tests performed.

6.1. PHASE AND MICROSTRUCTURAL EVOLUTION

The chemical composition of the studied HCCI is presented in Table 5.

Alloy	C	Fe	Cr	Mn	Mo	Ni	Cr/C
16% HCCI	1.92	81.5	14.38	0.41	0.71	0.17	7.5

Table 5. Bulk chemical composition (in wt. %) of the samples was measured by optical emission spectroscopy.

As mentioned in Section 5.1, Vilella's reagent was used to characterize the microstructure of the four samples, followed by Optical and SEM electron microscopy at different magnifications. Fig. 36(a) shows SEM images of the untreated sample in vCD mode. The As Cast microstructure is characterized by the presence of Cr-rich M_7C_3 type intergranular eutectic carbides (EC) ($\sim 30\%$) dispersed in an austenitic matrix (γ) ($\sim 60\%$), and a thin layer of needle-like martensite (α') ($\sim 10\%$) sandwiched between the EC and γ , as indicated in Fig. 36. The phases present in the microstructures are color-arrow coded throughout the work according to the following terminology:

- Austenite (γ): Red arrow pointing downwards
- Martensite (α'): Green arrow pointing upwards
- M_7C_3 eutectic carbide (EC): Yellow arrow pointing right
- M_7C_3 secondary carbide (SC): Blue arrow pointing left

The presence of martensite can be explained as a consequence of the formation of eutectic carbides, which resulted in the depletion of carbide-forming elements such as Cr and C in the surrounding matrix, increasing locally the Ms temperature. On the other hand, a high Cr/C ratio, and faster cooling rates during casting all favor austenitic matrix structures [18]. According to the graph presented by Maratray et al. [74], where the Cr/C ratio and Mo content are related to austenite decomposition during cooling, a Cr/C ratio greater than 6.2 is required for an alloy with a Mo content of around 0.7 wt. percent to avoid austenite decomposition. Even though this HCCI has a Cr/C ratio of 7.5, there are some small areas where austenite has partially transformed into pearlite, as shown in the magnified region of Fig. 36(b). It is worth mentioning that no SC was seen on this sample. As expected, no secondary carbides were observed. This is because the As Cast microstructure is the starting point for the subsequent austenitic destabilization heat treatment which leads to SC precipitation within the matrix [16], [38].

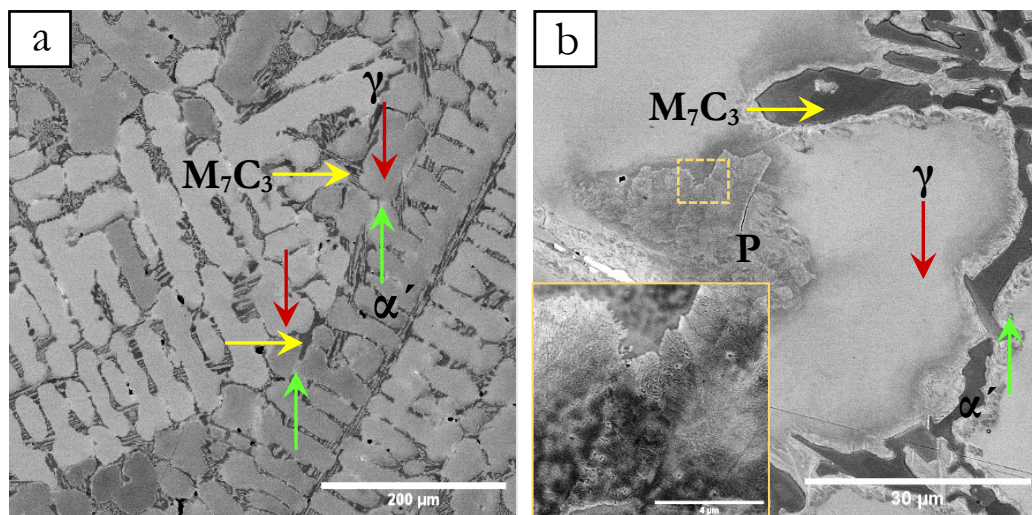


Fig. 36. Representative SEM micrographs of As Cast sample, after Vilella's etching for 15 seconds. (a) Shows the eutectic carbides between the austenite dendrites. (b) The different phases, austenite (γ), martensite (α'), pearlite (P), and eutectic carbides (M_7C_3) are indicated in the image (b). The pearlite phase can be observed in the inset in (b). The various phases are marked for reference.

Fig. 37 shows the optical micrographs of the three heat treated samples, together with the as-cast one for comparison, after etching with Vilella's reagent. The dark regions in the optical images of Fig. 37 correspond to areas where SC precipitation and austenite to martensite transformation took place. This transformation occurs surrounding the eutectic carbides (red arrows) and in certain areas inside the austenite dendrites, due to the high

concentration of small secondary carbides. When compared to the As-Cast state, image (b) demonstrates the beginning of the precipitation of small secondary carbides (yellow arrows) at 800°C as well as the presence of a fine martensitic matrix around the unaltered eutectic carbide phase. With the increasing temperature, this SC seems to increase in number. On the 900°C sample, the austenitic matrix is partially transformed into martensite, as well as the SC nucleation zones. At 980°C, these zones between the eutectic are almost completely composed of secondary carbides and martensite, with a few spots of austenite left. These materials are predicted to contain small secondary carbides, but optical microscopy methods cannot resolve them. Therefore, SEM pictures were taken to provide a higher level of resolution and detail concerning the existence and distribution of secondary carbides. As a result, provides a much clearer understanding of these transformations on the HCCI by providing three different SEM pictures at various magnifications for each sample.

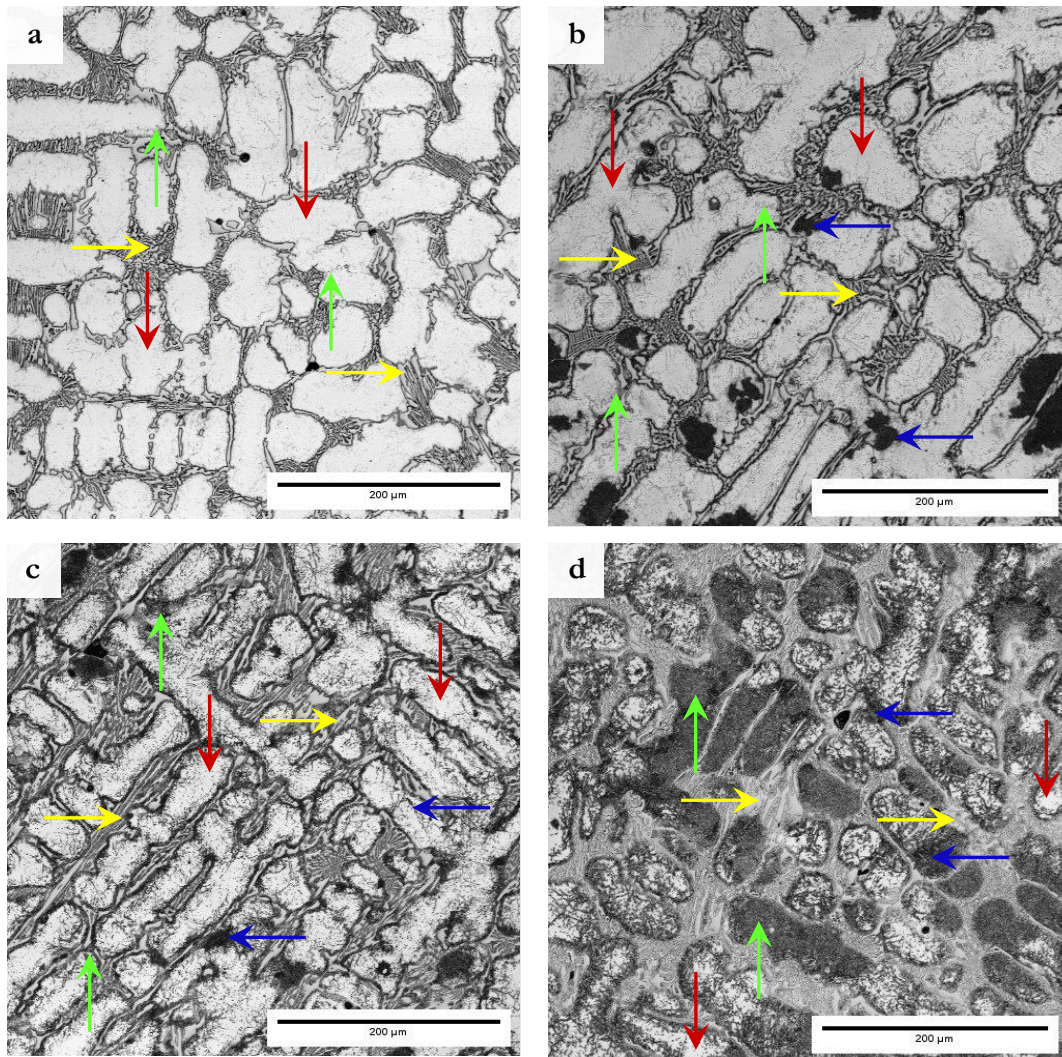


Fig. 37. Optical microscopy images showing: (a) the as-cast condition; (b) the 800°C condition; (c) the 900°C condition; and (d) the 980°C condition. The samples were etched with Vilella's reagent for matrix/carbide contrast. The phases are accordingly colour and arrow labelled for reference.

It is worth mentioning that the selection of the image magnification is non-trivial for an appropriate characterization of the carbides. At low magnification, the secondary carbides are not well distinguished and at higher magnifications, no eutectic carbides fit completely within the image, as shown in Fig. 38. For this reason, and due to the difference in size between eutectic and secondary carbides, they cannot be analyzed simultaneously from the same image. The focus of this work is to evaluate and characterize the secondary carbides precipitated during the thermal treatment.

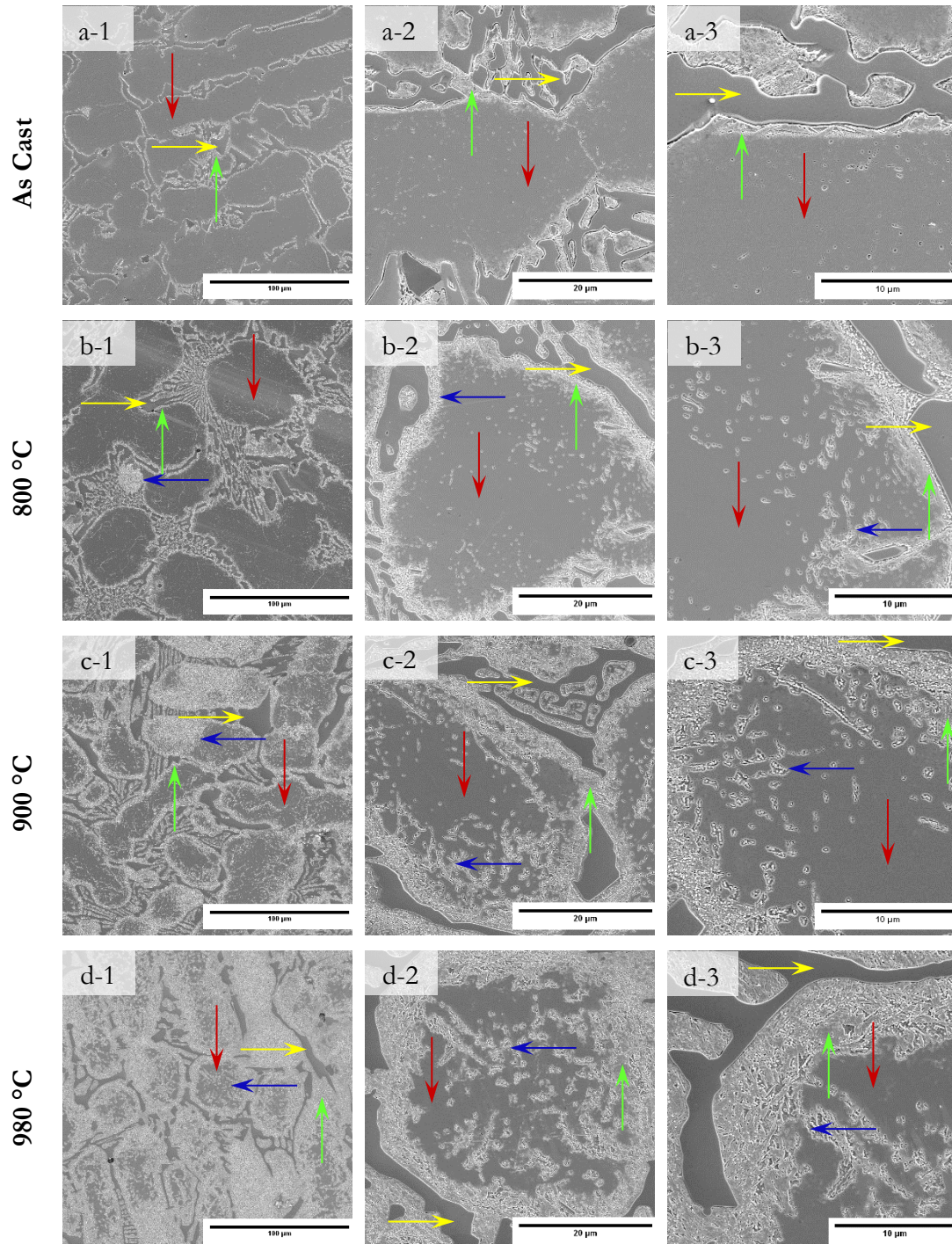


Fig. 38. SEM (BSE) images for all the samples at different magnifications from left to right x 500, x 2000, and x 3500, respectively. (a) As cast, (b) 800 °C, (c) 900 °C Q, and (d) 980 °C. The phases are accordingly colour and arrow labelled for reference.

As seen in Fig. 37(b) and Fig. 38(b1-b3), the presence of SC can be observed after heating up to 800 °C, which is a clear indication that the SC precipitation occurs during heating, starting at temperatures below 800 °C. The precipitation of SC started in the regions next to the EC, where a thin layer of martensite was present in the as-cast state. This is probably a consequence of the high-density of non-equilibrium defects present in the martensitic phase [75]. The number of SC increases as the HT temperature rises, and they precipitate towards the matrix center, as observed in the 900°C and 980°C samples (Fig. 38(c) and (d)). There, large nucleation regions are present, as well as a larger fraction of austenitic matrix into martensite.

As learned from previous works [16], [25], [33], [76], the increase in the temperature leads to the increase of the nucleation zones for secondary carbides, and the transformation of the matrix from austenite to martensite. This can be appreciated by looking at the increasing white zones in the 800, 900, and 980 °C images, respectively.

6.2. SECONDARY CARBIDES CHARACTERIZATION

Previous works from Guitar et al [16], [77] showed the presence of M_7C_3 SC after heat treatment of 16%Cr HCCI, presenting a rounded morphology. Despite the chemical composition of the material treated/used in this work partially differs from the treated by Guitar et al. [77], the Cr/C ratio is close enough to expect the same type of carbides. Fig. 39 shows three SEM images of the 800, 900, and 980°C samples, respectively, attacked with Vilella reagent.

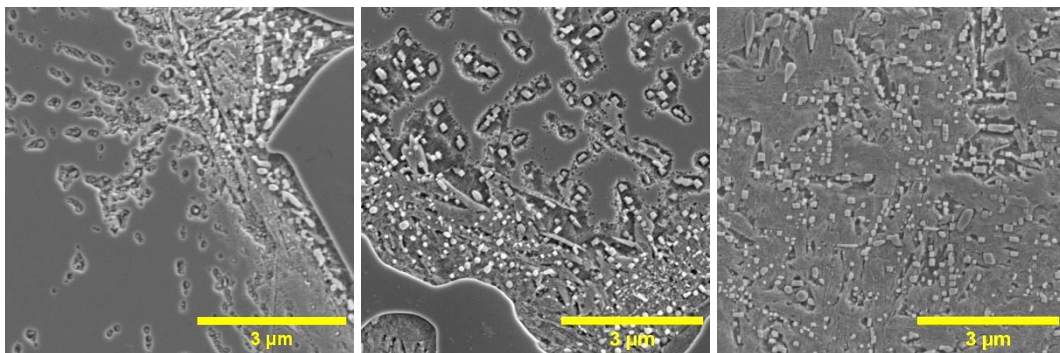


Fig. 39. SEM images showing the morphology of the secondary carbide particles in 800,900 and 980°C respectively.

Although the secondary carbides in Fig. 39 are observed at magnifications higher than x2000, since they are etched with Vilella's reagent, due to the low contrast between the phases present, is not possible to perform a correct image segmentation with the software used for a further particle's quantification. Therefore, they were treated with the modified Murakami reagent, which allows having a better contrast between the SC and the matrix in the SEM (particularly with the BSE detector, Fig. 40), allowing to do IA and segmentation process simpler.

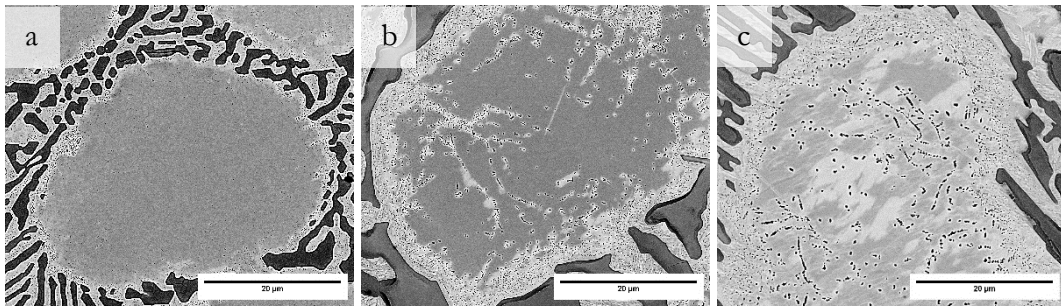


Fig. 40. SEM BSE mode images after etching with Modified Murakami (a) 800 °C, (b) 900 °C Q, and (c) 980 °C.

Figure 42 depicts the size distribution in μm^2 of the secondary carbides for each of the samples. The lognormal distribution is the best fit for the values for the type of sampling. Although all treatment conditions have a high number of particles between 0.0003 and 0.014 μm^2 , resulting in a skewed distribution to the right, the number of particles decreases as the treatment temperature increases.

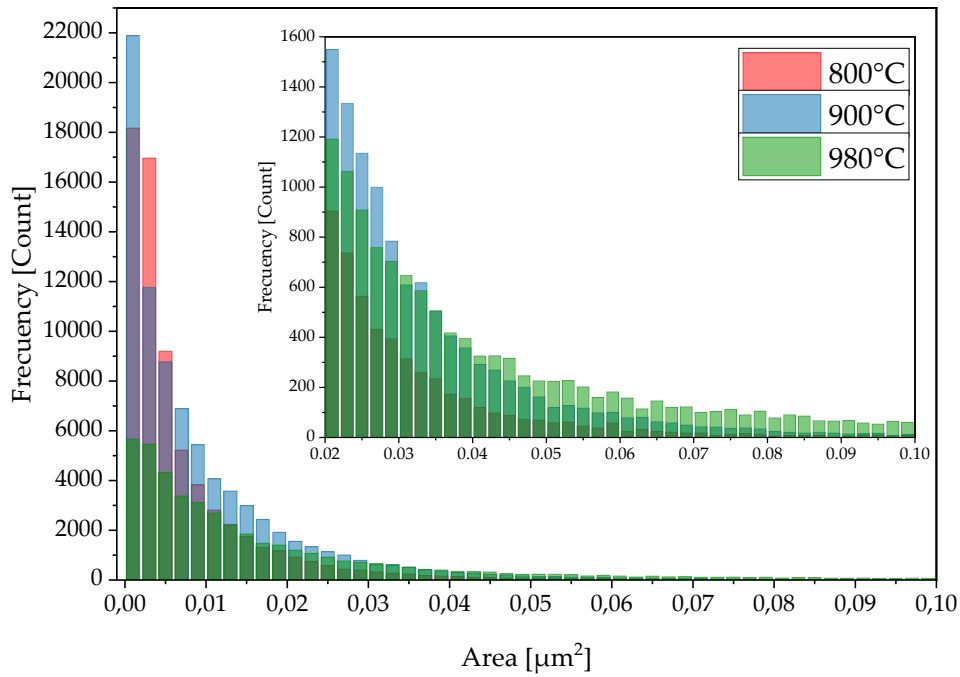


Fig. 41. Particle size distribution for 800, 900, and 980°C, respectively.

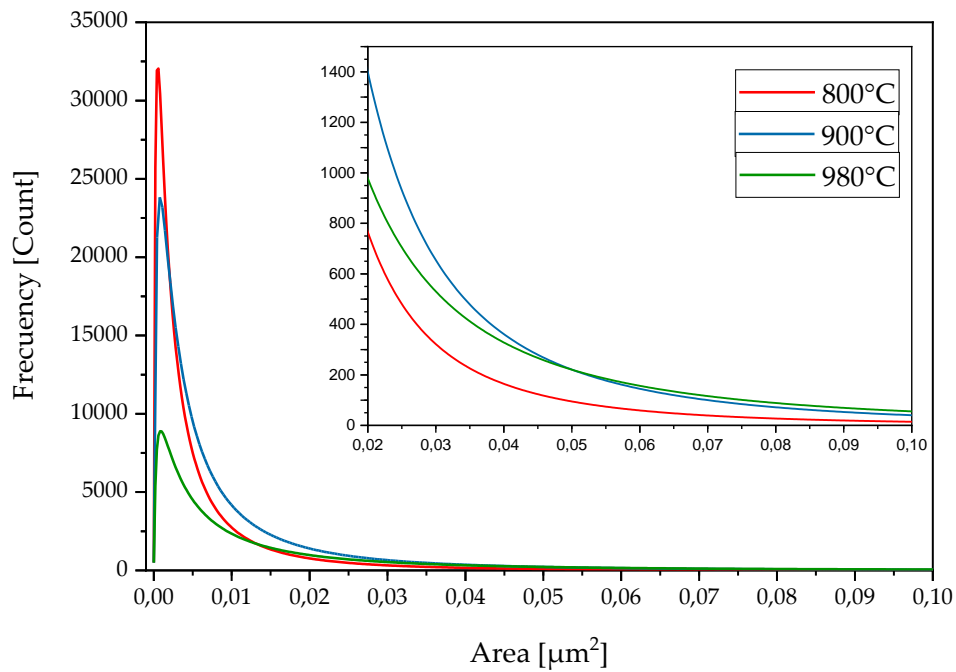


Fig. 42. Lognormal curves of the particle size distribution.

Sample	Mean \pm SD [μm^2]
800°C	0.00672 \pm 0.00988
900°C	0.01018 \pm 0.01302
980°C	0.0189 \pm 0.02934

Table 6. SC mean size.

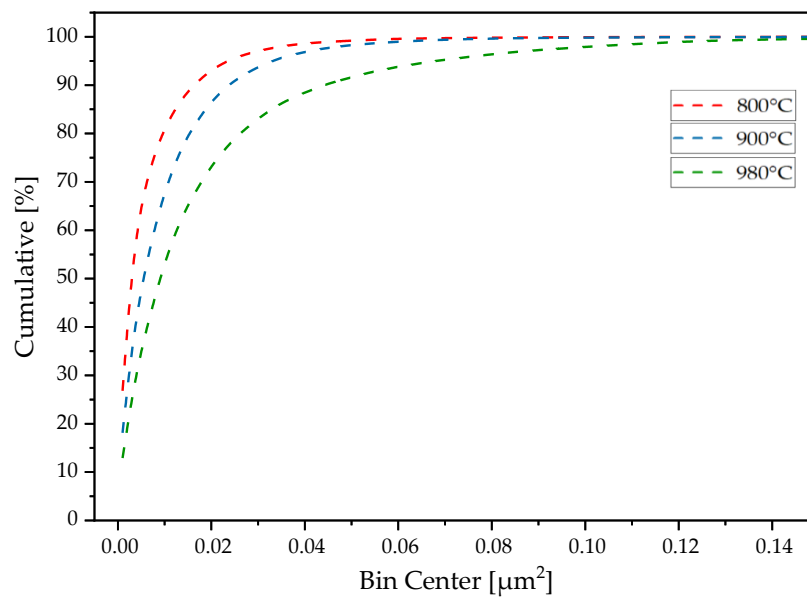


Fig. 43. SC particle size cumulative distribution curve.

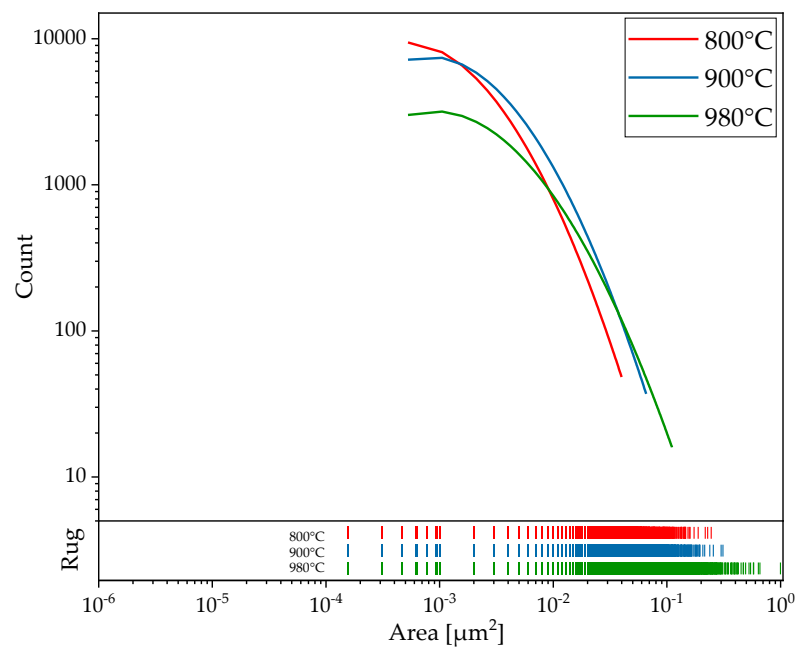


Fig. 44. distribution-rug plot plotted on a log-log scale, which is indicative of a histogram with zero-width bins and used to visualise the distribution of the data.

The log-normal size distribution (in terms of particle count vs. area (μm^2)) for the three HTed samples is graphically represented in Fig. 42. The average particle size for the corresponding samples is indicated in the inset Table 6. The cumulative distribution curve is plotted in Fig. 43, which shows that for a given size, the percentage of particles falling within that size range decreases from 800°C to 980°C. This is further exemplified by the distribution-rug plot in Fig. 44, plotted on a logarithmic scale for better visualization, where it is indicated that the 980°C sample has a higher number of particles with larger sizes. Analogously, the 800°C sample has the highest number of smaller particles. Combining the information obtained from Fig. 41, Fig. 42, Fig. 43, and Fig. 44, it is evident that the average size increases from 800°C to 980°C.

The lognormal particle distribution for each condition was analyzed using GeoGebra software to determine the probability of finding particles larger than $0.05 \mu\text{m}^2$, resulting in Table 7.

Sample	800°C	900°C	980°C
Probability	36.0%	49,8%	62.4%

Table 7. Probability of founding a particle with an area more than $0.05 \mu\text{m}^2$.

Fig. 45 represents the area fraction occupied by the secondary carbides in each of the samples. It can be seen that the SCVF was similar in the 900 and 980°C samples (4.48 ± 0.59 and 4.54 ± 1.53 , respectively), however, there is a significant difference between the latter and the 800°C condition (2.85 ± 0.59). Even though, as previously stated, the analysis is dependent on the area where the image was taken, there are areas of small carbides and areas of large carbides in the 980°C sample. If the maximum value of the SCVF for each sample is taken, it is possible to assume that temperature influences the volume fraction of the secondary carbides, which increases with increasing temperature. Figures 42 and 43 show that increasing the temperature, up to 980°C in this case, results in a distribution of larger secondary carbides throughout the matrix, as reported by Guitar et al. in [16], [38].

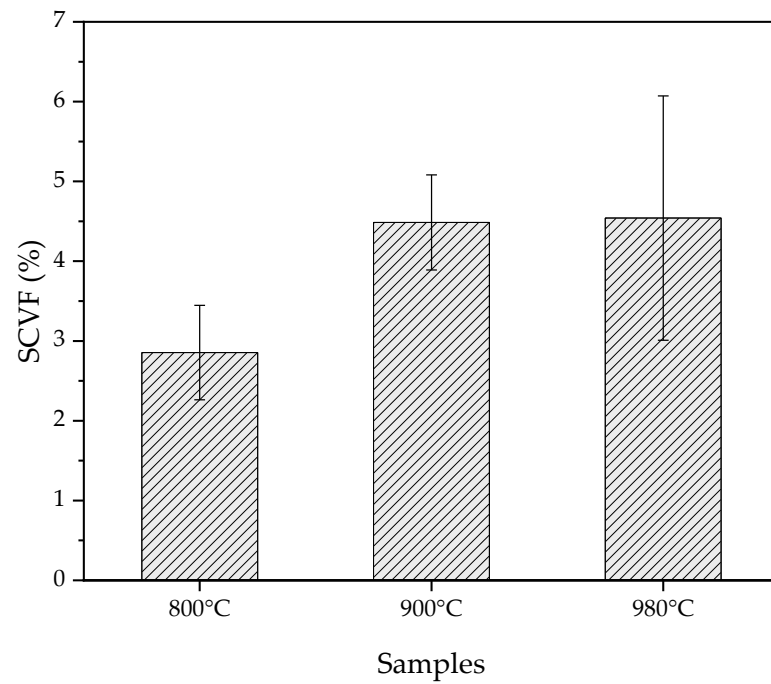


Fig. 45. Secondary Carbide volume fraction.

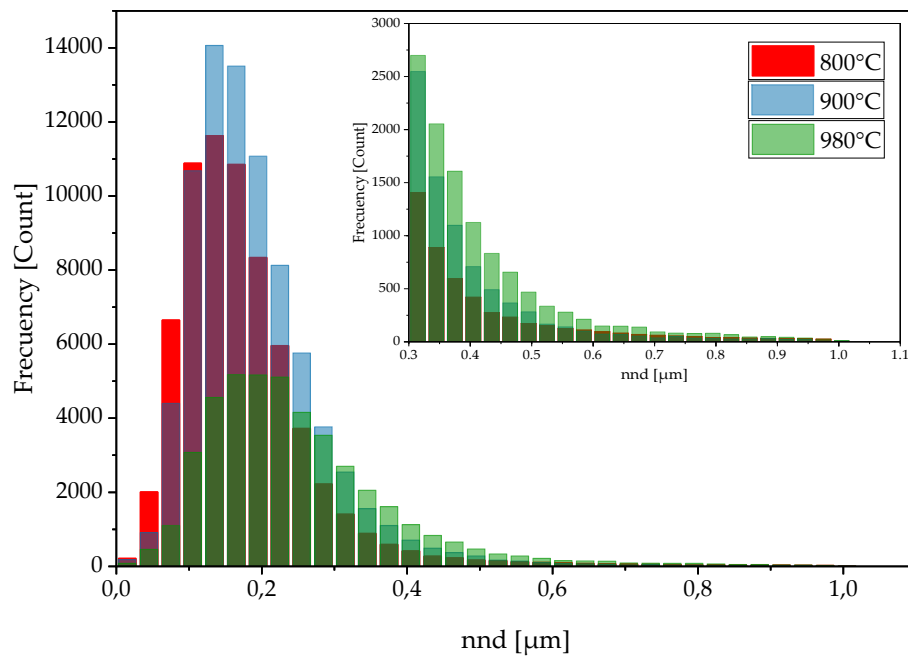


Fig. 46. Nearest Neighbor Distance distribution for the samples 800, 900, and 980°C.

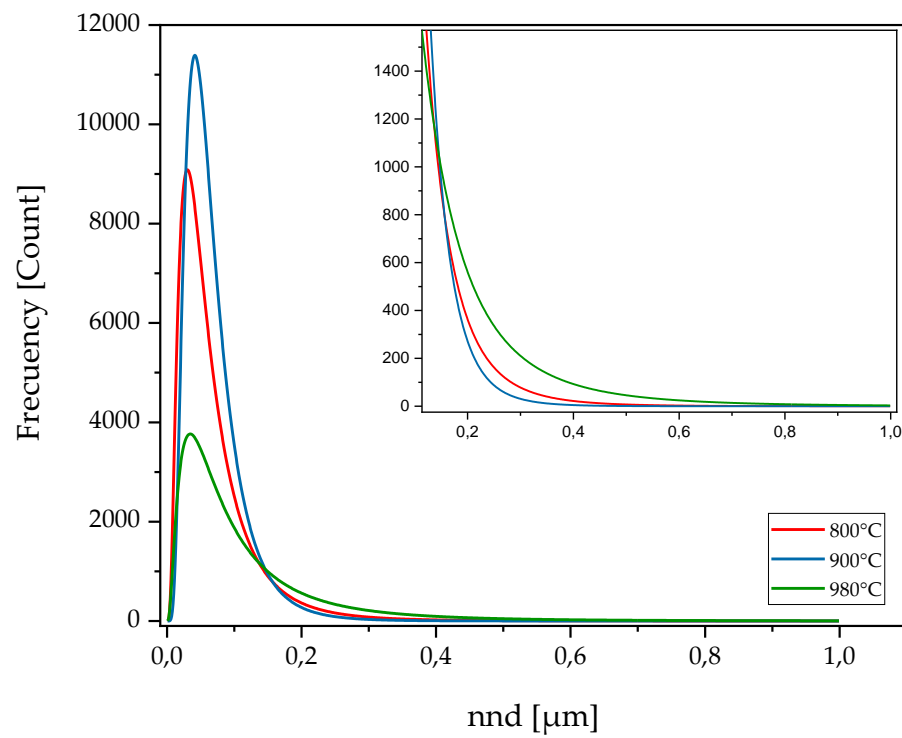


Fig. 47. Lognormal distribution of the Nearest Neighbor Distance for the samples 800, 900, and 980°C.

Sample	Nnd: Mean \pm SD [μm^2]
800°C	0.179 ± 0.125
900°C	0.192 ± 0.109
980°C	0.257 ± 0.172

Table 8. nnd mean size.

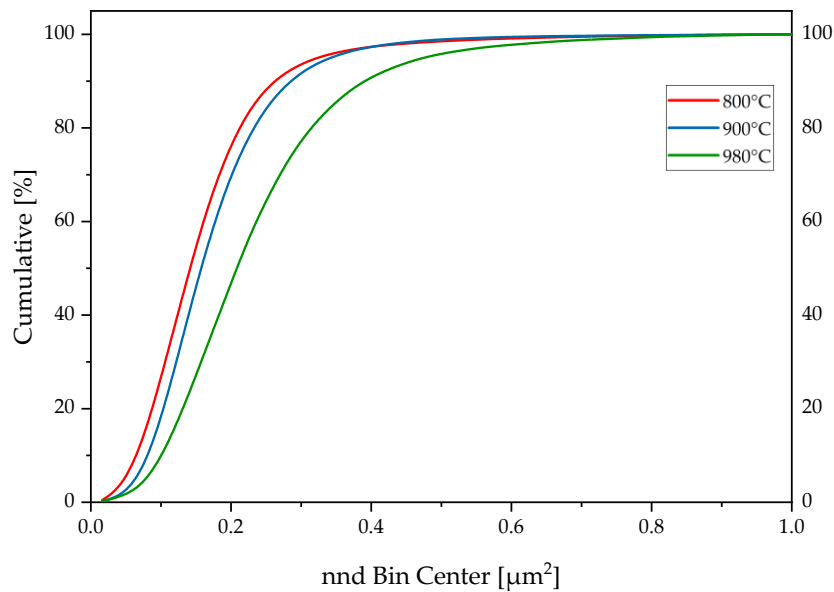


Fig. 48. SC particle nnd cumulative distribution curve.

The distance between neighbors is regarded as an important descriptive parameter for quantifying the degree of particle distribution because it can affect the mechanical response of the material. Fig. 46 depicts the nnd distribution, in terms of particle count vs. nnd (μm), for the three HTed samples. As for the particle size, the distribution of the nnd is a log-normal distribution, whose representative curves can be seen in Fig. 47. The average particle size for the corresponding samples is indicated in Table 8. The cumulative distribution curve is plotted in Fig. 48, which shows that for a given size, the percentage of nnd particles falling within that size range decreases from 800°C to 980°C. It should be noted that, although nnd in the lower temperature samples is lower, the carbides are concentrated at the periphery of the austenite dendrites. Whereas, with increasing treatment temperature, the carbides are more evenly distributed within the matrix.

6.3. MICROHARDNESS

As stated in the experimental section, the indentations were performed with a load of 0.098 N ($\text{HV}_{0.01}$), in order to measure the matrix while minimizing the influence of carbides and taking into account that a plastic deformation zone is generated around the

imprint during the measurement. As shown in Figure 48, the presence of eutectic carbides indicates a slightly higher hardness, as indicated by a smaller size (yellow circle) of the imprint for the same load as the rest of the imprints. On the contrary, a larger imprint size can be seen in the austenitic zone, as indicated by the red circle, and an intermediate imprint size can be seen in the martensitic zone, as indicated by the blue circle, as expected for each of the phases present in the microstructure, as reported by [14], [54].

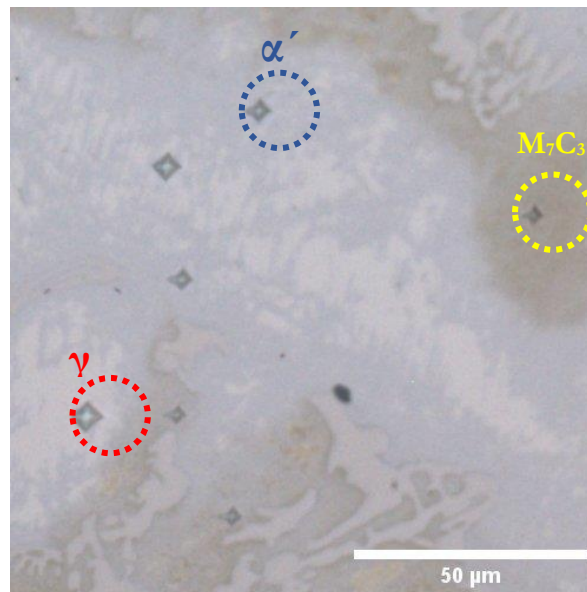


Fig. 49. Optical micrograph of the microhardness indentations on the 980°C sample.

Fig. 49 depicts the imprints made on each of the samples as a comparison of their size and microstructure change. It is to be expected that the average value measured in the higher temperature samples will have a higher degree of deviation due to the presence of secondary carbides and the transformation from austenite to martensite in certain areas.

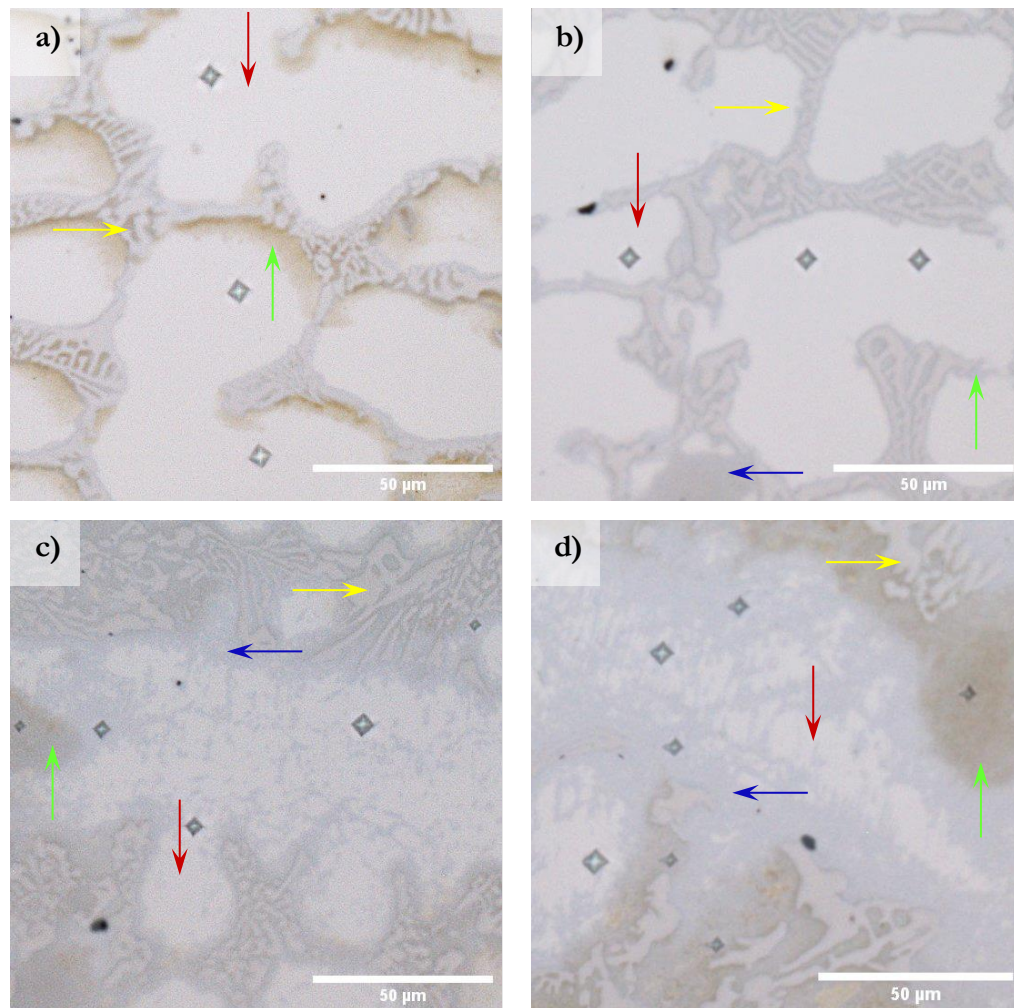


Fig. 50. Optical micrograph of microhardness indentations: a) As Cast; b) 800°C; c) 900°C; and d) 980°C. The phases are accordingly colour and arrow labelled for reference. Austenite (γ): Red arrow pointing downwards, Martensite (α'): Green arrow pointing upwards, M_7C_3 eutectic carbide (EC): Yellow arrow pointing right, and M_7C_3 secondary carbide (SC): Blue arrow pointing left.

Fig. 50 represents the Vickers microhardness values of the microstructures of the studied samples. The higher temperature samples' increased hardness is due to the greater presence of secondary carbides scattered throughout the matrix (increased CVF). The 900°C sample, however, does not have a significant increase in hardness when compared to the As Cast and 800°C samples, nor does the 980°C sample. The increase in hardness of the latter, on the other hand, is attributed not only to an increase in CVF but also to the transformation of the austenitic matrix into martensitic.

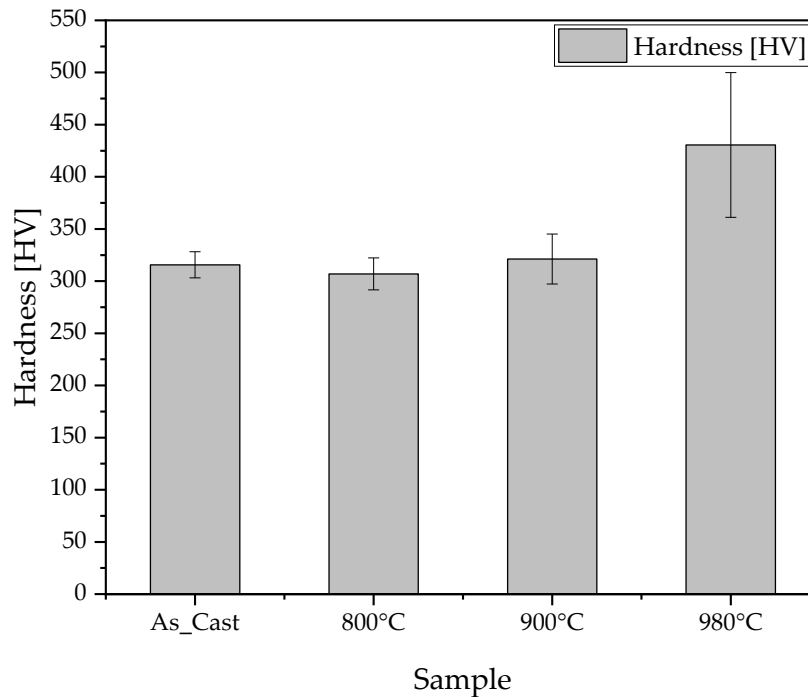


Fig. 51. Microhardness measurements for four microstructural states: as cast, 800, 900, and 980°C, respectively. The standard deviation of the measures is also plotted.

The presence of more secondary carbides scattered throughout the matrix increases the hardness of the microstructure as CVF increases. However, the 900°C sample does not have a significant increase in this property when compared to the As Cast and 800°C samples, as the 980°C sample does. The increase in hardness in the 980°C sample, on the other hand, is attributed to an increase in CVF and the transformation of the austenitic matrix to martensitic.

6.4. WEAR

Figures 51(a)-(d) show CLSM micrographs of the sample surface after wear with a 50% overlap of the height profile for each condition studied. To improve visibility across the wear track, the "composite" CLSM micrograph was divided into two halves based on height (left half) and intensity (right half). For reference, the height range (applicable only to the height profile) and sliding direction (SD) are also mentioned. The variation in height

from the edge of the wear track to the center is clearly visible, as indicated by the change in blue shade.

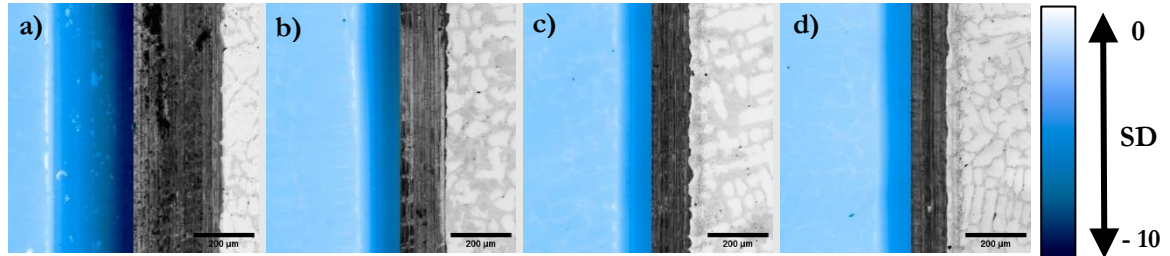


Fig. 52. CLSM micrographs of the wear tracks at (a) 800°C, (b) 900°C, and (c) 980°C with a 50% overlap of the height profile. The CLSM micrograph on the left, in blue tones, is based on height, and the one on the right, in grey tones, on intensity. The height range (only applicable to the height profile) and sliding direction (SD) are also mentioned.

The wear track of the untreated sample is significantly wider and deeper than that of the heat-treated samples, as shown in Fig. 52. As shown in Table 9, there is a decrease in these dimensions as the heat treatment temperature increases, with the reduction in depth being 40, 47, and 59 percent, respectively, in comparison to the untreated sample. Fig. 53, which depicts the average depth profile of the three tests for each condition taken transverse to the sliding direction, confirms this. Furthermore, Fig. 54 clearly shows the decrease in wear track size with increasing temperature.

Samples	800°C	900°C	980°C
Depth reduction	40%	47%	59%
Width reduction	50%	55%	58%

Table 9. Depth and Width reduction percentages concerning the As Cast condition.

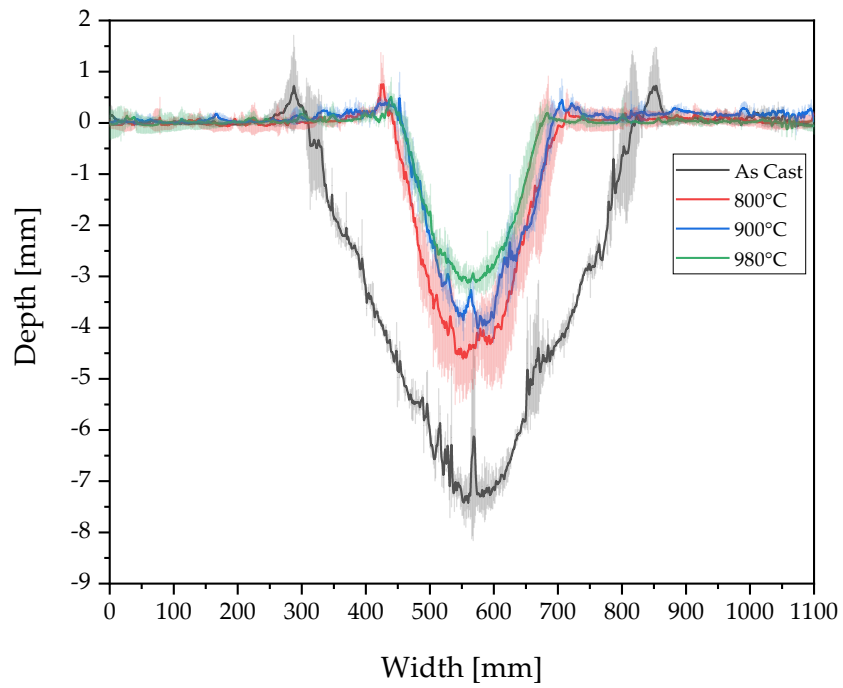


Fig. 53. Wear tracks profile comparison between As Cast, 800, 900, and 980°C.

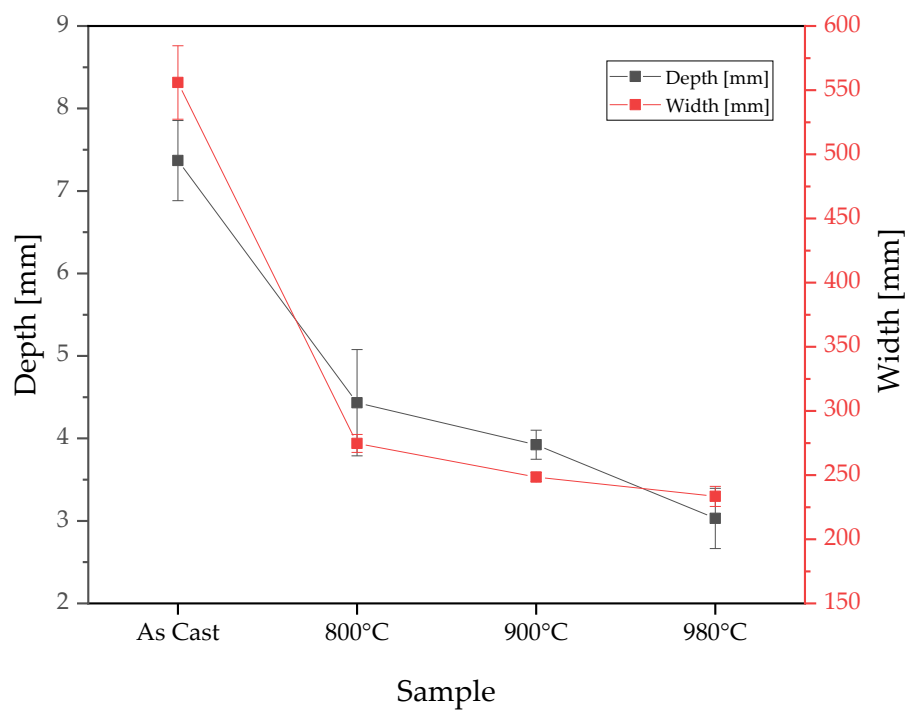


Fig. 54. Width vs. depth of wear tracks for each condition.

Ridges can also be seen on the edge of the As Cast condition track, indicating a certain plastic deformation at the edges of the wear track after the test that is not visible in the other samples, as shown in Fig. 53. Fig. 55 depicts the wear rate for all conditions studied. As can be seen, the wear rate decreased by 50% in the 800°C sample compared to the untreated condition, while it decreased by 71% and 77% in the 900°C and 980°C conditions, respectively. When comparing the overall profiles of the heat-treated samples to the untreated samples, a decrease in dimensions is clearly visible, which is consistent with the behavioral relationship established by Archad [45], which indicates that harder materials have lower wear rates. Even though the hardness measured in the matrix for the untreated and 800°C samples is very similar, the wear rate for the latter is reduced by 50%, which can be attributed to the presence of small secondary carbides distributed in the austenitic matrix. The same can be said for the difference between 900°C and 980°C conditions compared to As Cast and 800°C, and even between 900°C and 980°C. The difference between the latter conditions is attributed to a higher hardness of the martensitic matrix, which emerged after the 980°C treatment, compared to the austenitic one (900°C), as well as a higher volume fraction of secondary carbide particles, which is about 15% higher. Moreover, it is expected for the 980 sample to contain a larger fraction of the martensitic phase, which is a consequence of a larger fraction of SC and redistribution of alloy elements

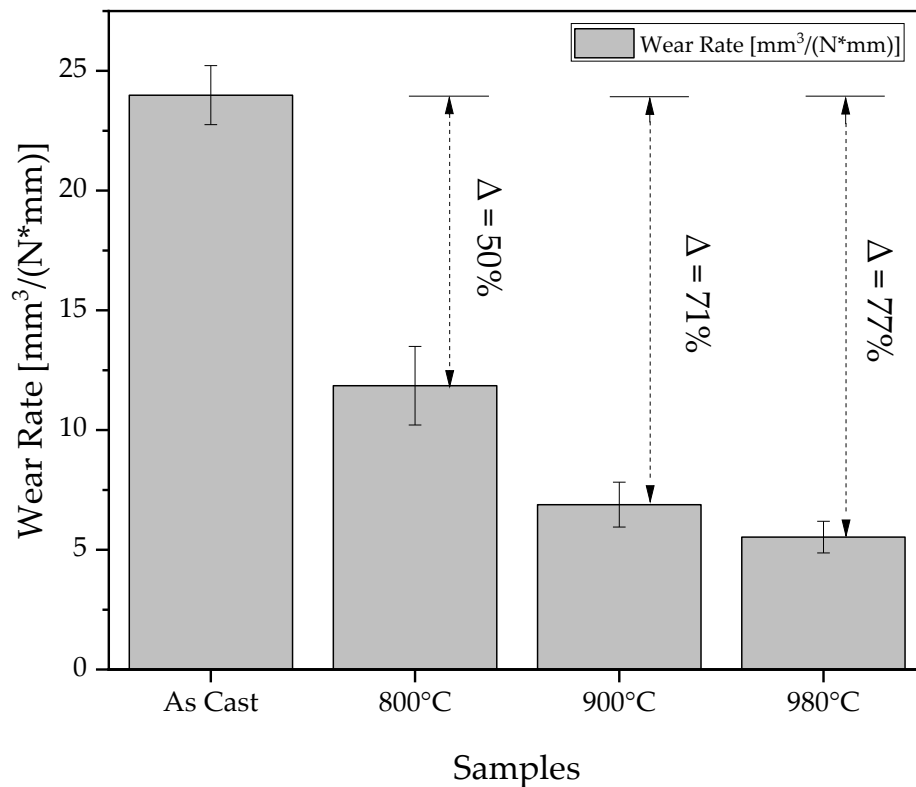


Fig. 55. Wear rate comparison on the studied samples.

The coefficient of friction (COF) is used to express the friction behavior of the specimens under the 20 N load. For each condition, the average value of the various COF measurements, along with their corresponding deviation, is plotted in Fig. 56. These curves were compared to Blau's [78] description of the most common shapes of time-dependent friction curves for sliding metal-to-metal pairs. As can be seen, they have a zone of self-accommodation or "running in," in which a rapid increase of the COF is observed until a maximum peak is reached, followed by a decrease until a characteristic stable value is obtained, from which the curve remains stable ("steady state"). The COF curve evolves similarly in all cases during the first 250 cycles, which is typical of dry metal sliding systems [78]. The elimination of the initial roughness of the two contacting bodies results in higher local contact pressures and, as a result, higher friction as the curve evolves during "running-in." This behavior could be explained further by changes in surface composition caused by the ball's sliding action on the sample surface [78], [79]. Although all of the curves are typical of dry metal-pair sliding systems, they differ in some ways. In the case of the untreated sample, the curve takes the shape of the d-curve described by Blau, with an initial peak followed by a small valley, and instead of stabilizing, it acquires a

curvature that exceeds the value of the initial peak, increasing in value with time. This indicated that there was a large number of wear particles left inside the track, which could act as a third body, increasing the coefficient of friction (higher roughness). Furthermore, this condition had the highest COF values (1.11 ± 0.05), which is consistent with the higher wear rate observed. Likewise, the 800°C curve has a similar appearance, but with values that are slightly lower than the untreated sample (1.04 ± 0.06), indicating a reduction in the coefficient of friction as well as a 50% reduction in the wear rate. For the 900°C and 980°C conditions, the curves take on the characteristic shape of Blau's type b curve, reaching a maximum peak at the start of the stroke and then stabilizing at its steady state value once the uniformity of the movement is achieved. In these cases, the average COF values are even lower than the previous ones, averaging 0.82 ± 0.03 for the 900°C sample and 0.78 ± 0.03 for the 980°C sample. Furthermore, the latter conditions reach running-in and steady-state behavior earlier than the others, which may be due to the pellet suffering less damage and thus establishing a stable contact more quickly. It should be noted that the steady state for the 900°C and 980°C samples have very little deviation from its average value, indicating that a large portion of the wear particles expelled during the test did not come into contact with the ball and thus could not act as a third body and increase abrasive wear.

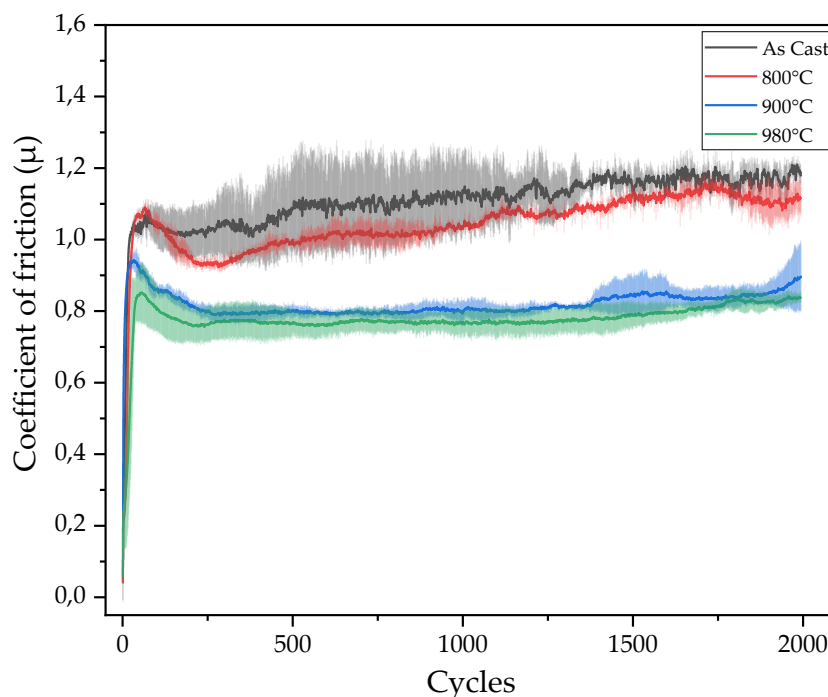


Fig. 56. Evolution of COF for the different samples.

This increase in strength of the heat-treated samples cannot be explained solely by hardness values because of a synergistic effect caused by the different phases of the microstructure, as is well known in multi-modal systems. This is because the behavior of these materials must be considered as a compound, as it is determined not only by the structure or distribution of the carbides but also by the nature of the matrix surrounding the carbides and the interaction of this set [80]. The austenite/martensite transformation of the matrix added to the secondary carbides precipitated in the treated samples plays an important role in improving the wear resistance of the 900 and 980°C samples. However, in cases where a complete martensitic transformation is not achieved (800 and 900°C), the amount of retained austenite may improve the wear response compared to the untreated sample by acting in two ways: by inactivating the formation of crack tips and by hindering the development of cracks from more brittle phases [76], as was the case with the untreated sample's footprint. SEM micrographs were taken with the two microscopes mentioned in section 5 to obtain complementary information to explain the wear response in greater detail. Furthermore, EDS analysis was performed in various areas of the prints to identify the wear mechanisms present in each condition.

6.4.1. Microstructural analysis of the 800 °C heat treated sample after wear test

Fig. 57(a) depicts a SEM micrograph of the 800°C sample's abraded surface morphology. Initially, some material transfer occurs as the Al₂O₃ ball traverses the sample surface due to the roughness of the ball, which generates a high contact pressure on the ball's asperities, causing adhesion [39], [79]. Furthermore, the reciprocating sliding and shearing action causes adhesive wear and the formation of wear particles. A closer look at the wear track in Fig. 57(b) reveals micro-cracks in the eutectic carbides that are mostly perpendicular to the sliding direction. Given that the test is performed at a load of 20 N, as reported by Nayak et al [57], and given the higher hardness of the Al₂O₃ balls (1500 HV0.01) compared to the M₇C₃ carbides (1200 HV0.01), it is expected that the carbides will crack and fracture and the matrix will be affected [11], [49]. The cracking and fragmentation of the carbides eventually leads to their ejection, as shown in Fig. 58(a) and (b). The fractionated

carbides can then act as third-body particles, resulting in the micro-cutting and micro-ploughing phenomena seen in abrasive wear, as illustrated in Fig. 58(c). It is also worth noting that the majority of the M_7C_3 carbides were cracked but not ejected from their positions; and that the cracks occurred in. This is due to the ductility of the austenitic matrix, which provides adequate mechanical support, preventing crack propagation and subsequent carbide detachment.

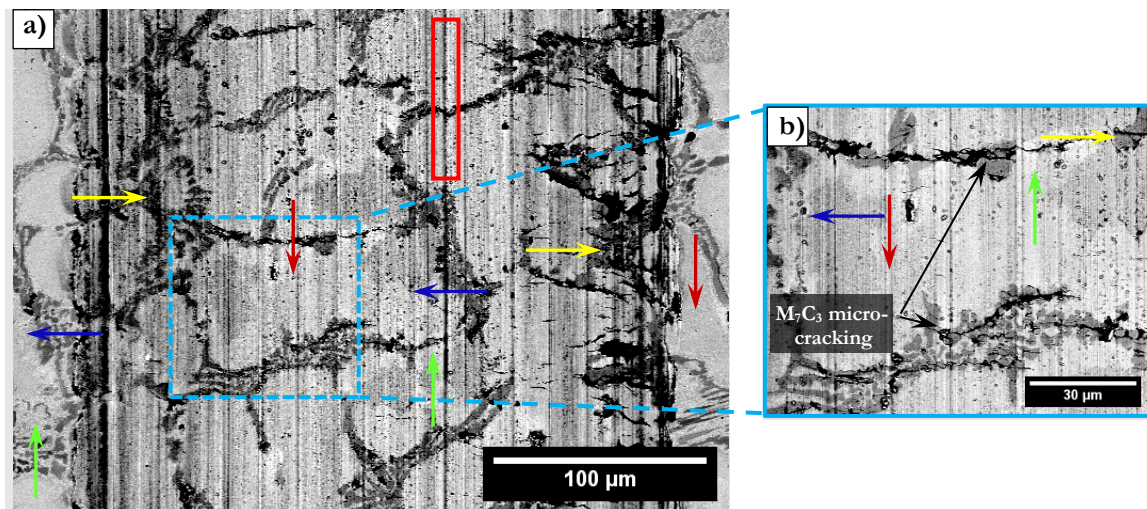


Fig. 57. a) SEM micrograph of the wear track for the 800°C sample in BSE mode, with the red rectangle representing the micro-cutting phenomenon. In eutectic carbides, the phenomenon of micro shearing or fracture is observed (b). The phases are accordingly colour and arrow labelled for reference. Austenite (γ): Red arrow pointing downwards, Martensite (α'): Green arrow pointing upwards, M_7C_3 eutectic carbide (EC): Yellow arrow pointing right, and M_7C_3 secondary carbide (SC): Blue arrow pointing left.

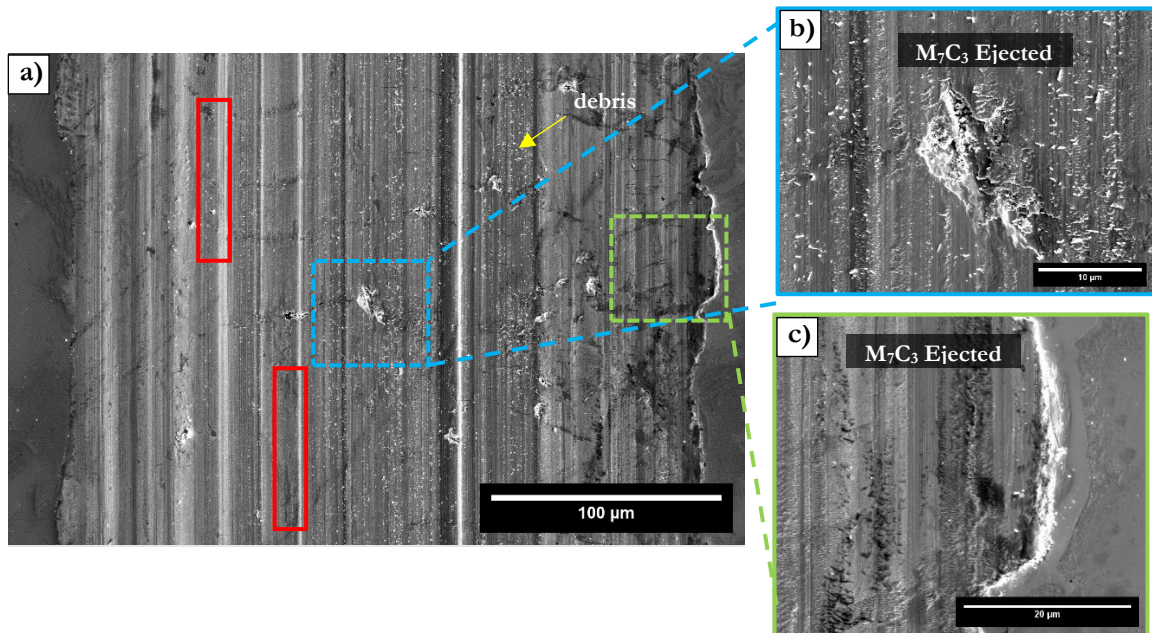


Fig. 58. (a) SEM micrograph of the wear track for the 800°C sample in BSE mode, with the red rectangle representing the micro-cutting phenomenon. In this case, the ejection of one or a fraction of a eutectic carbide particle is observed (b). In addition, the micro-sanding phenomenon of adhesive wear can be seen in (c).

Fig. 59 depicts a SEM (BSE) micrograph of the edge of the wear track where plastic deformation of the austenitic matrix occurred, as indicated by the presence of three distinct sets of slip planes, despite the presence of one or more eutectic carbides as a barrier. In contrast to what Nayak et. al. [57] reported, these planes appeared in the austenite matrix region. These slip traces are generated to accommodate the austenitic matrix's deformation caused by the tangential forces exerted by the ball during the test, which cause dislocation displacement in the matrix. It is worth noting that the slip bands stop when they reach the martensitic region or a secondary carbide zone, as shown in Fig. 59 and Fig. 60, respectively, due to the differences in the mechanical properties [58]. Nayak et al. [57] calculated the critical load for the martensite and the EC to be deformed, obtaining P_c values larger than 20N. For this reason, there is no deformation in the martensite of the EC.

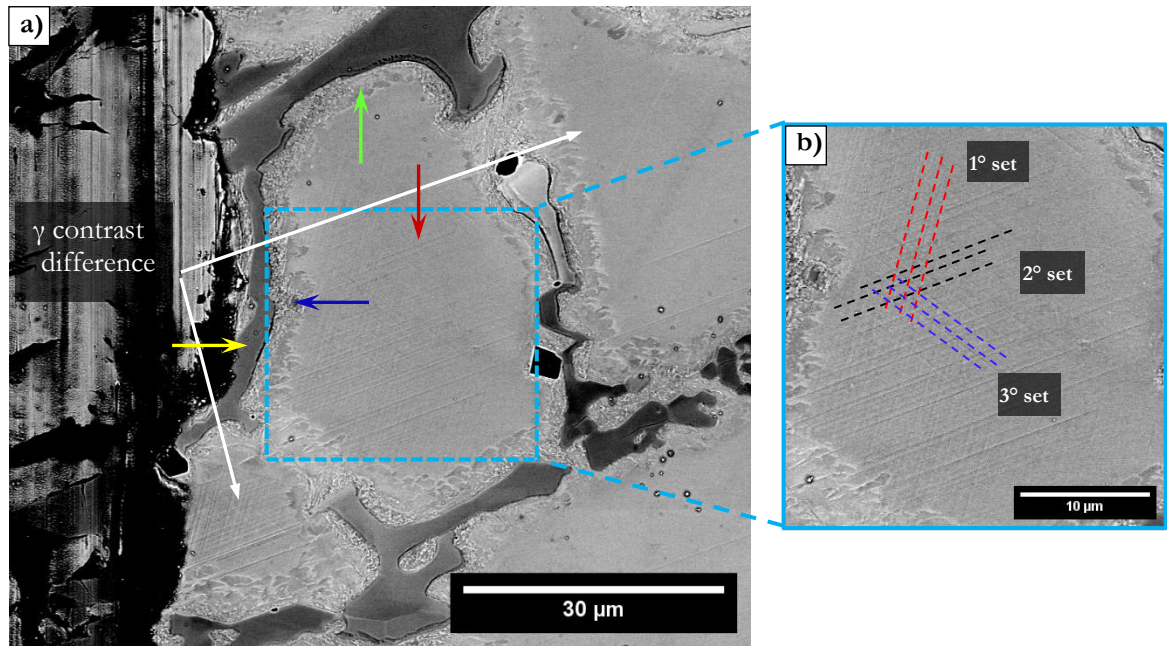


Fig. 59. (a) SEM micrograph in BSE mode of the wear track for the 800°C sample showing the austenitic matrix (γ), eutectic carbides (M_7C_3), and the contrast between deformed and undeformed austenite. (b) Displays a zoomed-in view of the boxed area, indicating the generated directions and slip sets.

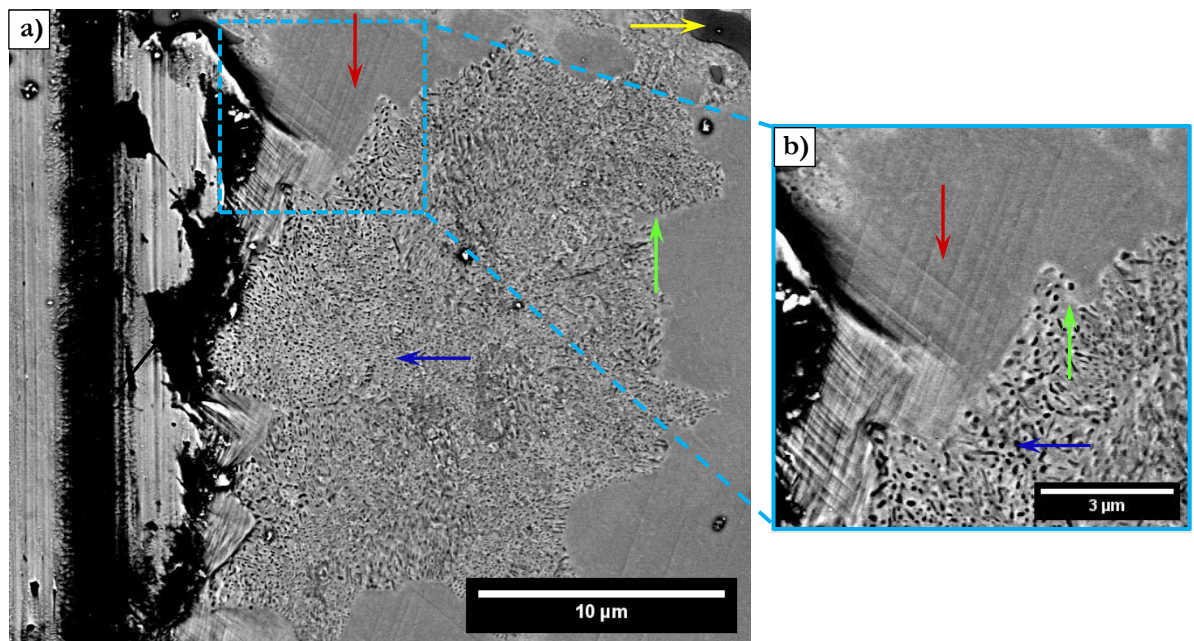


Fig. 60. a) SEM micrograph of the wear track on the 800°C sample, where it can be seen within the yellow ellipse, the stop of the slip lines when reaching the secondary carbide zone. (b) Enlarged image of the squared area.

Some oxide particles (white dots or particles) can be seen in Fig. 58. They could correspond to worn particles of alumina or of the oxidized ferritic matrix. Fig. 61(a) depicts a SEM (SE) micrograph with a 50% overlay of the EDS oxygen concentration map on the wear track. Fig. 61(b), (c), and (d) show the corresponding EDS concentration maps for iron, carbon, and chromium, respectively. The high oxygen content denoted by the intense green color in Fig. 61(a) clearly shows how the cracks formed in the wear track were covered by these oxide particles. There are also no oxidative debris particles visible outside the track. The oxidation of the sample can be caused by several factors, including the presence of humidity in the atmosphere during the test (45 % humidity) or local heating of the sample caused by the friction of the ball on the sample. Based on the findings, it was determined that the active wear mechanisms were adhesion and mild abrasion.

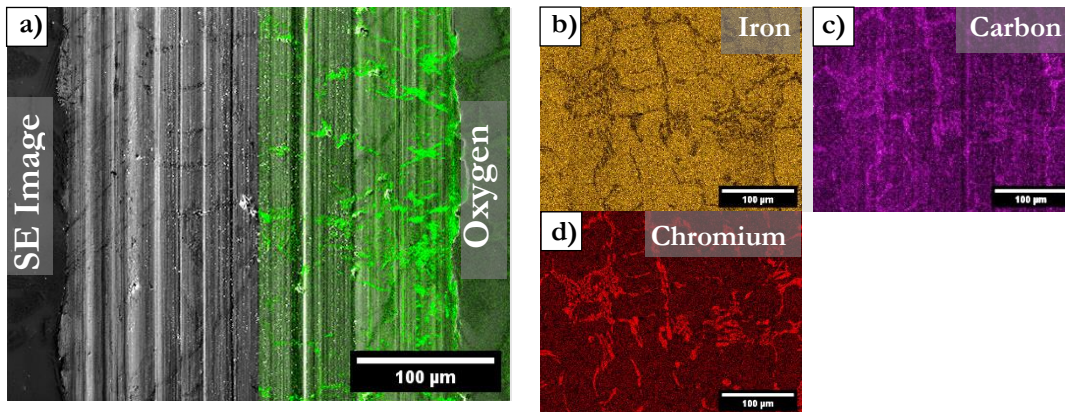


Fig. 61. (a) SE SEM micrograph with a 50% overlay of the EDS oxygen concentration map on the wear track. While the EDS concentration maps for iron, carbon, and are depicted in (b), (c), and (d), respectively.

6.4.2. Microstructural analysis of the 900°C heat treated sample after wear test

Fig. 62(a) shows an SEM micrograph of the wear track for the 900°C sample, in which it can be seen that inside the track, micro-cracks, and micro-cuts occurred in the eutectic carbides. However, in contrast to the previous conditions, these microcracks also occurred in the matrix zone inside the wear track. Although it could not be quantified, it was observed from the SEM images, that compared to the 800°C condition, there was a

higher amount of expelled EC, as can be seen in the magnified image Fig. 62(b). Furthermore, in contrast to the previous conditions, as indicated by the orange rectangle in Figures Fig. 62 and Fig. 63, wear particles or "debris" appeared on both sides of the track. This can be explained by a higher number of secondary carbides, which leads to an increase in the percentage of martensite in the matrix. The martensite, being harder and more brittle than the austenite, does not have the capacity to withstand the plastic deformations generated by the contact pressure of the ball and the cracks generated in the carbides. However, as could be seen above, the wear was minor, which may indicate that the wear particles, as they were ejected towards the edges of the wear track, did not act as third body.

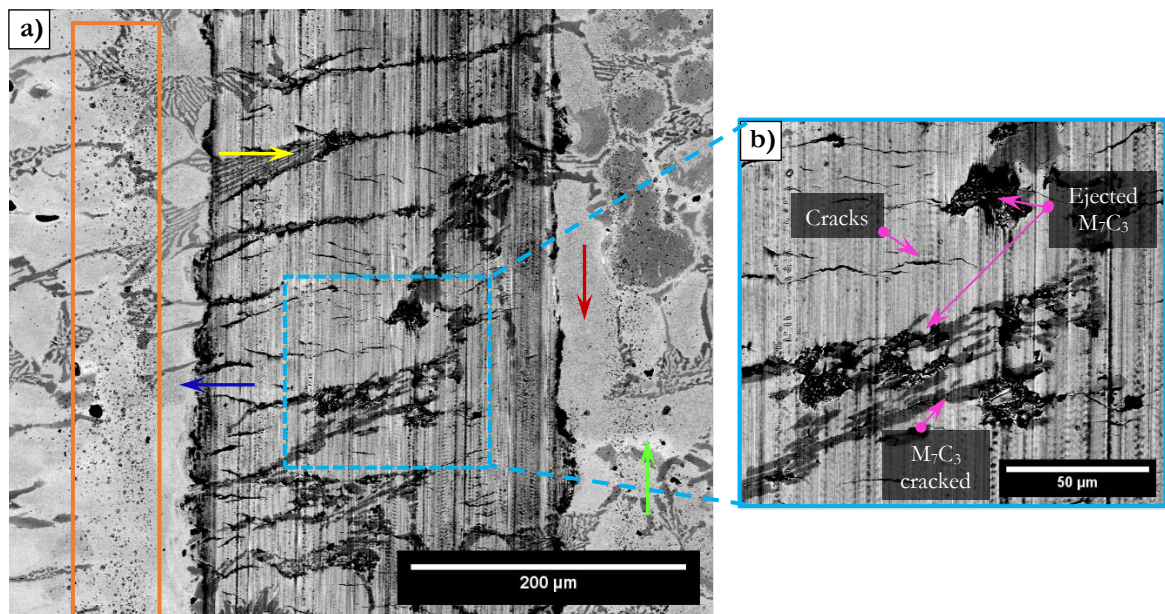


Fig. 62. SEM (BSE) micrograph of the wear track on the 900°C sample. Wear particles can be seen next to the wear track (orange rectangle). Micro cuts and micro-cracks can also be seen inside the track, near the EC, as shown in the image (b). The phases are accordingly colour and arrow labelled for reference. Austenite (γ): Red arrow pointing downwards, Martensite (α): Green arrow pointing upwards, M₇C₃ eutectic carbide (EC): Yellow arrow pointing right, and M₇C₃ secondary carbide (SC): Blue arrow pointing left.

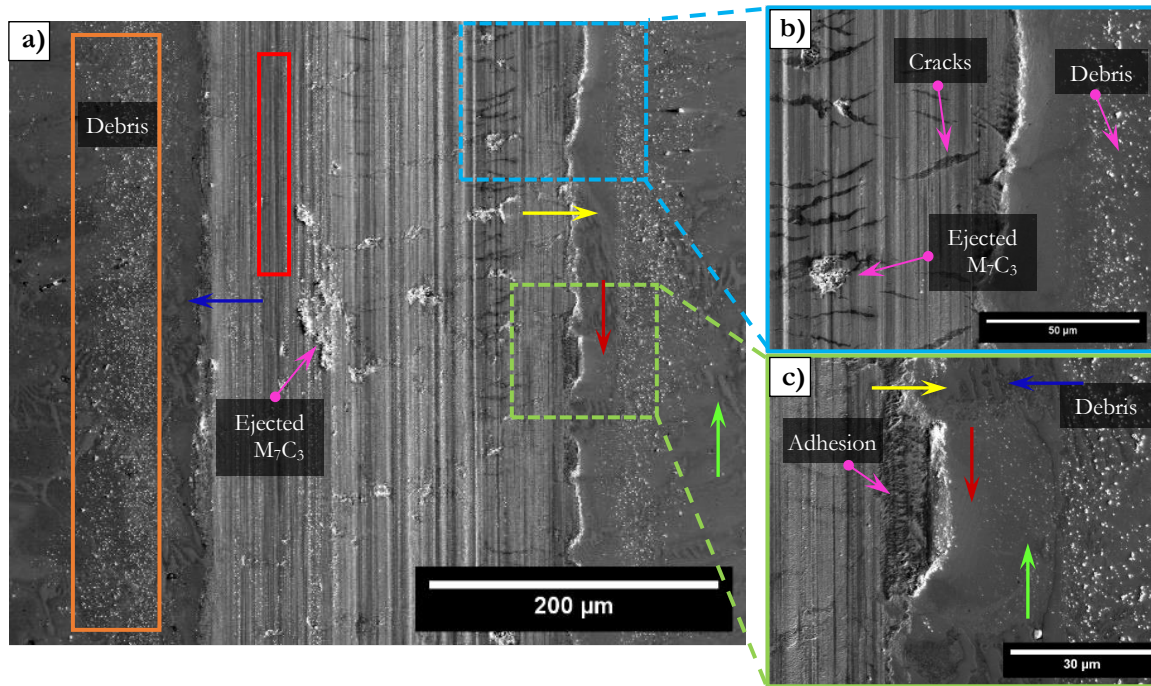


Fig. 63. SEM micrograph of the wear track on the 900°C sample, revealing wear particles (orange rectangle) and micro-cracking (red rectangle). Micro-cuts and micro-cracks can also be seen in the interior of the printtrack, close to the EC, as shown in the image (b), as well as signs of adhesion in the image (c).

Fig. 64(a) shows a SEM micrograph in SE mode with a 50% overlay of the EDS oxygen concentration map on the wear track. It denotes the preferential accumulation of oxides in areas where carbides crack and chip. Because abrasion dominates the wear mechanism, micro-cutting and ploughing contribute to surface deterioration, resulting in the formation of numerous defects such as cracks and voids. This is an important consideration because the rate of carbide removal essentially indicates the rate at which oxides accumulate and eventually decompose, altering subsequent wear behavior [55]. The light green color indicates that the cracks and traces left by the ejected carbides were filled by oxide particles. Oxides are produced during the tribological test, as are the wear particles on the outskirts of the wear track. Furthermore, Fig. 64(b) shows a closer look at the oxide accumulation where the M_7C_3 carbide was ejected, and the EDS elemental concentration maps, Fig. 64(c)-(e), show that the oxide formed is iron-chromium oxide. Looking at figure (c), it can be seen that the cracks in figure (b) were filled with oxide particles, due to the intense light green color. On the other hand, the intense red color in figure (d) indicates the presence of a eutectic carbide in this area. If images (c) and (d) are compared, it can be seen that the oxide particles not only filled the cracks generated in the vicinity of the EC, but also the cracks generated in the matrix itself.

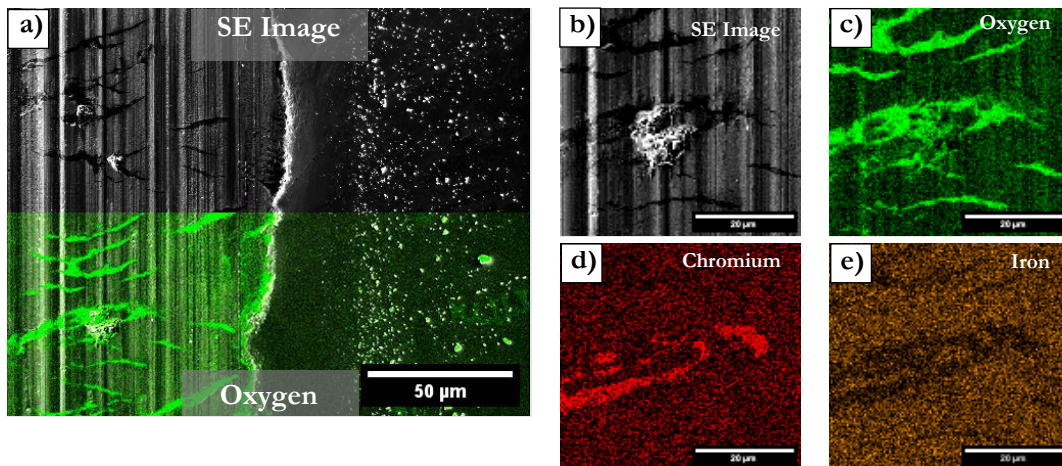


Fig. 64. (a) SEM (SE) micrograph with a 50% overlay of the EDS oxygen concentration map on the wear track. Figure (b) depicts a SE-mode SEM micrograph of the magnified region, while figures (c), (d), and (e) depict EDS concentration maps for oxygen, chromium, and iron, respectively.

Although the abrasive wear mechanism is more severe than the adhesive one, the wear rate on the 900°C sample was lower than the wear rate on the 800°C sample. This can be explained primarily by changes in the microstructure of the matrix and the fact that, as shown in Fig. 64(a), the oxide particles formed during the test do not remain in the contact zone but are expelled, accumulating on the sides of the wear track. As a result, while the wear mechanism is primarily abrasive in this case, it is mild due to the low presence of oxide particles acting as a third body inside the track.

6.4.3. Microstructural analysis of the 980°C heat treated sample after wear test

Finally, the wear test was performed at 980°C, and the SEM micrographs of the wear track shown in Fig. 65(a). Unlike the other conditions, no slip planes were observed at the track's edges as a consequence of stress generation. This is because, at 980°C, the austenitic matrix has largely transformed into martensite, which requires higher stress to activate its slip planes. Furthermore, because it is more brittle but also more resistant to friction and fatigue than the austenitic matrix, the martensitic matrix provides better wear behavior. Consequently, the generation of cracks and debris particles, as well as the expulsion of carbides, was increased in this condition, the cyclic sliding wear rate decreased. As previously stated, when wear particles remain within the contact zone, they generate

more abrasion and thus a higher wear rate. The presence of a large number of wear particles at the track's edges rather than on the track, as shown in Fig. 65(a), would explain the lower wear rate obtained for this condition.

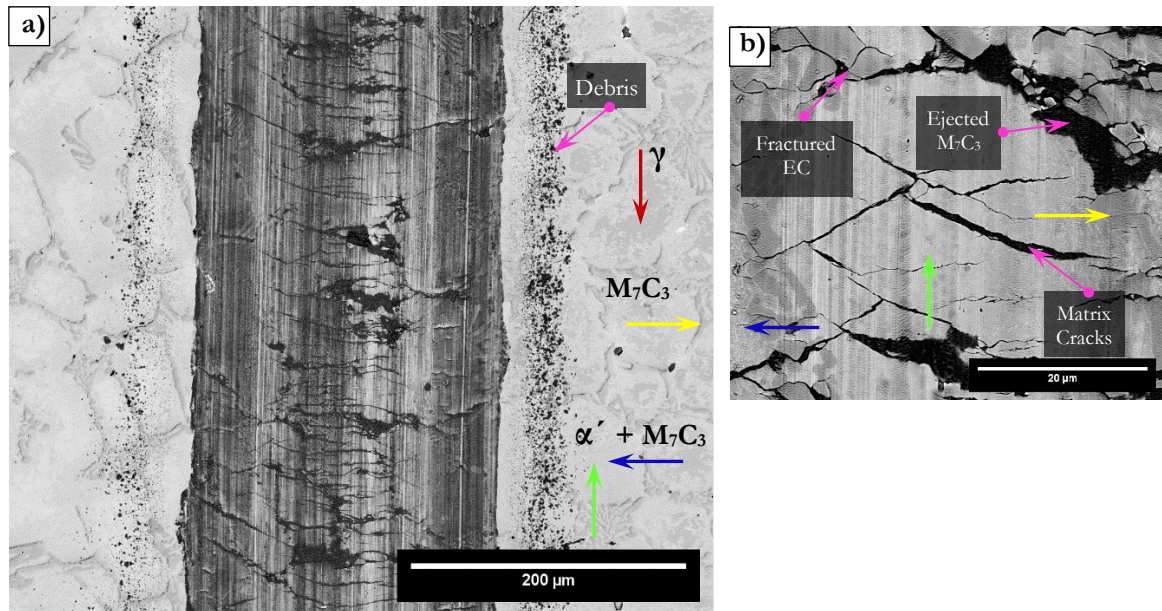


Fig. 65.(a) SEM EBS micrograph of the wear track on the 980°C sample, with wear particles visible at the track's edges. The fractured and ejected carbides, as well as the cracks generated, are visible (b). The phases are accordingly colour and arrow labelled for reference. Austenite (γ): Red arrow pointing downwards, Martensite (α'): Green arrow pointing upwards, M_7C_3 eutectic carbide (EC): Yellow arrow pointing right, and M_7C_3 secondary carbide (SC): Blue arrow pointing left.

Fig. 66(a) depicts the wear particles on the track's edges more clearly. The enlarged Fig. 66(b) shows the micro-cutting phenomena generated on the martensitic matrix and the edges of the eutectic carbides, as well as their detachment, which left voids covered with wear particles, indicating adhesion. Furthermore, the phenomenon of abrasive wear can be identified, as evidenced by a large number of characteristic micro-ploughing grooves in the sliding direction, confirming that this is the dominant mechanism.

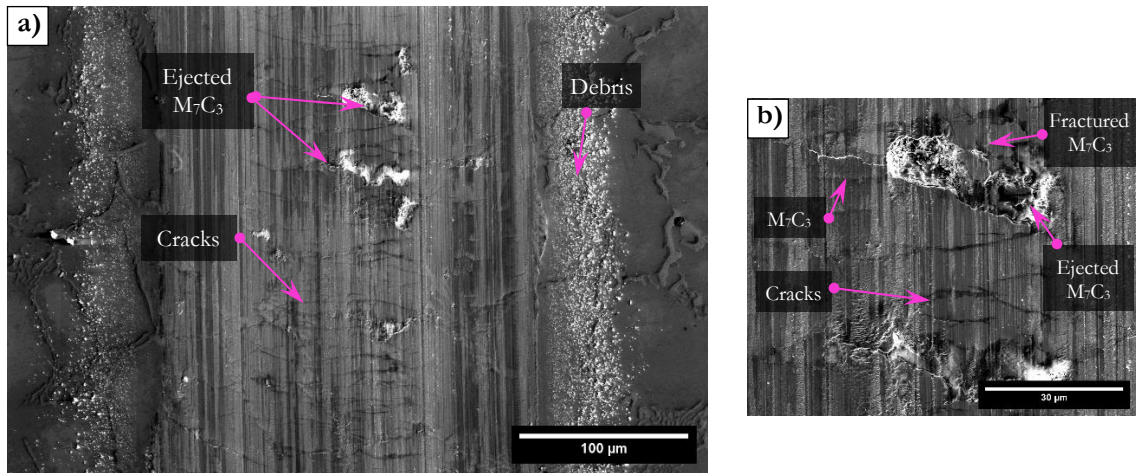


Fig. 66. (a) SEM micrograph of the wear track on the 980°C sample, with wear particles visible at the track's edges. The fractured and ejected carbides, as well as the cracks generated, are visible in (b).

Fig. 67(a) shows a SEM micrograph of the 980°C sample in SE mode, with a 50% overlay of the EDS oxygen concentration map on the wear track. It indicates the preferential accumulation of oxides in areas where carbides were cracked and chipped, as well as in areas where microcracks have been generated. This image verifies that the particles accumulated at the edges of the track correspond to oxides formed during the wear test. The EDS maps in Figs. (b) and (c) can be seen, with brown, red, and green colors indicating the elements iron, chromium, and oxygen, respectively.

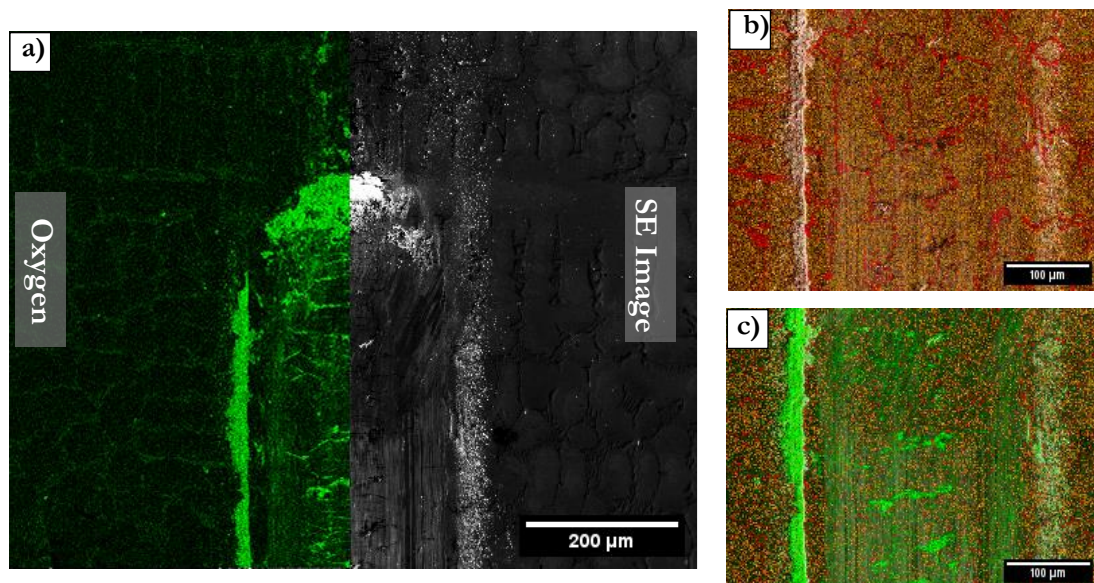


Fig. 67. (a) SE SEM micrograph with a 50% overlay of the EDS oxygen concentration map on the wear track. (b) SE mode micrograph with 100 percent overlay of Fe (brown) and Cr (red) EDS concentration maps (red). (c) SE mode micrograph with 100 percent overlay of Fe (brown), Cr (red), and O EDS concentration maps (green).

CHAP. 7: SUMMARY AND CONCLUSIONS

This was an applied research project that used the scientific method to push the frontier of knowledge in materials science, specifically in the design of heat treatments to achieve a specific microstructure. The project took place as part of a collaborative research grant between the Surface Engineering Group of the Facultad Regional Concepción del Uruguay, Universidad Tecnológica Nacional, and the Functional Materials Group of Saarbrücken University, Saarbrücken, Germany.

Initially, an exhaustive analysis of the available knowledge on the subject was carried out, followed by the experimental part, which began with the preparation of the samples and the implementation of the different heat treatments, followed by the study of the microstructure by means of different characterization techniques, wear tests and their subsequent characterization, and finally the analysis of the results. In this chapter, a summary of the results obtained, and the most important conclusions are presented.

7.1. SYNTHESIS OF RESULTS

Iron castings containing 16% Cr were subjected to three different heat treatments: 800, 900, and 980°C, followed by rapid cooling in water, to evaluate the microstructural changes that occurred during the heating up to the desired temperature. Furthermore, their response to reciprocating sliding wear behavior was investigated.

In the sample without any heat treatment (As Cast), the microstructure consisted of a matrix of austenitic dendrites with eutectic carbides of the type M_7C_3 , which are surrounded by a thin martensite zone. As expected, no secondary carbides were observed in this microstructure [16], [38]. In terms of wear behavior, it presented the wear track with the largest dimensions, thus, the highest wear rate (23.98 ± 1.23 [$\text{mm}^3/(\text{N} \times \text{mm})$]). In the wear track profile, it could be observed that, unlike the other conditions, it presented ridges on the edges, which would indicate a plastic deformation of the matrix. The coefficient of friction for this sample had the highest average value (1.11 ± 0.05), and its curve did not have a stable state value but continued increasing with the number of cycles. No

debris particles were observed on the outskirts of the track. The latter could explain that wear particles could have been trapped inside the track and could act as a third body, increasing the abrasive wear mechanism, thus increasing the coefficient of friction (due to the higher roughness) and the wear rate.

In the sample treated at 800°C, which is the temperature at which SC nucleation begins, the microstructure was mainly constituted by an austenitic matrix and EC, with the presence of SC at the edges of the austenite dendrites, which were surrounded by a thin martensitic region. Regarding the morphology of the secondary carbides, they had mostly rounded shapes, and it was expected that the particle size measured was the smallest of all the samples (0.007 ± 0.009), as well as the secondary carbides volume fraction, the latter being around (2.85 ± 0.59), approximately 37% smaller than the samples treated at higher temperatures. The presence of the small SCs dispersed in the austenitic matrix, together with a small portion of martensitic matrix surrounding them, managed to decrease the wear rate by 50% compared to the untreated sample. However, the coefficient of friction did not do so in the same way but had a decrease of 6% and its profile shape was similar to the As Cast sample. Due to the higher hardness of the ball, it was expected that the eutectic carbides would crack and spall, generating wear particles that could act as a third body, increasing the abrasive wear. It is important to mention that cracks were generated between the M_7C_3 EC and the matrix as well as that the ECs were not expelled from their position. This is due to the ductility of the austenitic matrix, which provides adequate mechanical support, inhibiting crack propagation and the subsequent ejection of the ECs. Therefore, SEM micrographs showed the activation of three distinct slip planes in the austenitic matrix at the edges of the wear track, which were generated by the contact pressure of the ball. It should be noted that these lines stopped when they reached a martensitic zone, due to the change in the crystalline structure, and higher hardness, which requires the application of higher stress to activate its slip planes. In both CLSM and SEM images, practically no wear particles were observed on the outskirts of the wear track, so it can be said that the wear mechanism was similar to that of the As Cast sample. On the other hand, by analyzing the EDS maps of the wear track, it could be observed that there was oxidative wear inside the wear track, judging by a large number of oxide particles that filled the cracks that were generated around the ECs.

In the 900°C sample, showed 36% (4.48 ± 0.59) more secondary carbides dispersed in the austenitic matrix increase, with larger particles size when compared to the 800°C

sample, according to the distribution-rug plot. This increase in the amount of SC consequently led to an increase in the percentage of martensite in the matrix. This resulted in a decrease in the wear rate (6.88 ± 0.93), being 70% and 42% lower than the As Cast and the 800°C sample, respectively. On the other hand, the COF also decreased, with an average value of 0.82 ± 0.03 , being 25% and 18% lower than the As Cast and the 800°C sample, respectively. It is worth noting that the shape of the COF curve in this case is similar to the characteristic curves for a dry metal-to-metal contact because it is set at a constant value. In the SEM micrographs in BSE mode of the wear track, it could be observed that, like the 800°C condition, cracks and fractures were generated at the edges of the ECs. Moreover, in the 900°C condition, only a few ECs were fractured and ejected from the contact zone, and some cracks were generated within the matrix itself (not in the vicinity of the ECs). In addition, a significant amount of wear particles could be seen on both sides of the wear track. This can be partly explained by the increased amount of martensite in the matrix, which, being harder and more brittle, is not able to deform to withstand the plastic deformation generated by the contact pressure of the ball and the cracks generated in the carbides. However, the wear rate was lower, which would indicate that these wear particles, when expelled out of the ball contact zone, did not act as a third body. The EDS analysis confirms that these wear particles belong to iron-chromium oxides formed during the wear test, which filled the voids left by the fractured and ejected carbides.

Finally, in the sample treated at 980°C, the microstructure consisted essentially of martensite due to the higher number of secondary carbides dispersed in the matrix, with few remaining austenite zones. This condition had the highest volume fraction of secondary carbides (4.54 ± 1.53), and the highest number of particles with the larger size. Regarding the matrix hardness, it was the only sample in which an increase was seen concerning the other conditions, being 30%. From the SEM micrographs, cracks and grooves were visible on all the abraded surfaces, as in the rest of the samples. It was evident that the wear mechanism was a combination of adhesive and abrasive wear, with a greater predominance of the latter. On the other hand, cracks or grooves generated in the matrix, far from the ECs, were seen. Although not quantified, the density of these cracks and grooves had increased, and some of the EC were fractured and ejected. This was verified by contrasting the EDS images of the different elements present on the wear track. It is worth mentioning that for the 980°C sample, no slip planes were observed at the edges

of the wear track. Although they were not quantified due to the lack of methods to do so, more debris was seen on both sides of the track, in contrast with the 900°C sample. However, the wear rate has decreased (5.52 ± 0.66), being 77% and 20% lower than the As Cast and the 900°C sample, respectively. On the other hand, the COF also decreased (0.78 ± 0.03), resulting in 31% and 5% lower than the As Cast and the 900°C sample, respectively. The COF curve had a very similar shape to that described for the 900°C condition. This improvement in the wear response of the 980°C condition can be attributed to the fact that the wear particles, due to the higher strength of the system: martensitic matrix, EC, and the higher amount of SC, have a greater tendency to be expelled out of the wear track, avoiding contact as third body particles.

According to the above summary, it can be indicated that for the alloy studied, and in accordance with the predictions made by computer simulations by Nayak et al [38], M_7C_3 secondary carbides precipitation starts during heating at temperatures just below 800°C. The increase in heat treatment temperature, followed by rapid cooling, showed an increase in the size of the SCs, hence in their volume fraction, as well as a transformation of the austenitic matrix into a martensitic structure. This led to an increase in the hardness of the matrix and consequently, in the wear resistance under reciprocating sliding condition of the system.

7.2. DEGREE OF ACHIEVEMENT OF OBJECTIVES

The objectives were successfully achieved because, throughout this work, we contributed to understanding the kinetics and nature of secondary carbide precipitation occurring in a HCCI_16%Cr during heating up to the destabilization temperature. As expected, in addition to the variation in the size and fraction of secondary carbides, other microstructural modifications that occur as a function of the reached temperature, such as the transformation of austenite to martensite during cooling, could be confirmed. These factors affect the mechanical and tribological response of the material. Therefore, this work quantified the tribological response of a HCCI_16%Cr, with its different microstructures modified during heating, to cyclic wear.

7.3. EVALUATION OF RESULTS

The results obtained in this research project are scientifically relevant. As shown in the background review, although there are many publications on iron castings with a high content of alloying elements, especially chromium, the heat treatment parameters for the precipitation of secondary carbides for this microstructure have not been established. The influence of the microstructure on the sliding wear behavior has not been thoroughly investigated. In this project, a solid, well-founded research task has been carried out in order to extend the frontier of scientific knowledge on these topics. On the basis of this research, a paper will be prepared for submission to an international journal for publication.

CHAP. 8: REFERENCES

- [1] “Tecnología Industrial II. Materiales.: Estructura cristalina.” <https://materialesti2.blogspot.com/p/estructura.html> (accessed Sep. 13, 2022).
- [2] S. H. Avner, *Introduction to Physical Metallurgy*. 1974.
- [3] M. Hinojosa, “La Estructura Cristalina de los Metales,” *Ingenierías*, vol. 3, no. 8, pp. 20–25, 2000.
- [4] “Deformación cristalina a escala,” pp. 85–110, 2003.
- [5] P. Mec, “Defectos en estructuras cristalinas: Defectos puntuales:” <https://www.youtube.com/watch?v=n-HkS2mgjDo> (accessed Sep. 13, 2022).
- [6] Newell J., “Estructura de los materiales,” *Cienc. Mater. en Ing.*, p. 704, 2016.
- [7] A. Maxime, “Estudio de la viabilidad sobre el uso de los modelos de plasticidad cristalina en la modelización de la deformación plástica de cristales hexagonales,” pp. 1–8, 2012, [Online].
- [8] J. Ignacio and S. Hidalgo, “Mecanismo de deformación: Deslizamiento de dislocaciones.” [Online]. Available: <https://slideplayer.es/slide/12245186/>
- [9] GM Manufacturing, “Sistema de deslizamiento en diferentes estructuras cristalinas,” *Slidersbeir*, 2015. <https://es.slideshare.net/carlosarreola395/93-sistemas-de-deslizamiento-en-diferentes-cristales>
- [10] W. Plieth, “Electrochemistry for Materials Science,” *Electrochemistry for Materials Science*. 2008. doi: 10.1016/B978-0-444-52792-9.X5001-5.
- [11] P. J. T. H, “Structure and wear performance of abrasion resistance chromium white cast irons,” *Trans Am Foundrymen’s Soc*, vol. 92, pp. 599–622, 1984.
- [12] M. Ngqase and X. Pan, “An Overview on Types of White Cast Irons and High Chromium White Cast Irons,” in *Journal of Physics: Conference Series*, 2020, vol. 1495, no. 1. doi: 10.1088/1742-6596/1495/1/012023.
- [13] C. U. Chisholm, “Materials and processes in manufacturing (5th edn.),” *J. Mech. Work. Technol.*, vol. 6, no. 1, pp. 95–96, 1982, doi: 10.1016/0378-3804(82)90022-5.
- [14] G. Laird, R. Gundlach, and K. Rohrig, *Abrasion-Resistant Cast Iron Handbook*. 2000.

- [Online]. Available: www.afsinc.org
- [15] A. Bedolla-Jacuinde, B. Hernández, and L. Béjar-Gómez, “SEM study on the M7C3 carbide nucleation during eutectic solidification of high-chromium white irons,” *Zeitschrift fuer Met. Res. Adv. Tech.*, vol. 96, no. 12, pp. 1380–1385, 2005, doi: 10.3139/146.101188.
- [16] M. A. Guitar *et al.*, “High Chromium Cast Irons: Destabilized-Subcritical Secondary Carbide Precipitation and Its Effect on Hardness and Wear Properties,” *J. Mater. Eng. Perform.*, vol. 27, no. 8, pp. 3877–3885, 2018, doi: 10.1007/s11665-018-3347-1.
- [17] M. Durand-Charre, *Microstructure steels and Cast of Irons*, 2004th ed. Paris.
- [18] C. P. Tabrett, I. R. Sare, and M. R. Ghomashchi, “Microstructure-property relationships in high chromium white iron alloys,” *Int. Mater. Rev.*, vol. 41, no. 2, pp. 59–82, 1996, doi: 10.1179/imr.1996.41.2.59.
- [19] W. R. Thorpe and B. Chicco, “The Fe-rich corner of the metastable C-Cr-Fe liquidus surface,” *Metallurgical Transactions A*, vol. 16, no. 9, pp. 1541–1549, 1985. doi: 10.1007/BF02663011.
- [20] M. F. and U.-N. R., “Factors affecting the structure of chromium and chromium-molybdenum white irons,” *Climax Molybdenum SA*, pp. 1–32, 1971.
- [21] A. B. Jacuinde and W. M. Rainforth, “The wear behaviour of high-chromium white cast irons as a function of silicon and Mischmetal content,” *Wear*, vol. 250–251, no. PART 1, pp. 449–461, 2001. doi: 10.1016/S0043-1648(01)00633-0.
- [22] K. F. Pinho, C. Boher, and C. Scandian, “Effect of molybdenum and chromium contents on sliding wear of high-chromium white cast iron at high temperature,” *Lubr. Sci.*, vol. 25, no. 2, pp. 153–162, 2013, doi: 10.1002/lis.1171.
- [23] Ulbrinox, “Fundamentos de las condiciones de templado del acero...” <https://www.ulbrinox.com.mx/blog/fundamentos-de-las-condiciones-de-templado-del-acero-inoxidable> (accessed Sep. 16, 2022).
- [24] V. I. Transformaciones and D. E. L. A. Austenita, “Vi. transformaciones de la austenita fuera del equilibrio,” pp. 1–6.
- [25] A. Wiengmoon, “Carbides in high chromium cast irons,” *Naresuan Univ. Eng. J.*,

- vol. 6, no. 1, pp. 64–70, 2011, doi: 10.14456/nuej.2011.6.
- [26] R. Benz, J. F. Elliott, and J. Chipman, “Thermodynamics of the carbides in the system Fe-Cr-C,” *Metall Trans*, vol. 5, no. 10. pp. 2235–2240, 1974. doi: 10.1007/BF02643938.
- [27] A. Bedolla-Jacuinde, R. Correa, I. Mejía, J. G. Quezada, and W. M. Rainforth, “The effect of titanium on the wear behaviour of a 16%Cr white cast iron under pure sliding,” *Wear*, vol. 263, no. 1-6 SPEC. ISS., pp. 808–820, 2007, doi: 10.1016/j.wear.2006.12.011.
- [28] S. T. Petrovic, S. Markovic, and Z. A. Pavlovic, “The effect of boron on the stereological characteristics of the structural phases present in the structure of the 13% Cr white iron,” *Journal of Materials Science*, vol. 38, no. 15. pp. 3263–3268, 2003. doi: 10.1023/A:1025133904322.
- [29] R. Correa, A. Bedolla-Jacuinde, J. Zuno-Silva, E. Cardoso, and I. Mejía, “Effect of boron on the sliding wear of directionally solidified high-chromium white irons,” *Wear*, vol. 267, no. 1–4, pp. 495–504, 2009, doi: 10.1016/j.wear.2008.11.009.
- [30] J. R. Davis and M. Park, *Alloying: understanding the basics*, vol. 39, no. 09. 2002. doi: 10.5860/choice.39-5209.
- [31] G. L. F. Powell and G. Laird, “Structure, nucleation, growth and morphology of secondary carbides in high chromium and Cr-Ni white cast irons,” *Journal of Materials Science*, vol. 27, no. 1. pp. 29–35, 1992. doi: 10.1007/BF02403640.
- [32] J. Asensio, J. A. Pero-Sanz, and J. I. Verdeja, “Microstructure selection criteria for cast irons with more than 10 wt.% chromium for wear applications,” *Mater. Charact.*, vol. 49, no. 2, pp. 83–93, 2002, doi: 10.1016/S1044-5803(02)00260-7.
- [33] A. Bedolla-Jacuinde, L. Arias, and B. Hernández, “Kinetics of secondary carbides precipitation in a high-chromium white iron,” *Journal of Materials Engineering and Performance*, vol. 12, no. 4. pp. 371–382, 2003. doi: 10.1361/105994903770342881.
- [34] A. E. Karantzalis, A. Lekatou, and E. Diavati, “Effect of destabilization heat treatments on the microstructure of high-chromium cast iron: A microscopy examination approach,” *J. Mater. Eng. Perform.*, vol. 18, no. 8, pp. 1078–1085, 2009, doi: 10.1007/s11665-009-9353-6.
- [35] Z. Sun, R. Zuo, C. Li, B. Shen, J. Yan, and S. Huang, “TEM study on precipitation

- and transformation of secondary carbides in 16Cr-1Mo-1Cu white iron subjected to subcritical treatment,” *Mater. Charact.*, vol. 53, no. 5, pp. 403–409, 2004, doi: 10.1016/j.matchar.2004.09.007.
- [36] A. E. Karantzalis, A. Lekatou, and H. Mavros, “Microstructural Modifications of As-Cast High-Chromium White Iron by Heat Treatment,” *J. Mater. Eng. Perform.*, vol. 18, no. 2, pp. 174–181, 2009, doi: 10.1007/s11665-008-9285-6.
- [37] Ö. N. Doğan, J. A. Hawk, and G. Laird, “Solidification structure and abrasion resistance of high chromium white irons,” *Metall. Mater. Trans. A Phys. Metall. Mater. Sci.*, vol. 28, no. 6, pp. 1315–1328, 1997, doi: 10.1007/s11661-997-0267-3.
- [38] M. A. Guitar, U. P. Nayak, D. Britz, and F. Mücklich, “The Effect of Thermal Processing and Chemical Composition on Secondary Carbide Precipitation and Hardness in High-Chromium Cast Irons,” *Int. J. Met.*, vol. 14, no. 3, pp. 755–765, 2020, doi: 10.1007/s40962-020-00407-4.
- [39] I. Hutchings and P. Shipway, *Tribology: Friction and wear of engineering materials: Second Edition*. 2017.
- [40] K. H. Zum Gahr, “Microstructure and wear of materials.,” *Amsterdam, Netherlands, Elsevier Sci. Publ. B.V., 1987*, vol. 10) (ISBN, 1987, doi: 10.1016/0043-1648(88)90112-3.
- [41] J. Hailing, *Encyclopedia of tribology*, vol. 150, no. 1–2. Elsevier, 1991. doi: 10.1016/0043-1648(91)90333-p.
- [42] G. Straffelini, “Springer Tracts in Mechanical Engineering Friction and Wear Methodologies for Design and Control.” pp. 44–48, 2015. [Online]. Available: <http://www.springer.com/series/11693>
- [43] G. W. Stachowiak and A. W. Batchelor, “e n g i n e e r i n g t r i b o l o g y.”
- [44] Y. J. J. Jason, H. G. How, Y. H. Teoh, and H. G. Chuah, “A study on the tribological performance of nanolubricants,” *Processes*, vol. 8, no. 11. MDPI AG, pp. 1–33, 2020. doi: 10.3390/pr8111372.
- [45] J. F. Archard, “Contact and rubbing of flat surfaces,” *J. Appl. Phys.*, vol. 24, no. 8, pp. 981–988, 1953, doi: 10.1063/1.1721448.
- [46] G. W. Stachowiak and A. W. Batchelor, *Engineering Tribology: Fourth Edition*. 2013.

- doi: 10.1016/C2011-0-07515-4.
- [47] J. K. Fulcher, T. H. Kosel, and N. F. Fiore, “The effect of carbide volume fraction on the low-steel abrasion resistance of high CR-MO white cast irons.,” *Wear*, vol. 84. pp. 313–325, 1981.
- [48] K. H. Zum Gahr and D. V. Doane, “Optimizing fracture toughness and abrasion resistance in white cast irons,” *Metallurgical Transactions A*, vol. 11, no. 4. pp. 613–620, 1980. doi: 10.1007/BF02670698.
- [49] R. B. Gundlach and J. L. Parks, “Influence of abrasive hardness on the wear resistance of high chromium irons,” *Wear*, vol. 46, no. 1. pp. 97–108, 1978. doi: 10.1016/0043-1648(78)90113-8.
- [50] K. Abdel-Aziz, M. El-Shennawy, and A. A. Omar, “Microstructural characteristics and mechanical properties of heat treated high-cr white cast iron alloys,” *International Journal of Applied Engineering Research*, vol. 12, no. 14. pp. 4675–4686, 2017. [Online]. Available: <http://www.ripublication.com>
- [51] O. F. Higuera-Cobos, F.-D. Dumitru, and D. H. Mesa-Grajales, “Mejoramiento de la resistencia al desgaste abrasivo de la fundición al alto cromo ASTM A-532 a través de ciclos de tratamiento térmico,” *Rev. Fac. Ing.*, vol. 25, no. 41, pp. 93–103, 2016, doi: 10.19053/01211129.4141.
- [52] S. Inthidech, P. Kosasu, S. Yotee, and Y. Matsubara, “Effect of repeated tempering on abrasive wear behavior of hypoeutectic 16 mass% Cr cast iron with molybdenum,” *Mater. Trans.*, vol. 54, no. 1, pp. 28–35, 2013, doi: 10.2320/matertrans.M2012185.
- [53] G. Pintaude, F. G. Bernardes, M. M. Santos, A. Sinatora, and E. Albertin, “Mild and severe wear of steels and cast irons in sliding abrasion,” *Wear*, vol. 267, no. 1–4, pp. 19–25, 2009, doi: 10.1016/j.wear.2008.12.099.
- [54] S. Turenne, F. Lavallée, and J. Masounave, “Matrix microstructure effect on the abrasion wear resistance of high-chromium white cast iron,” *Journal of Materials Science*, vol. 24, no. 8. pp. 3021–3028, 1989. doi: 10.1007/BF02385662.
- [55] A. Bedolla-Jacuinde and W. M. Rainforth, “Electron microscopy analysis on the worn surface of a high-chromium white iron during dry sliding contact,” in *Materials Research Society Symposium Proceedings*, 2005, vol. 843, pp. 299–304. doi:

- 10.1557/proc-843-t7.4.
- [56] M. Pokusová, I. Berta, and E. Šooš, “Abrasion Resistance of as-Cast High-Chromium Cast Iron,” *Sci. Proc. Fac. Mech. Eng.*, vol. 22, no. 1, pp. 75–80, 2014, doi: 10.2478/stu-2014-0013.
- [57] U. P. Nayak, S. Suárez, V. Pesnel, F. Mücklich, and M. A. Guitar, “Load dependent microstructural evolution in an as-cast 26% Cr high chromium cast iron during unlubricated sliding,” *Friction*, vol. 10, no. 8, pp. 1258–1275, 2022, doi: 10.1007/s40544-021-0553-x.
- [58] “Physical principles of electron microscopy,” *Mater. Today*, vol. 8, no. 12, p. 49, Dec. 2005, doi: 10.1016/S1369-7021(05)71290-6.
- [59] A. Us and K. Personnel, “How SEM Works,” 2016. <https://www.nanoscience.com/techniques/scanning-electron-microscopy/>
- [60] D. Brandon and W. D. Kaplan, *Microstructural Characterization of Materials: 2nd Edition*. 2008. doi: 10.1002/9780470727133.
- [61] Ixrfsystems, “Scanning Electron Microscopy - Theory and Instrumentation.” <https://www.ixrfsystems.com/electron-microscopy/> (accessed Sep. 23, 2022).
- [62] U. P. Nayak, M. Müller, D. Britz, M. A. Guitar, and F. Mücklich, “Image Processing using Open Source Tools and their Implementation in the Analysis of Complex Microstructures,” *Pract. Metallogr.*, vol. 58, no. 8, pp. 484–506, 2021, doi: 10.1515/pm-2021-0039.
- [63] Leica Microsystems, “Leica DCM 3D User Manual,” 2012. <https://www.leica-microsystems.com>
- [64] S. W. Paddock, “Confocal laser scanning microscopy,” *Biotechniques*, vol. 27, no. 5, pp. 992–1004, 1999, doi: 10.2144/99275ov01.
- [65] J. Tomáščík, H. Šebestová, R. Čtvrtlík, and P. Schovánek, “Laser scanning confocal microscopy in materials engineering,” *18th Czech-Polish-Slovak Opt. Conf. Wave Quantum Asp. Contemp. Opt.*, vol. 8697, no. February 2017, p. 869710, 2012, doi: 10.1117/12.2010259.
- [66] U. Pranav Nayak, M. A. Guitar, and F. Mücklich, “Evaluation of etching process parameter optimization in the objective specific microstructural characterization

- of as-cast and heat treated HCCI alloy,” *Prakt. Metallogr. Metallogr.*, vol. 57, no. 10, pp. 688–713, 2020, doi: 10.3139/147.110682.
- [67] M. A. Guitar, A. Scheid, D. Britz, F. Mücklich, M. A. Guitar, and A. Scheid, “Evaluation of the Etching Process for Analysis of Secondary Carbides in HCCI by Optical and Confocal Laser Microscopy” 2020, [Online]. Available: www.hanser-elibrary.com
- [68] J. Schindelin *et al.*, “Fiji: An open-source platform for biological-image analysis,” *Nat. Methods*, vol. 9, no. 7, pp. 676–682, 2012, doi: 10.1038/nmeth.2019.
- [69] Yuxiong Mao, “Nearest Neighbor Distances Calculation with ImageJ,” <https://icme.hpc.msstate.edu>, 2016. https://icme.hpc.msstate.edu/mediawiki/index.php/Nearest_Neighbor_Distances_Calculation_with_ImageJ.html (accessed Jun. 13, 2022).
- [70] A. A. CASTRILLÓN and M. R. M. TORRES, “Ensayos de dureza,” *Ensayos de dureza*, 2020. <https://www.struers.com/es-ES/Knowledge/Hardness-testing/Vickers>
- [71] J. J. Penagos, J. I. Pereira, P. C. Machado, E. Albertin, and A. Sinatora, “Synergetic effect of niobium and molybdenum on abrasion resistance of high chromium cast irons,” *Wear*, vol. 376–377, pp. 983–992, 2017, doi: 10.1016/j.wear.2017.01.103.
- [72] E. Rabinowicz, L. A. Dunn, and P. G. Russell, “A study of abrasive wear under three-body conditions,” *Wear*, vol. 4, no. 5, pp. 345–355, 1961, doi: 10.1016/0043-1648(61)90002-3.
- [73] T. Sun, R. bo Song, X. Wang, P. Deng, and C. jing Wu, “Abrasive wear behavior and mechanism of high chromium cast iron,” *J. Iron Steel Res. Int.*, vol. 22, no. 1, pp. 84–90, 2015, doi: 10.1016/S1006-706X(15)60014-0.
- [74] F. Maratray, “Choice of appropriate compositions for chromium-molybdenum white irons,” *AFS Trans*, vol. 79, pp. 121-124., 1971.
- [75] D. A. Porter and K. E. Easterling, *Phase Transformations in Metals and Alloys*, vol. 3, no. April. Boston, MA: Springer US, 1992. doi: 10.1007/978-1-4899-3051-4.
- [76] H. Gasan and F. Erturk, “Effects of a destabilization heat treatment on the microstructure and abrasive wear behavior of high-chromium white cast iron investigated using different characterization techniques,” *Metall. Mater. Trans. A*

- Phys. Metall. Mater. Sci.*, vol. 44, no. 11, pp. 4993–5005, 2013, doi: 10.1007/s11661-013-1851-3.
- [77] M. A. Guitar, A. Scheid, S. Suárez, D. Britz, M. D. Guigou, and F. Mücklich, “Secondary carbides in high chromium cast irons: An alternative approach to their morphological and spatial distribution characterization,” *Mater. Charact.*, vol. 144, pp. 621–630, 2018, doi: 10.1016/j.matchar.2018.08.020.
- [78] P. J. Blau, “Interpretations of the friction and wear break-in behavior of metals in sliding contact,” *Wear*, vol. 71, no. 1, pp. 29–43, 1981, doi: 10.1016/0043-1648(81)90137-X.
- [79] P. L. Hurricks, “Some metallurgical factors controlling the adhesive and abrasive wear resistance of steels. A review,” *Wear*, vol. 26, no. 3, pp. 285–304, 1973, doi: 10.1016/0043-1648(73)90184-1.
- [80] A. Demir, N. Altinkok, F. Findik, and I. Ozsert, “The wear behaviour of dual ceramic particles (Al₂O₃/SiC) reinforced aluminium matrix composites,” *Key Eng. Mater.*, vol. 264–268, no. II, pp. 1079–1082, 2004, doi: 10.4028/www.scientific.net/KEM.264-268.1079.

APPENDIX

LIST OF FIGURES

Fig. 1. Diagram of a crystalline and an amorphous structure [1].	3
Fig. 2. The 14 Bravais' networks [1].	4
Fig. 3. Types of dislocations: wedge, helical and mixed dislocations, respectively [5].	5
Fig. 4. Exemplification of a linear dislocation sliding system [8].	6
Fig. 5. Metastable phase-diagram of the iron-carbon system at a lower carbon concentration [10].	9
Fig. 6. a) 3D SEM image of Primary austenite dendrites during solidification of a high-Cr iron before the eutectic reaction takes place [15], and b) Optical microscopy image of the as-cast condition of 16 wt.% Cr HCCI [16].	10
Fig. 7. 2D view of the Iron rich corner of metastable C-Cr-Fe liquidus surface: rectangular box indicates the compositional range of hypoeutectic white cast iron alloys commonly used. Image-based on [14], [19].	11
Fig. 8. Iron-rich corner of the Fe-Cr-C metastable liquidus diagram, for 15 wt.% Cr and 3wt.% C HCCI [14].	13
Fig. 9. SEM (BSE) images for As-cast 16wt.% Cr HCCI at different magnifications from left to right x500, x2000, and x6500, respectively. Image-based on [16].	13
Fig. 10. Austenite and martensite unit cells showing carbon atom position [23], [24].	14
Fig. 11. Representation of a cube of High chromium White cast iron with M_7C_3 carbides [14].	15
Fig. 12. Schematic isothermal transformation diagrams for HCCI: (a) undestabilized austenite, (b) austenite destabilized by precipitation of secondary carbides [20].	19
Fig. 13. Destabilization process at 980 C for different times (0, 30 and 90 min) calculated using MatCalc and the corresponding SC type and fraction. Thermal cycle for the destabilization process (on top) and the SC type and fraction during HT as a function of time (low) [38].	22

Fig. 14. Schematic representation of the elements of tribo-system [40].	24
Fig. 15. Schematic description of the four main wear mechanisms [40].	24
Fig. 16. Two and three-body modes of abrasive wear [43].	25
Fig. 17. Ball-on-plate tribological test [44].	25
Fig. 18. Scheme of a SEM (extracted from NanoScience Instruments, 2016) [59].	30
Fig. 19. Schematic drawing of a scanning electron beam incident on a solid sample, showing some of the signals generated that can be used to help characterize the microstructure [61].	31
Fig. 20. Helios™ G4 PFIB CXe DualBeam™ SEM.	32
Fig. 21. FEI Helios NanoLab™ 600 DualBeam™ FE-SEM.	32
Fig. 22. Representative SEM micrograph of a heat-treated sample chemically etched with Murakami's reagent; (b) represents a 100% overlay of the corresponding micrograph in the back-scattered mode [62].	33
Fig. 23. Scan of a structure with a confocal laser scanning microscope. (Extracted from Leica Microsystems web, year 2008) [63].	34
Fig. 24. LEXT OLS 4100 Olympus CLSM.	35
Fig. 25. Rectangular sample before being mounted.	36
Fig. 26. SPECTROMAXx arc spark optical emission spectroscopy [55].	36
Fig. 27. Furnace used for realizing the Heat Treatments.	37
Fig. 28. Schematic of the performed heat treatment.	38
Fig. 29. Mecapress I metallographic mounting machine.	39
Fig. 30. Struers TegraPol-21 grinder/polisher.	39
Fig. 31. Piece of 16%HCCI after HT after mounting.	40
Fig. 32. Cupboard used for etching the samples.	41
Fig. 33. SEM vCD image of 900°C sample before (a) and after (b) the segmentation using the Trainable WEKA segmentation method.	42
Fig. 34. Struers Dura Scan 50 microhardness tester [70].	43

Fig. 35. Spirale 3 - Excal 2211-HA Environmental chamber and Microtribometer used, respectively	45
Fig. 36. Representative SEM micrographs of As Cast sample, after Vilella's etching for 15 seconds. (a)Shows the eutectic carbides between the austenite dendrites. (b)The different phases, austenite (γ), martensite (α'), pearlite (P), and eutectic carbides (M_7C_3) are indicated in the image (b). The pearlite phase can be observed in the inset in (b). The various phases are marked for reference.....	47
Fig. 37. Optical microscopy images showing: (a) the as-cast condition; (b) the 800°C condition; (c) the 900°C condition; and (d) the 980°C condition. The samples were etched with Vilella's reagent for matrix/carbide contrast. The phases are accordingly colour and arrow labelled for reference.	49
Fig. 38. SEM (BSE) images for all the samples at different magnifications from left to right x 500, x 2000, and x 3500, respectively. (a) As cast, (b) 800 °C, (c) 900 °C Q, and (d) 980 °C. The phases are accordingly colour and arrow labelled for reference.	50
Fig. 39. SEM images showing the morphology of the secondary carbide particles in 800,900 and 980°C respectively.....	51
Fig. 40. SEM BSE mode images after etching with Modified Murakami (a) 800 °C, (b) 900 °C Q, and (c) 980 °C.	52
Fig. 41. Particle size distribution for 800, 900, and 980°C, respectively.	53
Fig. 42. Lognormal curves of the particle size distribution.....	53
Fig. 43. SC particle size cumulative distribution curve.....	54
Fig. 44. distribution-rug plot plotted on a log-log scale, which is indicative of a histogram with zero-width bins and used to visualise the distribution of the data.	54
Fig. 45. Secondary Carbide volume fraction.	56
Fig. 46. Nearest Neighbor Distance distribution for the samples 800, 900, and 980°C.	56
Fig. 47. Lognormal distribution of the Nearest Neighbor Distance for the samples 800, 900, and 980°C.	57
Fig. 48. SC particle nnd cumulative distribution curve.....	58

- Fig. 49. Optical micrograph of the microhardness indentations on the 980°C sample.
..... 59
- Fig. 50. Optical micrograph of microhardness indentations: a) As Cast; b) 800°C; c) 900°C; and d) 980°C. The phases are accordingly colour and arrow labelled for reference.
..... 60
- Fig. 51. Microhardness measurements for four microstructural states: as cast, 800, 900, and 980°C, respectively. The standard deviation of the measures is also plotted..... 61
- Fig. 52. CLSM micrographs of the wear tracks at (a) 800°C, (b) 900°C, and (c) 980°C with a 50% overlap of the height profile. The CLSM micrograph on the left, in blue tones, is based on height, and the one on the right, in grey tones, on intensity. The height range (only applicable to the height profile) and sliding direction (SD) are also mentioned.... 62
- Fig. 53. Wear tracks profile comparison between As Cast, 800, 900, and 980°C..... 63
- Fig. 54. Width vs. depth of wear tracks for each condition..... 63
- Fig. 55. Wear rate comparison on the studied samples. 65
- Fig. 56. Evolution of COF for the different samples..... 66
- Fig. 57. a) SEM micrograph of the wear track for the 800°C sample in BSE mode, with the red rectangle representing the micro-cutting phenomenon. In eutectic carbides, the phenomenon of micro shearing or fracture is observed (b)..... 68
- Fig. 58. (a) SEM micrograph of the wear track for the 800°C sample in BSE mode, with the red rectangle representing the micro-cutting phenomenon. In this case, the ejection of one or a fraction of a eutectic carbide particle is observed (b). In addition, the micro-sanding phenomenon of adhesive wear can be seen in (c)..... 69
- Fig. 59. (a) SEM micrograph in BSE mode of the wear track for the 800°C sample showing the austenitic matrix (γ), eutectic carbides (M_7C_3), and the contrast between deformed and undeformed austenite. (b) Displays a zoomed-in view of the boxed area, indicating the generated directions and slip sets. 70
- Fig. 60. a) SEM micrograph of the wear track on the 800°C sample, where it can be seen within the yellow ellipse, the stop of the slip lines when reaching the secondary carbide zone. (b) Enlarged image of the squared area. 70

Fig. 61. (a) SE SEM micrograph with a 50% overlay of the EDS oxygen concentration map on the wear track. While the EDS concentration maps for iron, carbon, and are depicted in (b), (c), and (d), respectively. 71

Fig. 62. SEM (BSE) micrograph of the wear track on the 900°C sample. Wear particles can be seen next to the wear track (orange rectangle). Micro cuts and micro-cracks can also be seen inside the track, near the EC, as shown in the image (b). 72

Fig. 63. SEM micrograph of the wear track on the 900°C sample, revealing wear particles (orange rectangle) and micro-cracking (red rectangle). Micro-cuts and micro-cracks can also be seen in the interior of the printtrack, close to the EC, as shown in the image (b), as well as signs of adhesion in the image (c). 73

Fig. 64. (a) SEM (SE) micrograph with a 50% overlay of the EDS oxygen concentration map on the wear track. Figure (b) depicts a SE-mode SEM micrograph of the magnified region, while figures (c), (d), and (e) depict EDS concentration maps for oxygen, chromium, and iron, respectively. 74

Fig. 65.(a) SEM EBS micrograph of the wear track on the 980°C sample, with wear particles visible at the track's edges. The fractured and ejected carbides, as well as the cracks generated, are visible (b). 75

Fig. 66. (a) SEM micrograph of the wear track on the 980°C sample, with wear particles visible at the track's edges. The fractured and ejected carbides, as well as the cracks generated, are visible in (b). 76

Fig. 67. (a) SE SEM micrograph with a 50% overlay of the EDS oxygen concentration map on the wear track. (b) SE mode micrograph with 100 percent overlay of Fe (brown) and Cr (red) EDS concentration maps (red). (c) SE mode micrograph with 100 percent overlay of Fe (brown), Cr (red), and O EDS concentration maps (green). 76

LIST OF TABLES

Table 1. Slip planes and slip directions for FCC, BCC, and HCC crystallographic structures [9].....	7
Table 2. Grinding/Polishing parameters.....	38
Table 3. Description of the two etchants employed on the polished samples and their corresponding parameters, depending on the final objective.....	40
Table 4. . Tribological testing parameters.....	44
Table 5. Bulk chemical composition (in wt. %) of the samples was measured by optical emission spectroscopy.....	46
Table 6. SC mean size.....	54
Table 7. Probability of founding a particle with an area more than $0.05 \mu\text{m}^2$	55
Table 8. nnd mean size.....	57
Table 10. Depth and Width reduction percentages concerning the As Cast condition.....	62